SYNTHESIS, CHARACTERIZATION AND STRUCTURE CONTROL OF ORDERED MESOPOROUS SILICA NANOPARTICLES

A Dissertation

Presented to the Faculty of the Graduate School

of Cornell University

In Partial Fulfillment of the Requirements for the Degree of

Doctor of Philosophy

by

Teeraporn Suteewong

January 2011

SYNTHESIS, CHARACTERIZATION AND STRUCTURE CONTROL OF ORDERED MESOPOROUS SILICA NANOPARTICLES

Teeraporn Suteewong, Ph. D.

Cornell University, 2011

Ordered mesoporous silica materials are characterized by uniform and tunable pore size, high surface area and large pore volume. In particular, nano-sized ordered mesoporous silica particles have drawn interest from several fields, including bio-related areas, because silica is benign, possesses chemical stability and can be integrated with other materials. Structural aspects, such as pore connectivity, geometry and pore size are known to govern materials performance. Extensive efforts have been devoted to synthesize mesoporous silica particles with different structures, functionalities and sizes. In contrast, only a small number of studies so far have concentrated on the formation mechanism of these particles. This is hence the focus of the present dissertation.

The first part reports on the synthesis and characterization of ordered mesoporous silica nanoparticles with and without embedded magnetic nanoparticles. The formation mechanism of silica nanocomposites is investigated by capturing particle formation at different time points during the synthesis. A combination of transmission electron microscopy (TEM) and small angle x-ray scattering (SAXS) is used to characterize the structure evolution of resulting materials.

Incorporating organic moieties into the silica matrix provides additional functionalities to ordered mesoporous silica nanoparticles. However, it often leads to disordered pore structure or pore blockage. The second part demonstrates the

preparation of aminated and ordered mesoporous silica nanoparticles using a co-condensation method. Increasing the amount of aminosilane in the synthesis feed causes a structural transition of organically modified particles from hexagonal to cubic. Pore size of ordered mesoporous silica and aminated ordered mesoporous silica nanoparticles can be tailored by the addition of a swelling agent during the synthesis. The structural transformation from hexagonal to cubic is also observed in the latter case, albeit at different amino silane concentrations.

The final part reports on the internalization of nanoparticles into cells. Fluorescent aminated mesoporous silica nanoparticles are first prepared and then coated with poly(ethylene glycol) to improve particle stability and lower protein adsorption. Dye-labeled aminated mesoporous silica nanoparticles are spontaneously internalized by cells.

BIOGRAPHICAL SKETCH

Teeraporn Suteewong was born on the 14th of May in Bangkok, but grew up in Suphanburi. She is the youngest child among 3 daughters, which explains why she was given her nickname, Aey, which means the end in this case. It is often used as the last word in old Thai poems or songs. Her oldest sister's nickname is the first word in the poem. She obtained her kindergarten through high school education in Suphanburi. Her favorite subjects were drawing and science and she found the similarity between these two fields. Once the day came when she had to make a decision between being an architect or a chemist, she chose to study chemistry with the reasoning that she could be a chemist and still design things, but she could not be an architect and do wet labs.

She attended Mahidol University in Bangkok, where she earned a Bachelors and Master degree in Chemistry and Polymer Chemistry, respectively. In her freshman year, she joined the Development and Promotion of Science and Technology Program. With this program, she had the opportunity to pursue research in organic and polymer laboratories every semester with different mentors.

In 2005, while packing her luggage to continue her higher education in Australia, she received a letter from the Department of Materials Science and Engineering at Cornell University accepting her into the Ph.D program. She joined and worked in the group of professor Ulrich Wiesner in 2005 and completed her doctoral degree in January 2011.

To My Parents

ACKNOWLEDGMENTS

Though the following dissertation is my own individual work, I could have never reached heights or explored depths without the help, support, guidance and efforts of a lot of people.

Foremost, I would like to express my sincere gratitude to my advisor, professor Ulrich Wiesner, for his continuous support of my Ph.D study and research, his patience, guidance, motivation and immense knowledge. I have been fortunate to have an advisor who gave me the freedom to explore on my own, and at the same time, to guide me to recovery when my steps were wrong. Professor Wiesner taught me how to question thoughts and express ideas. His infectious enthusiasm and unlimited optimism have been major driving forces through my graduate career at the Cornell University.

I would like to thank my committee, professor Barbara Baird, professor Chekesha Liddell Watson, and professor Lara Estroff, for their encouragement, insightful comments, and questions. I would also like to take this opportunity to thank all my teachers.

I am also indebted to all of the collaborators that I have had the pleasure of working with. I would like to thank Dr. Roy Cohen who spent an enormous amount of time testing my particles. I would also like to acknowledge Dr. Ulrike Werner-Zwanziger and Dr. Josef Zwanziger for the help they have given with the ^{29}Si NMR.

I would like to thank all the staff and facility managers at CCMR and NBTC for their help and suggestions. In particular, I would like to thank John Grazul for his assistance with TEM and his humor. I also deeply appreciate the financial support from the Royal Thai Government Scholarship.

Additionally, I am grateful to the former and current members of the Wiesner group, for their various forms of support during my graduate study. Hooisweng Ow

helped me start as a part of the C dots group and provided continuous support. Andrew Burns and Erik Herz provided advice, humor and entertainment in what could have otherwise been a somewhat stressful laboratory environment. Thanks to Hiroaki Sai who spent a lot of his time running SAXS on my samples, and I would like to give a special thanks to Chris Orilall for helping my car commit suicide. My sincere thank also goes to Dolores Dewbury for her assistance and support.

Throughout the years here I have met friends, which I greatly value their friendship and love. I deeply appreciate their belief in me. You know whom I mean, thank you so much.

I am indebted to my family for their ceaseless encouragement, faith and love, which have helped me stay sane through these difficult years, especially this year. Their support and care helped me overcome setbacks and stay focused on my graduate study in the hardest time of my life. My very special thanks to the one person whom I owe everything I am today, my father. His unwavering faith and confidence in my abilities and in me is what has shaped me to be the person I am today. Thank you for the first scientific book you gave me when I was a kid. Thank you for everything. I love you and wish you were still with me.

TABLE OF CONTENTS

LIST OF FIGURES

LIST OF TABLES

CHAPTER 1

INTRODUCTION

Since the first report on micron-sized mesoporous silica particles with two-dimensional hexagonally ordered pore arrays in 1997,[1] intense efforts have been devoted to develop ordered mesoporous silica nanoparticles with controlled structures and functionalities. Nano-sized mesoporous silica combines advantages of silica as a matrix and of porous materials. Silica is benign, possesses chemical stability and can be endowed with versatile functionalities. Mesoporous silica exhibits uniform and tunable pore size, high specific surface area and large pore volume, making it suitable for a variety of potential applications in nanobiotechnology and nanomedicine.

Due to aforementioned characteristics, the idea of using mesoporous silica to absorb substances was first introduced in 1999.[2] Shortly afterwards, in 2001, micron-sized mesoporous silica possessing two dimensional, hexagonal pore structure, referred to as MCM41-type, was proposed for the first time and used as drug carrier.[3] Intensive efforts on the development of mesoporous silica-based drug delivery systems have since driven the field forward.[4, 5, 6, 7] Structural aspects, for example pore connectivity, geometry and pore size, have been considered and affect materials performance. From these parameters, particle size has attracted considerable attention for nanomedicinal uses. Research efforts have been devoted to controlling the particle size of ordered mesoporous silica as well as integrating different materials with silica to improve its functionalities.[8] As a result, today mesoporous silica nanoparticles are widely used in bio-related studies, both *in vitro* and *in vivo*, as multifunctional probes, such as drug delivery systems, theranostic systems as well as for bio-imaging.

While a lot of exploratory research has been performed in the past, fewer studies are devoted to the understanding of the formation mechanisms of mesoporous

silica nanoparticles. This has thus been the focus of the present dissertation. First, the synthesis and characterization of ordered mesoporous silica nanoparticles with embedded iron oxide nanoparticles is presented. The formation mechanism of the silica nanocomposites is investigated by capturing particle formation at different time points during the synthesis. The study reveals the structure evolution from disordered to ordered pore arrays occuring at the same time as a re-location process of iron oxide nanoparticles within the silica particles. Analogous to impurities during crystal growth, the iron oxide nanoparticles act as seeds at the early stages and are pushed from the silica particle centers to the edges (crystal grain) at the end of the particle growth.

Surface chemicals, pore geometry as well as pore size influence the properties of mesoporous silica regardless of particle size. Chemical modification of mesoporous silica can be accomplished either by post-synthetic grafting or by co-condensation with organosilanes.[9, 10] The latter provides a uniform distribution of organic moieties, but can affect shape and pore structure of the resulting materials.[9, 10] Using a large amount of organosilane in the synthesis often causes loss of hierarchical pore structure.[11] Incorporating a desired amount of organosilane into mesoporous silica nanoparticles without disrupting the regularity of the pore structure is hence an important goal. Control of surface properties and pore structures of nano-sized mesoporous silica is the focus of the second part of the thesis. To this end, amine-modified ordered mesoporous silica nanoparticles are prepared by means of a co-condensation method. By feeding different amounts of aminosilane in the synthesis, pore architecture transforms from two-dimensionally hexagonal to three-dimensionally cubic symmetries. The formation mechanism of mesoporous silica nanoparticles with cubic symmetry is investigated next. Incorporating a swelling agent in the particle synthesis controls pore size of both, aminated and non-aminated

materials. This approach enlarges pore width of the resulting materials without appreciable loss of order of the pore system. It also decreases overall particle size to values smaller than 100 nm.

Since mesoporous silica nanoparticles have attracted much interest as imaging probes, both *in vitro* and *in vivo*, studies are extended to the synthesis of fluorescent aminated mesoporous silica nanoparticles. To this end fluorescent organic dye molecules can be covalently incorporated into the silica matrix without significantly disrupting pore symmetry. After PEGylating the particle surface to prevent undesirable particle aggregation and interactions with, e.g. proteins, dye-labeled aminated mesoporous silica nanoparticles are spontaneously internalized by cells.

REFERENCES

1. Grun, M.; Lauer, I.; Unger, K. K., *Advanced Materials* **1997,** *9* (3), 254-257.

2. Hata, H.; Saeki, S.; Kimura, T.; Sugahara, Y.; Kuroda, K., *Chemistry of Materials* **1999,** *11* (4), 1110-1119.

3. Vallet-Regi, M.; Ramila, A.; del Real, R. P.; Perez-Pariente, J., *Chemistry of Materials* **2001,** *13* (2), 308-311.

4. Vallet-Regi, M.; Balas, F.; Arcos, D., *Angewandte Chemie, International Edition* **2007,** *46,* 7548-7558.

5. Liong, M.; Lu, J.; Kovochich, M.; Xia, T.; Ruehm, S. G.; Nel, A. E.; Tamanoi, F.; Zink, J. I., *Acs Nano* **2008,** *2* (5), 889-896.

6. Park, K.; Lee, S.; Kang, E.; Kim, K.; Choi, K.; Kwon, I. C., *Advanced Functional Materials* **2009,** *19* (10), 1553-1566.

7. Fan, J.; Yu, C. Z.; Gao, T.; Lei, J.; Tian, B. Z.; Wang, L. M.; Luo, Q.; Tu, B.; Zhou, W. Z.; Zhao, D. Y., *Angewandte Chemie, International Edition* **2003,** *42* (27), 3146-3150.

8. Piao, Y.; Burns, A.; Kim, J.; Wiesner, U.; Hyeon, T., *Advanced Functional Materials* **2008,** *18* (23), 3745-3758.

9. Huh, S.; Wiench, J. W.; Yoo, J. C.; Pruski, M.; Lin, V. S. Y., *Chemistry of Materials* **2003,** *15* (22), 4247-4256.

10. Sadasivan, S.; Khushalani, D.; Mann, S., *Journal of Materials Chemistry* **2003,** *13* (5), 1023-1029.

11. Atluri, R.; Sakamoto, Y.; Garcia-Bennettt, A. E., *Langmuir* **2009,** *25* (5), 3189-3195.

CHAPTER 2

ORDERED MESOPOROUS SILICA NANOPARTICLES WITH AND WITHOUT EMBEDDED IRON OXIDE NANOPARTICLES: STRUCTURE EVOLUTION DURING SYNTHESIS[*]

2.0 Abstract

This work reports on the structural evolution during room temperature synthesis of hexagonally ordered mesoporous silica nanoparticles with and without embedded iron oxide particles. Oleic acid-capped iron oxide nanoparticles are synthesized and transferred to an aqueous phase using the cationic surfactant, hexadecyltrimethylammonium bromide (CTAB). MCM-41 type silica and composite nanoparticles are fabricated *via* sol–gel synthesis. Aliquots are taken from the solution during synthesis to capture the particle formation process. Transmission Electron Microscopy (TEM) and Small Angle X-ray Scattering (SAXS) reveal a transition from a disordered to an ordered structure in both synthesis systems. Along with the evolution of structure, iron oxide nanoparticles acting as seeds at the early stages are relocated from the particle centers to the edges. Nitrogen sorption measurements for iron oxide-embedded mesoporous nanoparticles indicate surface areas as high as for the mesoporous silica nanoparticles without iron oxide.

[*] Originally Published as: Teeraporn Suteewong, Hiroaki Sai, Jinwoo Lee, Michelle Bradbury, Taeghwan Hyeon, Sol M. Gruner and Ulrich Wiesner. *Ordered Mesoporous Silica Nanoparticles with and without Embedded Iron Oxide Nanoparticles: Structure Evolution during Synthesis.* Journal of Materials Chemistry, 2010, **20**, 7807-7814. Reproduced by permission of The Royal Society of Chemistry. http://pubs.rsc.org/en/Content/ArticleLanding/2010/JM/c0jm01002b

2.1 Introduction

Since the pioneering work by Stöber *et al.*, silica nanoparticles have been explored as candidates for a variety of applications including photonics and biomedicine.[1, 2] Nano-sized silica materials provide not only excellent intrinsic properties, such as low toxicity, excellent chemical stability and versatile functionalization chemistry, but also have the capability of being platforms for, or being integrated with, other nanomaterials.[3] The aforementioned characteristics have led to the development of multifunctional nanocomposites, in which properties of individual components are combined to create new features including drug delivery systems and lasing.[4, 5] Silica-based nanomaterials with new functionalities have been continuously developed. One example is one-dimensional hexagonally ordered mesoporous silica, known as MCM-41.[6, 7, 8] This material possesses uniform and tunable pore size, functionalizable surfaces, high specific surface area and large pore volume suitable for a variety of potential applications.[9, 10, 11, 12, 13, 14, 15] By modification of the Stöber method, Grun *et al.* reported the first synthesis of micrometre-size MCM-41-type particles.[16] Since then, nano-sized MCM-41 materials have been explored for biological applications.

Combining mesoporous silica with metals and metal oxides results in hybrid mesoporous silica nanoparticles with combinations of properties. Such hybrids could be used in applications, such as drug delivery, MRI and catalysis.[3, 11, 12, 13, 14, 17, 18, 19, 20, 21, 22] A hexagonal pore arrangement could facilitate the use of these nano-sized materials to the desired purposes. However, generation and preservation of such periodic silica structure during synthesis and processing is always a challenge. There have been many attempts to incorporate inorganic nanoparticles into the siliceous matrix without loss of the ordered structure. Back filtration of metal salt solutions into the pre-formed mesoporous materials and subsequent *in situ* formation of metal

particles have been applied to synthesize metal particle-embedded mesoporous silica composites.[17] Nooney and co-workers successfully grew a mesoporous silica shell onto silica-coated gold nanoparticles.[23, 24] Similarly, tumbler-like ordered mesoporous silica nanoparticles were synthesized at 50 °C in the presence of silica-coated magnetic nanoparticles.[18, 21] Recently, one-pot syntheses of magnetic core-containing silica nanospheres with ordered periodic mesostructure at elevated temperature (80 °C and below 65 °C, respectively) were reported.[14, 25, 26] In order to fabricate such hierarchical hybrid materials with optimal structure control, it is of interest to understand the formation mechanism. Indeed, several formation mechanisms have been proposed based on the structures of the final products.[14, 24, 26] What has been mostly lacking in the literature, however, is a systematic study of the formation mechanism with identification of early, intermediate and final stages of materials structure.

The present work reports on room temperature synthesis of magnetic iron oxide nanoparticle-containing MCM-41-type nanoparticles. The goal is to elucidate the formation mechanism to allow control of the location of the iron oxide nanoparticles within the siliceous particle matrix. To this end, magnetite particles were synthesized using a thermal decomposition method.[27] The resulting oleic acid-capped inorganic nanoparticles were transferred into an aqueous phase using a cationic surfactant, hexadecyltrimethylammonium bromide (CTAB).[12] The sol–gel silica reaction was performed in the presence of the CTAB-stabilized iron oxide nanoparticles. The dilution/neutralization method reported by Mann and coworkers was employed to lower the reaction rates and associated aggregation.[28, 29] Aliquots were taken at different time points for which the reaction was halted by the addition of hydrochloric acid. The structures at different reaction times were studied using Transmission Electron Microscopy (TEM) and Small Angle X-ray Scattering (SAXS)

and compared to results of the synthesis of MCM-41-type nanoparticles without embedded iron oxide nanoparticles. Surface area and pore size were inferred from nitrogen adsorption/desorption measurements.

2.2 Experimental

2.2.1 Chemicals

Hexadecyltrimethylammonium bromide (approx. 99%), ethyl acetate (ACS grade), tetraethyl orthosilicate (TEOS, ≥99%, GC), ammonium hydroxide (29%), acetic acid (glacial), hydrochloric acid (36.5–38%), ethanol (absolute, anhydrous), deionized water (Milli-Q, 18.2 MΩ-cm), chloroform (AR grade), 1-octadecene (AR grade), iron(III) oxide (FeO(OH)) (hydrated, 30–50 mesh), oleic acid (technical grade, 90%) and acetone (AR grade) were used as obtained without further purification.

2.2.2 Synthesis of Magnetic Nanoparticles

Iron oxide nanoparticles (8–9 nm) were synthesized as reported in the literature.[27] FeO(OH) (0.356 g) was mixed with oleic acid (4.52 g) and 1-octadecene (10 mL) in a three-necked round bottom flask. While stirring, nitrogen gas was purged through the mixture for 10 min before heating to 320 °C for 1 h. After cooling to room temperature, the as-made nanoparticles were cleaned by the addition of acetone and separated by centrifugation. After removal of the supernatant, the particles were re-dispersed in hexane and the washing procedure was repeated two more times. The particles were suspended in chloroform for the next step.

2.2.3 Phase Transfer of Magnetic Particles to Aqueous Phase

Magnetic nanoparticles (15 mg in 0.5 mL of chloroform) were added to aqueous CTAB solution (5 mL, 54.8 mM). The mixture was stirred until a

homogeneous microemulsion was formed. The solution was then transferred to a pre-heated oil bath at 70 °C for 10 min to evaporate the chloroform as well as to induce the interaction between the hydrophobic chains of the two surfactants.

2.2.4 Synthesis of Mesoporous Silica Nanoparticles Incorporating Magnetic Nanoparticles

The fabrication of iron oxide–silica nanoparticle composites was modified from Kim *et al.* and Fowler *et al.*[12, 28] As-made CTAB-stabilized magnetic nanoparticles solution (0.5 mL) was diluted in water (10 mL), followed by the addition of ethyl acetate (0.088 mL). NH_4OH (0.27 mL) and TEOS (50 mL) were subsequently added and the solution was stirred for 5 minutes. Then, water (3.69 mL) was added into the reaction, which proceeded for another 10 minutes. Aliquots were taken from the reaction mixture every minute and neutralized by adding 2 M HCl. The resulting material was cleaned by centrifugation using water and ethanol. To remove the surfactant templates, in the last washing, particles were redispersed in an ethanol/acetic acid (glacial) mixture (95/5, v/v) and the mixture was stirred for 30 minutes. Centrifugation in water and ethanol was employed in the cleaning step.

2.2.5 Synthesis of Mesoporous Silica Nanoparticles without Magnetic Nanoparticles

For comparison, mesoporous silica nanoparticles were synthesized in the absence of CTAB-stabilized magnetic nanoparticles. CTAB solution (0.5 mL, 54.8 mM) was added into water (10 mL). The subsequent steps were identical to what has been described in the foregoing synthesis of magnetic nanoparticle-embedded mesoporous silica nanoparticles.

2.2.6 Characterization

Transmission Electron Microscopy (TEM) images were obtained with an FEI Tecnai T12 Spirit microscope operated at an acceleration voltage of 120 kV. Particle size distributions were obtained by averaging over approximately 30 (short aging times) to 100 (longer aging times) particles. The standard deviation is reflected in error bars in Figure 2.5. Small-Angle X-ray Scattering (SAXS) patterns of samples after surfactant template removal in dry and wet forms were obtained on a home-built beamline as previously described,[30] as well as on the G1 beamline in Cornell High Energy Synchrotron Source (CHESS). Nitrogen physisorption isotherms of dried samples were obtained with a Micromeritics ASAP2020 physisorption instrument.

2.3 Results

Integrating inorganic nanoparticles into ordered mesoporous materials without disrupting the ordered structure of the matrix is a challenge. Only a few reports on one-step synthesis processes exist.[14, 23, 24, 25] Silica condensation in the presence of seed particles normally yields a core/shell morphology, *i.e.*, pre-formed particle cores with a secondary material shell. In the case of MCM-41 type mesoporous silica nanoparticles incorporating iron oxide nanoparticles, it is of interest to investigate the evolution of structure at different reaction times. To this end, we synthesized magnetic nanoparticles using thermal decomposition, yielding monodisperse particle sizes around 8–9 nm (Figure 2.1(a)). As-synthesized iron oxide particles were capped with oleic acid making them soluble in an organic solvent. Figure 2.2 shows a schematic representing the transfer of oleic acid-capped iron oxide from chloroform to an aqueous solution of CTAB.[12] Upon heating, the organic solvent evaporated and particles were transferred to an aqueous phase driven by the van der Waals interactions between the hydrophobic chains of adsorbed ligands on the particle

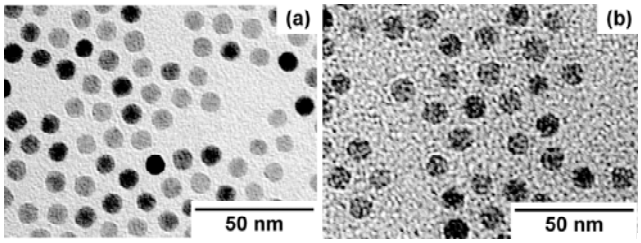

Figure 2.1. TEM of (a) oleic acid-capped iron oxide nanoparticles and (b) CTAB-coated iron oxide nanoparticles.

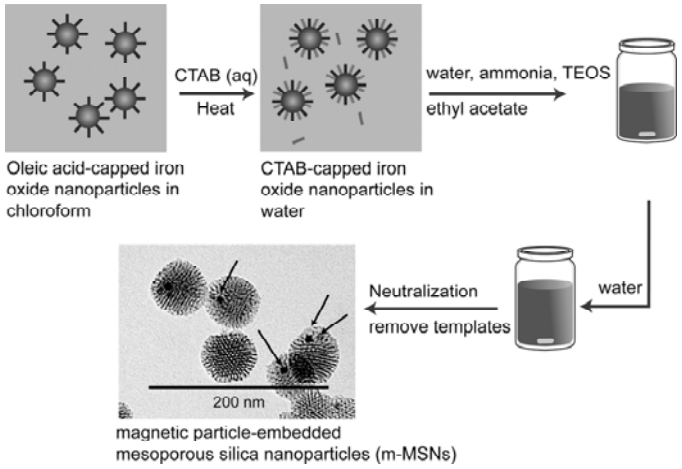

Figure 2.2. Synthesis scheme for magnetic particle-containing mesoporous silica nanoparticles (m-MSNs). Arrows indicate iron oxide nanoparticles incorporated.

surface and of CTAB, leading to the formation of bilayer structures with quaternary ammonium groups pointing outwards.[14] Resulting particles (Figure 2.1(b)) were diluted further before the addition of the silica precursor TEOS. A sol–gel reaction proceeding in the presence of CTAB-modified magnetic nanocrystals, with subsequent removal of the surfactant templates yielded highly ordered mesoporous silica nanoparticles with magnetic particles embedded in the matrix, referred to as m-MSNs. The size of the m-MSNs in Figure 2.2 is 62 ± 10 nm and the iron oxide in the electron micrographs appears to be predominately near the outer particle surface rather than in the particle center. To the best of our knowledge, this is the first report on room temperature and short time scale (15 minutes) synthesis of magnetic nanoparticles embedded in highly ordered mesoporous silica nanoparticles.

In the present study, after adding TEOS, the mixture was stirred for 5 minutes (mixing time). Then, additional water was added into the system and the reaction proceeded for another 10 minutes (aging time). During aging, aliquots were taken every minute and neutralized to halt the ongoing chemical processes. The addition of water after the first 5 minutes causes a decrease in the pH of the system, which results in slowing of silica hydrolysis but accelerates the silica condensation.[28, 29] Templates were subsequently removed using acid extraction (see Experimental) and air dried. TEM images of m-MSNs at different aging times are shown in Figure 2.3. An interesting structural evolution from disordered to ordered silica as a function of the aging time from 1 to 10 min is observed in these images including a change in location of the iron oxide particles from the center to the outer edge of the siliceous matrix. At the early aging stage (1–2 minutes), a core/shell type morphology with iron oxide cores and porous silica shells is found (Figure 2.3(a) and (b)), similar to what has been previously reported.[14] TEM images suggest that the iron oxide nanoparticles are all distributed within a disordered silica shell. The particles are about 42 ± 5 nm in size.

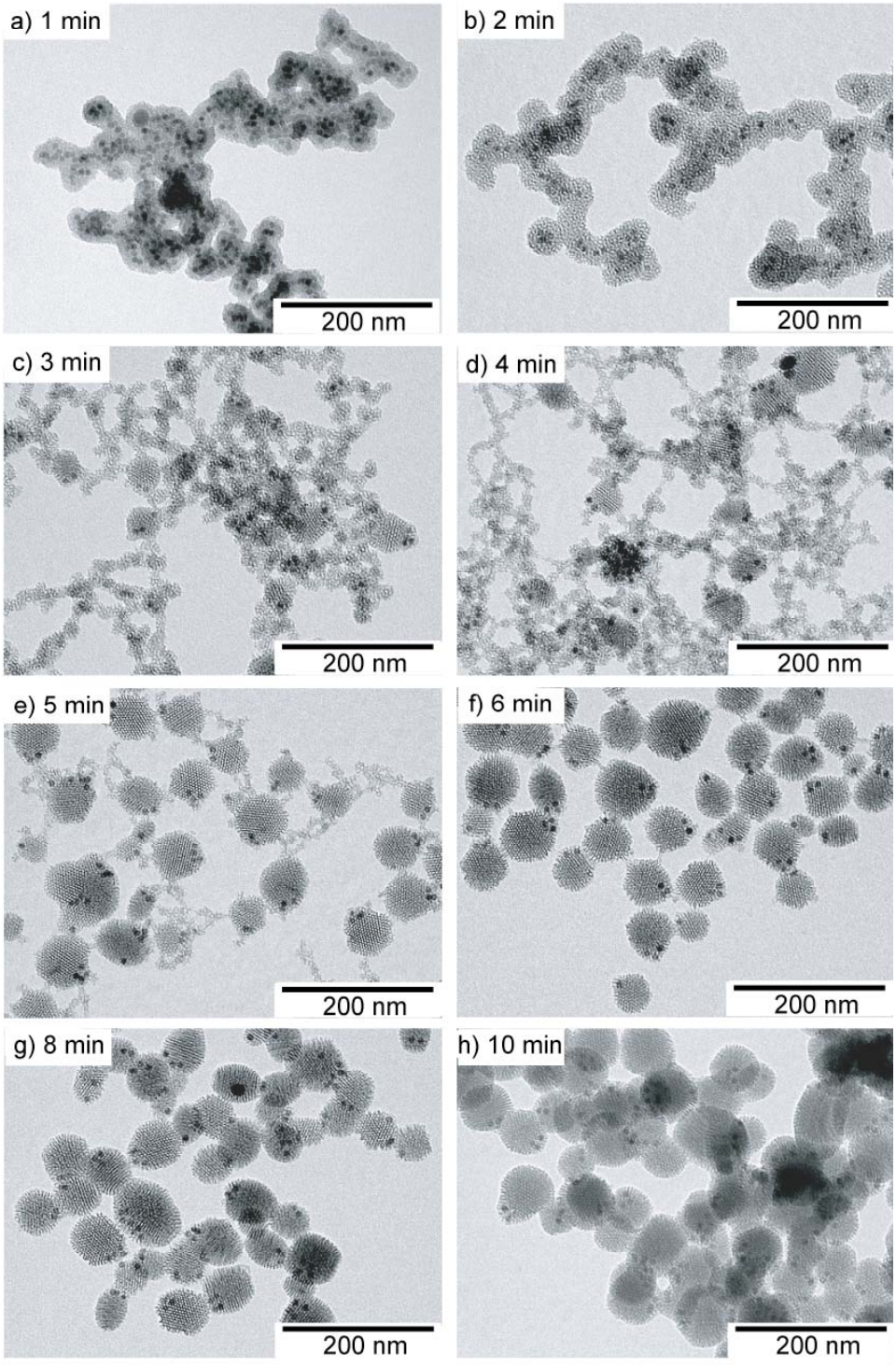

Figure 2.3. TEM of m-MSNs captured at different aging times from 1 to 10 minutes (a-h).

At aging time 3 minutes (Figure 2.3(c)), the inorganic particles are no longer located in the middle of the silica matrix, but are relocating to the edges. The structure of the silica matrix itself is also changing, *i.e.*, order is developing and, besides the primary particles, small secondary clusters of porous silica are forming. These clusters decrease in number when the reaction time increases (Figure 2.3(d) and (e)) and disappear after about 6 minutes of aging time (Figure 2.3(f)). Beyond 6 minutes, the morphology of the nanoparticle composites does not change significantly. After that time, highly ordered MCM-41-type nanoparticles containing iron oxide particles at their edges are obtained that are about 63 ± 9nm in size.

As a control, mesoporous silica particles without magnetic particle seeds (referred to as b-MSNs) were synthesized according to the protocol described in the Experimental section. TEM images of b-MSNs at different aging times are shown in Figure 2.4. Overall the structural evolution is similar to that in Figure 2.3, albeit exhibiting different particle sizes and kinetics. An accelerated disorder-to-order transition is observed, relative to the m-MSNs case. At an aging time of 1 minute, agglomerates of porous silica particles are seen. Although difficult to precisely determine, the size of the primary particles is of order 100 nm, *i.e.*, significantly larger than the primary particles obtained in the presence of iron oxide. The development of order starts at 2 minutes and can be clearly discerned at an aging time of 3 minutes (Figure 2.4(c)). At the 2 minute time point, secondary and loosely packed porous silica particles, roughly 20 nm in diameter, appear in TEM (Figure 2.4(b)). They disappear over the next 2 minutes and are absent in the image representing the time point of 5 minutes (Figure 2.4(e)). Particle size as well as structural order increases with increasing aging time. No significant changes are seen beyond about 5 minutes. The size of the final particles in Figure 2.4 is 117 ± 23 nm, *i.e.*, significantly larger than that of the iron oxide containing particles in Figure 2.3.

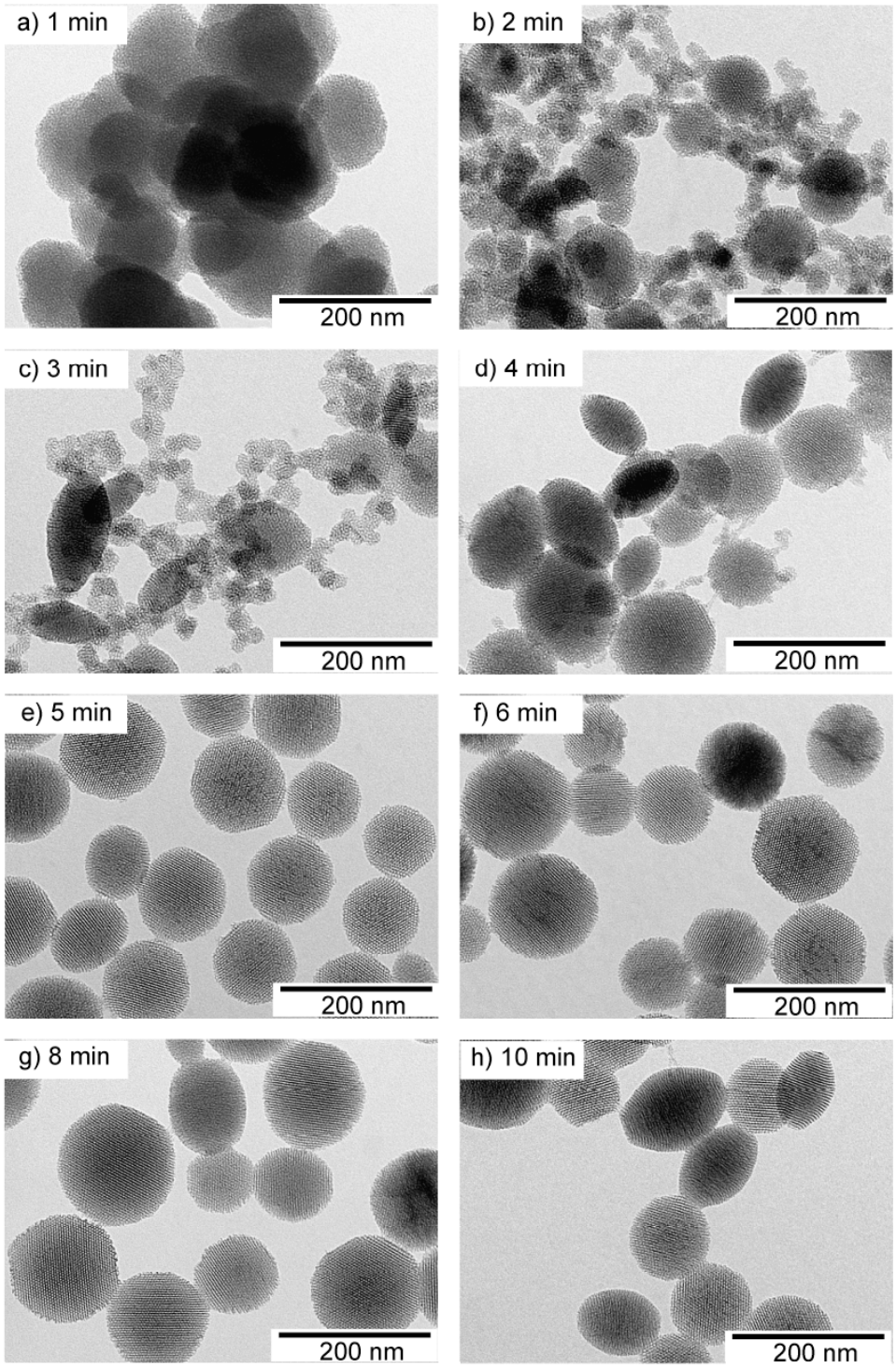

Figure 2.4. TEM of b-MSNs captured at different aging times from 1 to 10 minutes (a-h).

Particle size and size distributions of m-MSNs and b-MSNs at different aging times measured from TEM images are shown in Figure 2.5. Data at an aging time of 1 minute are excluded due to the aggregation of particles, making analysis difficult. Particle size increases in both cases with increasing aging time for about the first 7 minutes, with no significant changes after that. From this plot, it is evident (i) that particles with iron oxide seeds are smaller at any stage as compared to the control particles without iron oxide, (ii) that particle growth is accelerated for b-MSNs relative to m-MSNs, and (iii) that particle size distributions are larger in the case of b-MSNs throughout the formation process as obtained from analysis of TEM images.

In order to better characterize the structural order inside the particles, Small-Angle X-ray Scattering (SAXS) was used. Radially integrated scattering intensity profiles of particles in native solution (no treatment performed after neutralization), cleaned as-made particles in ethanol (before removing CTAB) and CTAB-removed particles in ethanol are shown in Figure 2.6(a). They were investigated in order to exclude significant structural transitions upon different processing steps. All solution patterns were taken at an aging time of 10 minutes. According to the SAXS patterns shown in Figure 2.6(a), there is no structural transition upon template removal. Compared to solution samples, however, SAXS reflections of dried samples taken at 10 minute aging times slightly shift to higher q values. For example, the first order peak shifts from 1.66 nm^{-1} in wet samples to 1.76 nm^{-1} in dried samples, where q denotes the scattering vector and is defined as $q = (4\pi \sin\theta)/\lambda$ with a scattering angle 2θ and the X-ray wavelength $\lambda = 1.54$ Å. This shift likely results from a contraction induced by further silica condensation upon drying. While scattering intensities from the suspensions are smaller than those from dried samples aside from peak shift, significant structural transitions were not observed upon drying. We therefore subsequently consider and discuss results only on the dried samples.

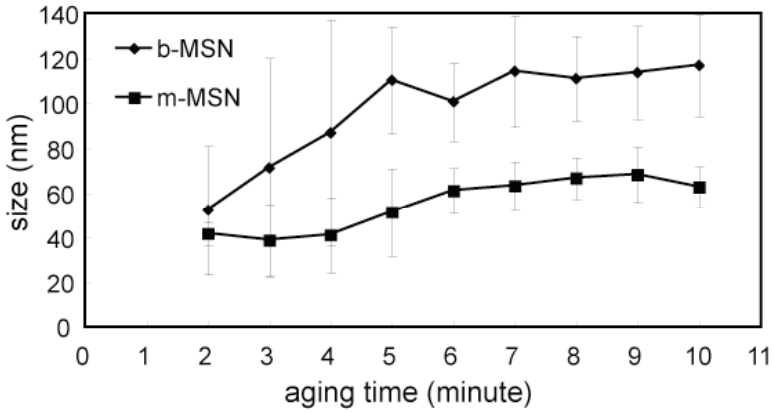

Figure 2.5. Particle sizes and size distributions of m-MSNs and b-MSNs at different aging times as obtained from TEM data analysis.

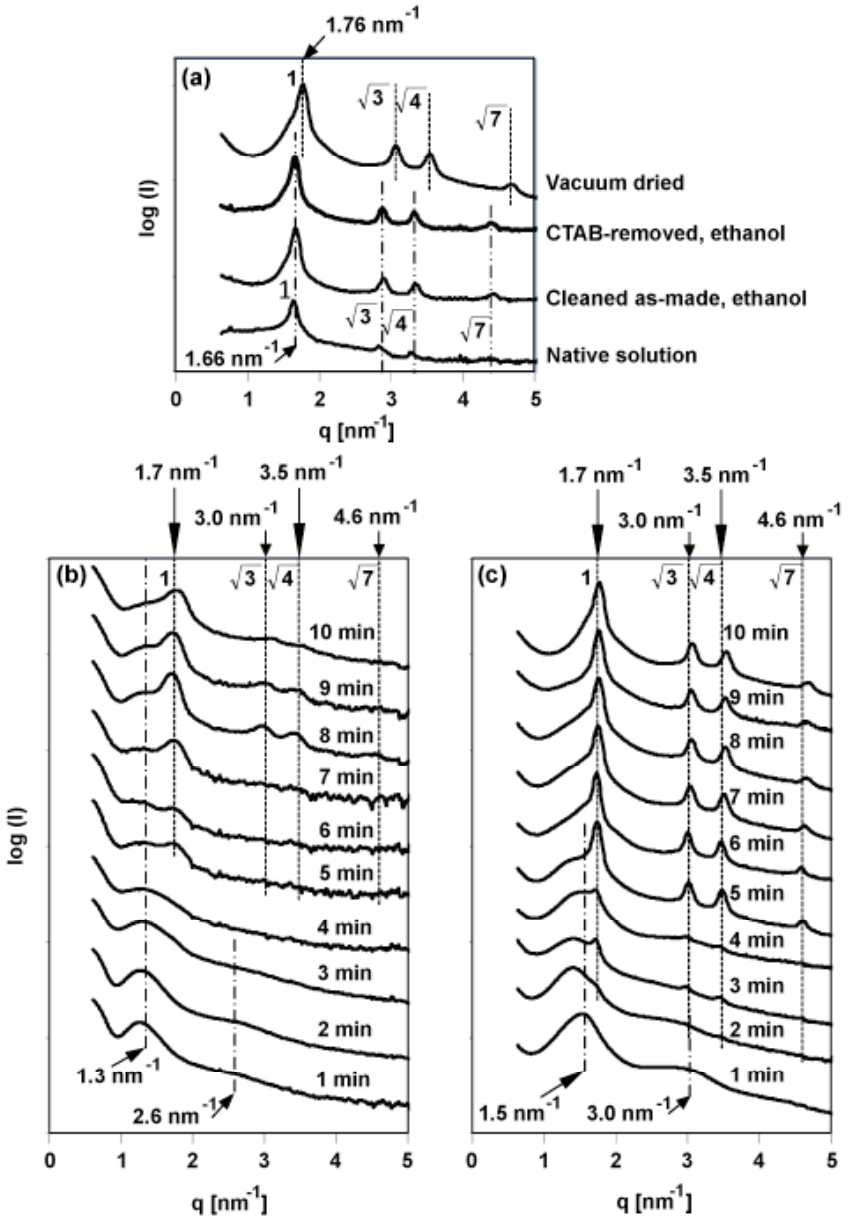

Figure 2.6. SAXS patterns of (a) b-MSN samples in vacuum dried form and suspensions (aqueous native solution, cleaned particles in ethanol before and after removal of CTAB) at an aging time of 10 minutes and SAXS patterns of dry CTAB-removed samples of (b) m-MSNs and (c) b-MSNs at different aging times from 1 to 10 minutes.

The structural evolution of nanoscale order during the particle formation in the 10 minute timeframe is studied for both m-MSN and b-MSN samples. A set of peaks at q = 1.7, 3.0, 3.5 and 4.6 nm^{-1} is observed. These reflections are consistent with the (10), (11), (20) and (21) peaks of a hexagonally packed cylindrical structure with an inter-channel distance of 4.2 nm. A broader set of peaks that initially appears at q = 1.5 and 3.0 nm^{-1} for b-MSNs and at q = 1.3 and 2.6 nm^{-1} for m-MSNs diminishes as the hexagonal peaks grow stronger. Both materials develop a more defined pattern characteristic of MCM-41 as time progresses. In the case of m-MSNs, a peak at q =1.3 nm^{-1} and a broad hump at 2.6 nm^{-1} can be observed from 1 to 4 minutes of aging time. At the 3 and 4 minute time points, the peak at lower q broadens toward higher q values. After that, starting from an aging time of 5 minutes, a more pronounced peak evolves at 1.7 nm^{-1}. As time progresses, additional peaks at q = 3 and 3.5 nm^{-1} are appearing, while after about 8 minutes of aging time, no significant further changes are observed. Similar trends are found in the kinetics study of b-MSN samples. However, a clear onset of hexagonal order is already observed at about 2 minute aging time, *i.e.*, significantly earlier than for m-MSNs. The biggest structural changes here occur between about 2 and 5 minutes, whereas after about 6 minutes, there are no significant further changes in the SAXS patterns of b-MSNs.

The N_2 sorption isotherms of MSNs with and without magnetic particles are shown in Figure 2.7. Both data sets exhibit type IV isotherms, without hysteresis loops, meaning that all pores are accessible. The pore size of m-MSNs as derived from the Barrett– Joyner–Halenda (BJH) analysis is almost unchanged over that of b-MSNs: 2.74 and 2.70 nm for m-MSNs and b-MSNs, respectively.[31, 32] The presence of magnetic particles incorporated into the siliceous matrix slightly affected the Brunner–Emmett–Teller (BET) specific surface area of MSNs, however, which was 893 $m^2 g^{-1}$ for m-MSNs and 1240 $m^2 g^{-1}$ for b-MSNs.

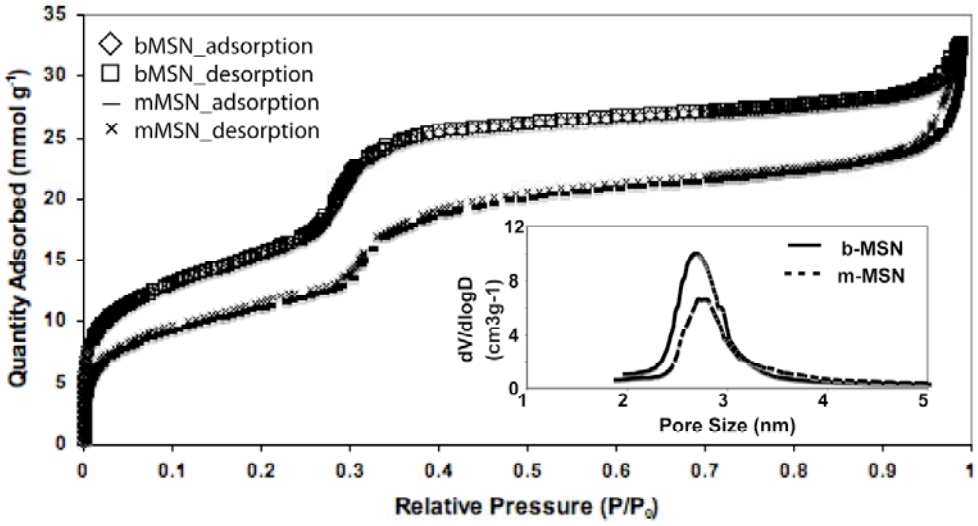

Figure 2.7. N_2 sorption isotherms of b-MSNs and m-MSNs after 10 minutes of aging time. Inset: pore size distributions as obtained from adsorption measurements (*V* = pore volume and *D* = pore size).

2.4 Discussion

In the past, multiple studies reported on the formation mechanisms of MCM-41 type materials, especially in the bulk.[8, 33, 34, 35] No single mechanism has been fully agreed to, however,[9] because the synthesis conditions typically change from one study to another, including temperature, catalyst, reaction time, solvent, pH, type of silica source and concentration of reactants. Based on this body of work, the synthesis and applications of ordered MSNs embedded iron oxide nanoparticles have been described. Less time has been devoted to elucidating their formation mechanisms. To this end, herein, the formation of ordered MSNs containing magnetic nanoparticles is elucidated based on TEM and SAXS measurements of particles and controls at different time points. The syntheses of inorganic nanoparticle-containing MSNs with and without ordered structure have been reported.[12, 14, 21, 24, 25, 26, 36]

Less attention has been paid to the correlation between the location of the magnetic particles and the structure evolution of the mesoporous matrix. Nooney *et al.* reported the synthesis of mesoporous silica/gold composite particles by growing a mesoporous silica layer on pre-existing nuclei, *i.e.*, silica-coated gold nanoparticles.[24] Both disordered and ordered mesoporous silica/ gold particles were found depending on the given synthesis conditions: if water was the only solvent, hexagonally-shaped ordered porous silica composites were observed, in which the gold seeds were located close to the particle edges. Under such conditions, elongated CTAB micelle–silica aggregates are formed preferring a directional aggregation to form an ordered structure on the existing silica-coated gold nanoparticles. If alcohol was used as co-solvent, however, micelles had smaller aspect ratios and their packing was disturbed yielding a disordered porous silica shell around center-located gold seeds. Zhang and co-workers reported on the fabrication of magnetic core/ ordered mesoporous silica shell nanospheres.[14] Stearic acid-capped magnetic particles were transferred to aqueous

phase using different alkyltrimethylammonium bromide surfactant chain lengths (C14–C18), prior to the synthesis of porous silica shells at 80 °C for 2 h. TEM images showed that iron oxide nanocrystals were well distributed in the center of the particles. Cationic surfactant-modified iron oxide particles acted as seeds for the packing and self-assembly of silica–surfactant complexes.

What both cases have in common is the incorporation of inorganic particles into the structurally ordered matrix. However, different inorganic particle locations and silica particle shapes were observed. The deduction of the particle formation mechanism based on the shape and morphology of the final materials is difficult, however. What happens during particle growth of such composites may help elucidate key steps in the formation processes leading to better control. To this end, here, we presented a kinetics study of the formation of magnetic nanoparticle-containing MCM-41 silica nanoparticles by tracking the reaction at different time points.

For simplicity, the key observations are divided into two periods: *i.e.*, the early stage (before an ordered structure is developed) and the ordering/restructuring stage, where the evolution of hexagonally arrayed cylinders is observed. During the early stage, comparing particle sizes and size distributions from TEM data analysis shown in Figure 2.5, initial particle sizes (aging time = 2 minutes) are significantly smaller when iron oxide seeds are present, *i.e.*, about 42 ± 5 nm for m-MSNs and about 52 ± 29 nm for b-MSNs. The size distribution is also smaller when magnetic particles are present. The location of magnetic particles initially (1–2 minutes of aging time) is in the center of the silica nanoparticles, see Figure 2.3(a) and (b)). These observations suggest that the magnetic nanoparticles may act as seeds for the growth of more homogeneously sized mesoporous silica particles. This is corroborated by additional experiments (data not shown) in which we decreased the amount of seed particles resulting in larger m-MSN size. During the second stage, *i.e.*, during the development

of hexagonal structure (Figure 2.3(c)–(h)), the disorder-to-order transition of the silica matrix is retarded by the presence of magnetic nanoparticles. Upon silica ordering, the magnetic nanoparticles are relocated to the boundaries of the ordered domains, a process that is typical for crystallization in the presence of impurities.[37] These results imply that magnetic nanoparticles act as impurities, which delay the crystallization process and end up at the grain boundaries. The other noticeable feature in Figure 2.3(c)–(f) is the existence of small secondary porous silica particles formed during the ordering stage. We suggest that this secondary nucleation and growth burst are associated with the second addition of water. While the primary particles grow, the secondary particles decrease in number and disappear, suggesting Ostwald ripening.

Figure 2.8 is an illustration of the observed formation mechanism of m-MSNs. This cartoon is divided into 3 parts: Part I shows the stepwise addition of all synthesis components, the middle part describes the mixing step taking place for 5 minutes after the addition of TEOS, and the last part describes the aging step, for which the kinetics study was conducted. The addition of TEOS initiates Part II. Phase separation of small TEOS droplets occurs from the aqueous phase due to its immiscibility with water. This phenomenon suggests that dissolution time is the rate limiting step.[24] TEOS molecules are hydrolyzed at the TEOS/water droplet interface generating ethanol as a by-product. This gradually changes the polarity of the system increasing the solubility of TEOS. Condensation between hydrolyzed TEOS molecules happens along with the electrostatic interaction with surfactant-stabilized inorganic particles, free surfactant molecules and surfactant micelles leading to the formation of magnetic core/porous silica shell particles as observed in Figure 2.3(a) and (b).[14] This process is seeded by the small magnetic nanoparticles. Seeding leads to smaller overall particle size and smaller particle size distributions as compared to the unseeded process. Water added at the end of the mixing step induces a sudden change in TEOS solubility and initiates

Part III. This causes a secondary nucleation burst, yielding the formation of small secondary silica nanoparticles. These later-formed nanoparticles are consumed by the growing primary nanocomposites in an Oswald ripening-type process.

Lowering the solution pH is expected to be an important factor in restructuring silica into highly hexagonally ordered structures.[10] Two parameters affecting pH in this study are ethyl acetate and water added after the mixing step. Ethyl acetate is hydrolyzed and gradually decreases the pH of the solution.[10] So does the addition of extra water. From TEM and SAXS results, the presence of magnetic nanoparticles influences the structural change in the siliceous matrix. Studies on the capture of inclusions during crystallization processes from melts and solutions have been described.[37, 38] Temperature, growth rate, size of inclusions/foreign particles and surface interactions between the growth front and foreign particles are all known to affect crystallization.[37] For instance, if the growth rate is high enough, particles will be captured inside crystals. It is also possible that particles will be repelled from the growing crystal front if the surface compatibility is poor. Even though the exact determination of aforementioned parameters is beyond the scope of this study, the general concept of incorporation of particles into growing crystals can be applied to explain our observations. If the disorder-to-order structure transition is considered as a crystallization process, the front of the ordered region could be thought of as the front of a growing crystal, which repels the foreign particle away to the grain boundaries while retarding crystallization (see Figure 2.6). Completion of the ordering (crystallization) leads to particles that all have the iron oxide at the edges of particles, see Figure 2.3(f)–(h).

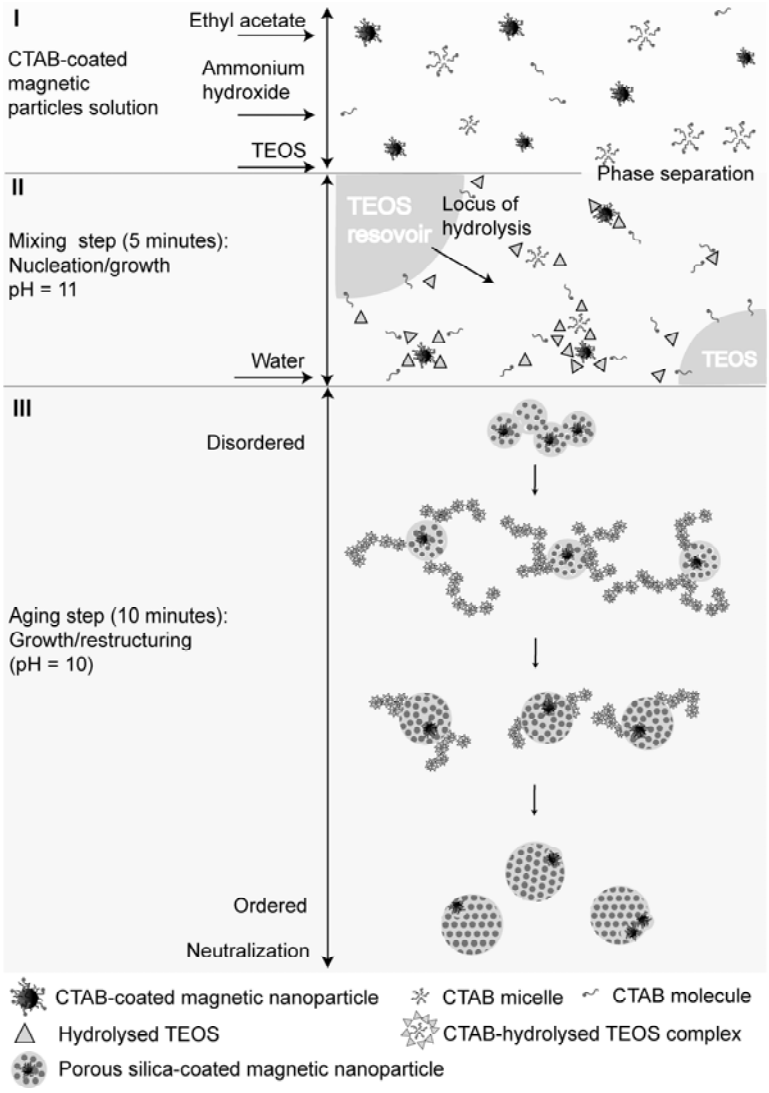

Figure 2.8. Proposed formation mechanism of m-MSNs.

2.5 Conclusion

Mesoporous silica nanoparticles incorporating magnetic nanoparticles have been synthesized at room temperature through a sol–gel synthesis. Capturing the reaction at different time points during the synthesis has helped to elucidate the formation mechanism. TEM and SAXS data show the structure evolution with primary and secondary nucleation steps, from disordered to ordered silica as well as show a change in location of iron oxide particle inclusions from the center to the edge of the silica matrix. Comparison to synthesis of mesoporous silica nanoparticles in the absence of iron oxide reveals that the iron oxide nanoparticles seed the silica formation leading to much smaller particles with lower size dispersion. The iron oxide inclusions further retard the transition from disordered to ordered silica which can be understood by considering the ordering process as a crystallization and the iron oxide as an impurity which is relocated towards grain boundaries (particle edges).

2.6 Disclaimer

The views and conclusions contained in this document are those of the authors and should not be interpreted as necessarily representing the official policies, either expressed or implied, of the US Department of Homeland Security or any of the funding agencies.

2.7 Acknowledgements

This work was supported by the Cornell Center for Materials Research (CCMR) with funding from a PREM program at Norfolk State University through the National Science Foundation (NSF) grant (DMR-0611430), by Department of Energy grant DE-FG02-97ER62443 and by the National Institute of Dental and Craniofacial Research (R21DE018335). This work was further supported by the US Department of

Homeland Security under Cooperative Agreement Number ‘‘2009-ST-108-LR0006’’. The authors thank CCMR for facility support. This work is based upon research conducted at Cornell High Energy Synchrotron Source (CHESS), which is supported by the NSF and the National Institutes of Health/National Institute of General Medical Sciences under NSF award DMR-0225180. T.S. is grateful to the Thai Government Scholarship under the Ministry of Science and Technology.

REFERENCES

1. Stober, W.; Fink, A.; Bohn, E., *Journal of Colloid and Interface Science* **1968,** *26* (1), 62-69.

2. Burns, A.; Ow, H.; Wiesner, U., *Chemical Society Reviews* **2006,** *35*, 1028-1042.

3. Piao, Y.; Burns, A.; Kim, J.; Wiesner, U.; Hyeon, T., *Advanced Functional Materials* **2008,** *18* (23), 3745-3758.

4. Hu, S. H.; Liu, D. M.; Tung, W. L.; Liao, C. F.; Chen, S. Y., *Advanced Functional Materials* **2008,** *18* (19), 2946-2955.

5. Noginov, M. A.; Zhu, G.; Belgrave, A. M.; Bakker, R.; Shalaev, V. M.; Narimanov, E. E.; Stout, S.; Herz, E.; Suteewong, T.; Wiesner, U., *Nature* **2009,** *460* (7259), 1110-1113.

6. Yanagisawa, T.; Shimizu, T.; Kuroda, K.; Kato, C., *Bulletin of the Chemical Society of Japan* **1990,** *63* (4), 988-992.

7. Beck, J. S.; Vartuli, J. C.; Roth, W. J.; Leonowicz, M. E.; Kresge, C. T.; Schmitt, K. D.; Chu, C. T. W.; Olson, D. H.; Sheppard, E. W.; McCullen, S. B.; Higgins, J. B.; Schlenker, J. L., *Journal of the American Chemical Society* **1992,** *114* (27), 10834-10843.

8. Kresge, C. T.; Leonowicz, M. E.; Roth, W. J.; Vartuli, J. C.; Beck, J. S., *Nature* **1992,** *359* (6397), 710-712.

9. Ying, J. Y.; Mehnert, C. P.; Wong, M. S., *Angewandte Chemie, International Edition* **1999,** *38* (1-2), 56-77.

10. Linssen, T.; Cassiers, K.; Cool, P.; Vansant, E. F., *Advances in Colloid and Interface Science* **2003,** *103*, 121-147.

11. Trewyn, B. G.; Whitman, C. M.; Lin, V. S. Y., *Nano Letters* **2004,** *4* (11), 2139-2143.

12. Kim, J.; Lee, J. E.; Lee, J.; Yu, J. H.; Kim, B. C.; An, K.; Hwang, Y.; Shin, C. H.; Park, J. G.; Hyeon, T., *Journal of the American Chemical Society* **2006,** *128* (3), 688-689.

13. Kim, J.; Kim, H. S.; Lee, N.; Kim, T.; Kim, H.; Yu, T.; Song, I. C.; Moon, W. K.; Hyeon, T., *Angewandte Chemie, International Edition* **2008,** *47* (44), 8438-8441.

14. Zhang, L.; Qiao, S. Z.; Jin, Y. G.; Yang, H. G.; Budihartono, S.; Stahr, F.; Yan, Z. F.; Wang, X. L.; Hao, Z. P.; Lu, G. Q., *Advanced Functional Materials* **2008,** *18* (20), 3203-3212.

15. Moller, K.; Bein, T., *Chemistry of Materials* **1998,** *10* (10), 2950-2963.

16. Grun, M.; Lauer, I.; Unger, K. K., *Advanced Materials (Weinheim, Germany)* **1997,** *9* (3), 254-257.

17. Arruebo, M.; Galan, M.; Navascues, N.; Tellez, C.; Marquina, C.; Ibarra, M. R.; Santamaria, J., *Chemistry of Materials* **2006,** *18* (7), 1911-1919.

18. Gov, N.; Borukhov, I.; Goldfarb, D., *Langmuir* **2006,** *22* (2), 605-614.

19. Gu, J.; Fan, W.; Shimojima, A.; Okubo, T., *Small* **2007,** *3*, 1740-1744.

20. Slowing, I. I.; Trewyn, B. G.; Lin, V. S. Y., *Journal of the American Chemical Society* **2007,** *129* (28), 8845-8849.

21. Liu, H. M.; Wu, S. H.; Lu, C. W.; Yao, M.; Hsiao, J. K.; Hung, Y.; Lin, Y. S.; Mou, C. Y.; Yang, C. S.; Huang, D. M.; Chen, Y. C., *Small* **2008,** *4* (5), 619-626.

22. Lee, J. E.; Lee, N.; Kim, H.; Kim, J.; Choi, S. H.; Kim, J. H.; Kim, T.; Song, I. C.; Park, S. P.; Moon, W. K.; Hyeon, T., *Journal of the American Chemical Society* **2010,** *132* (2), 552-7.

23. Nooney, R. I.; Thirunavukkarasu, D.; Chen, Y. M.; Josephs, R.; Ostafin, A. E., *Chemistry of Materials* **2002,** *14* (11), 4721-4728.

24. Nooney, R. I.; Thirunavukkarasu, D.; Chen, Y. M.; Josephs, R.; Ostafin, A. E., *Langmuir* **2003,** *19* (18), 7628-7637.

25. Lin, Y. S.; Haynes, C. L., *Chemistry of Materials* **2009,** *21* (17), 3979-3986.

26. Liong, M.; Lu, J.; Kovochich, M.; Xia, T.; Ruehm, S. G.; Nel, A. E.; Tamanoi, F.; Zink, J. I., *ACS Nano* **2008,** *2* (5), 889-896.

27. Yu, W. W.; Falkner, J. C.; Yavuz, C. T.; Colvin, V. L., *Chemical Communications (Cambridge, United Kingdom)* **2004,** (20), 2306-2307.

28. Fowler, C. E.; Khushalani, D.; Lebeau, B.; Mann, S., *Advanced Materials (Weinheim, Germany)* **2001,** *13* (9), 649-652.

29. Sadasivan, S.; Fowler, C. E.; Khushalani, D.; Mann, S., *Angewandte Chemie, International Edition* **2002,** *41* (12), 2151-2153.

30. Toombes, G. E. S.; Mahajan, S.; Weyland, M.; Jain, A.; Du, P.; Kamperman, M.; Gruner, S. M.; Muller, D. A.; Wiesner, U., *Macromolecules* **2008,** *41* (3), 852-859.

31. Kruk, M.; Jaroniec, M., *Chemistry of Materials* **2001,** *13* (10), 3169-3183.

32. Barrett, E. P.; Joyner, L. G.; Halenda, P. P., *Journal of the American Chemical Society* **1951,** *73* (1), 373-380.

33. Ryoo, R.; Kim, J. M., *Journal of the Chemical Society-Chemical Communications* **1995,** (7), 711-712.

34. Huo, Q. S.; Margolese, D. I.; Ciesla, U.; Demuth, D. G.; Feng, P. Y.; Gier, T. E.; Sieger, P.; Firouzi, A.; Chmelka, B. F.; Schuth, F.; Stucky, G. D., *Chemistry of Materials* **1994,** *6* (8), 1176-1191.

35. Huo, Q. S.; Margolese, D. I.; Ciesla, U.; Feng, P. Y.; Gier, T. E.; Sieger, P.; Leon, R.; Petroff, P. M.; Schuth, F.; Stucky, G. D., *Nature* **1994,** *368* (6469), 317-321.

36. Nooney, R. I.; Dhanasekaran, T.; Chen, Y. M.; Josephs, R.; Ostafin, A. E., *Advanced Materials (Weinheim, Germany)* **2002,** *14* (7), 529-532.

37. Chernov, A. A.; Temkin, D. E.; Mel'nikova, A. M., *Soviet Physics - Crystallography* **1976,** *21*, 369-374.

38. Kliya, M. O.; Sokolova, I. G., *Soviet Physics - Crystallography* **1958,** *3*, 217-221.

CHAPTER 3

HIGHLY AMINATED MESOPOROUS SILICA NANOPARTICLES WITH CUBIC PORE STRUCTURE*

3.0 Abstract

Mesoporous silica with cubic symmetry has attracted interest from researchers for some time. Here, we present the room temperature synthesis of mesoporous silica nanoparticles possessing cubic $Pm\bar{3}n$ symmetry with very high molar ratios (>50%) of 3-aminopropyl triethoxysilane. The synthesis is robust allowing, for example, co-condensation of organic dyes without loss of structure. By means of pore expander molecules, the pore size can be enlarged from 2.7 to 5 nm, while particle size decreases. Adding pore expander and co-condensing fluorescent dyes in the same synthesis reduces average particle size further down to 100 nm. After PEGylation, such fluorescent aminated mesoporous silica nanoparticles are spontaneously taken up by cells as demonstrated by fluorescence microscopy.

* Originally Published as: Teeraporn Suteewong, Hiroaki Sai, Roy Cohen, Suntao Wang, Michelle Bradbury, Barbara Baird, Sol M. Gruner and Ulrich Wiesner. *Highly Aminated Mesoporous Silica Nanoparticles with Cubic Pore Structure*, Journal of the American Chemical Society, *in press*. Reproduced with permission from Journal of the American Chemical Society.

3.1 Introduction

Significant research efforts in recent years have been devoted to the development of nanoparticles for applications in biomedical imaging, sensing, and drug delivery.[1, 2, 3, 4] Nanoparticle architecture and composition are key to the achievable property profiles. Silica is one of the most studied nanoparticle matrix materials due to low toxicity, versatile bulk and surface chemistry, and biocompatibility.[5, 6, 7, 8, 9] Ordered mesoporous silica in particular has attracted considerable interest due to its ability to reversibly load other compounds. It provides high surface area and large pore volume, necessary in sorption and catalysis applications, while maintaining the intrinsic properties of silica.[10, 11] Mesoporous siliceous materials with three-dimensional pore systems, such as MCM-48, provide advantages in diffusion and transport over one-dimensional channel systems such as in MCM-41-type materials.[6, 11, 12]

Among several three-dimensional mesoporous structures reported, mesoporous silica with cubic $Pm\bar{3}n$ symmetry and possessing a cage-type structure that is three-dimensionally interconnected with small open windows is a promising material, for example, as a carrier for biologically active molecules.[12, 13] Compared to cubic MCM-48 materials, only a few studies report on $Pm\bar{3}n$-type silica.[14, 15, 16, 17, 18] Recently, amine functionalized $Pm\bar{3}n$ mesoporous silica prepared from co-condensation of 3-aminopropyl triethoxysilane (APTES) and tetraethyl orthosilicate (TEOS) was reported.[19] Although with 4%, the mole percentage of APTES relative to total silane precursors (TEOS and APTES) was low, this work broadened the composition and functionality range of cage-type mesoporous silica. Cubic $Pm\bar{3}n$ mesoporous silica nanoparticles from high (>50 mol %) amino silane feed have not yet been reported. Furthermore, the existing synthesis protocol of amine containing $Pm\bar{3}n$ mesoporous silica only yielded micrometer-sized particles.[19] This may affect their applicability to

bio-related applications, particularly, cellular uptake, which is known to be strongly size dependent.[20, 21, 22]

Herein, we report the room temperature synthesis of discrete, faceted $Pm\bar{3}n$ highly aminated mesoporous silica nanoparticles (NH_2-MSNs), from 54 mol % APTES. To our surprise, the synthesis protocol is quite robust allowing the co-condensation of other functional moieties in the same synthesis, for example, organic dyes, without appreciable loss of structure control. We further demonstrate that the addition of pore expander 1,3,5-trimethylbenzene (TMB) to the synthesis increases pore size from 2.7 to 5 nm while decreasing overall particle size. Rendering these highly aminated, pore-expanded particles fluorescent by co-condensing organic dyes into the particles reduces particle size even further, down to about 100 nm, the smallest average particle size observed in this study. Finally, using fluorescence microscopy, we show the first results cellular uptake of such highly aminated MSNs after surface PEGylation.

3.2 Results and Discussion

In general, NH_2-MSNs were prepared via base-catalyzed sol-gel silica reactions using hexadecyltrimethyl ammonium bromide (CTAB), TEOS, and high molar amounts of APTES in the presence of ethyl acetate (see Appendix A).[23] Reactions proceeded for 24 h at room temperature. CTAB was removed by either acetic acid extraction or calcination. TEM images of acid-treated materials (Figure 3.1a-c) reveal discrete and well-faceted mesoporous particles. The size of the smallest particles in Figure 3.1a is down to about 100 nm, while the size of the largest particles is above 200 nm. For the larger particles, a truncated-octahedral shape can clearly be discerned from these images. Average particle size, as obtained from TEM image analysis, is about 220 ± 50 nm, which is consistent with the hydrodynamic particle

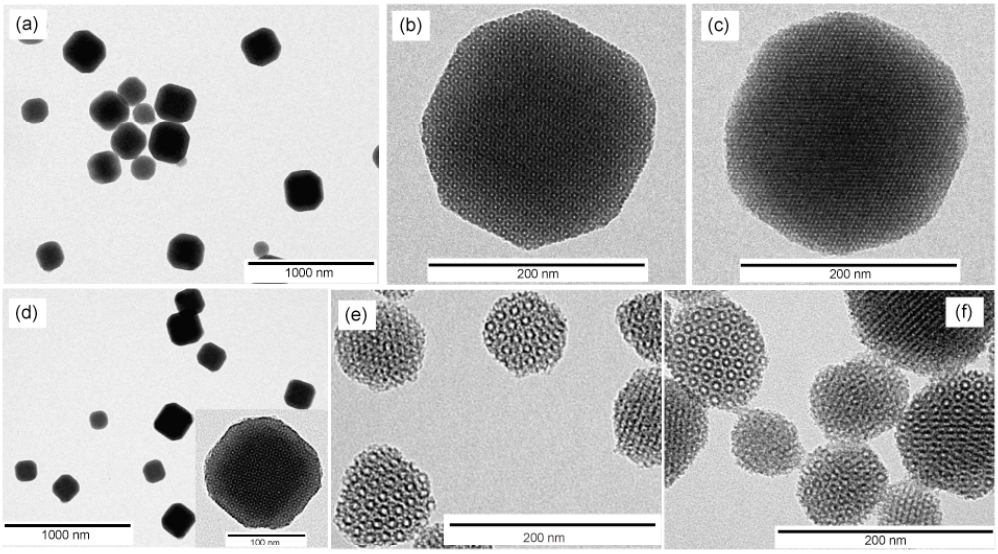

Figure 3.1.TEM images of (a) NH_2-MSNs at low magnification, (b) NH_2-MSN at [100] projection, (c) NH_2-MSN at [111] projection, (d) TRITC-labeled NH_2-MSNs (inset: high magnification image at [100] projection), (e) large-pore NH_2-MSNs, and (f) TRITC-labeled large-pore NH_2-MSNs.

size of 220 nm determined from dynamic light scattering (DLS) (see Appendix A). Two projections of a truncated, octahedrally shaped particle exhibiting four-fold and three-fold symmetries, that is, along the [100] and [111] directions are shown in Figure 3.1, panels b and c, respectively. Both these projections, as well as the particle shape, suggest a cubic structure for these materials.

To further characterize the structure of the particles, small-angle X-ray scattering (SAXS) was employed. SAXS patterns of dried powders of acid extracted and calcined materials are presented in Figure 3.2, panels a and b, respectively. On first inspection, the SAXS pattern of the calcined sample is shifted to higher q-values, where q denotes the scattering vector and is defined as $q = 4\pi\sin\theta/\lambda$ with a scattering angle of 2θ and the X-ray wavelength λ = 1.54 Å. This shift likely results from a contraction of the siliceous matrix induced by further silica condensation upon calcination. Twelve peaks consistent with the (110), (200), (210), (211), (220), (310), (222), (320), (321), (400), (420), and (421) indices of a cubic lattice can be observed in the pattern of the acid-extracted material (Figure 3.2a; see Appendix A for details). Allowed peaks corresponding to $Pm\bar{3}n$ symmetry are indicated in Figure 3.2 by vertical lines. Red lines are the observed peaks, while black lines indicate allowed positions missing in the scattering patterns. Albeit not as well resolved, at least five of the expected peaks for a $Pm\bar{3}n$ lattice can be observed for the calcined material (Figure 3.2b). The pattern in Figure 3.2a was taken at the Cornell High Energy Synchrotron Source (CHESS), while the pattern of the calcined sample was taken at a rotating anode setup. We speculate that the peaks in Figure 3.2b are more poorly resolved than in Figure 3.2a, both because of the intrinsically poorer resolution of the laboratory setup and because the specimen is intrinsically more disordered. The SAXS and TEM results combined are consistent with a cubic $Pm\bar{3}n$ symmetry for the acid extracted sample, with unit cell dimension (a_0) = 9.6 nm. If one assumes that the

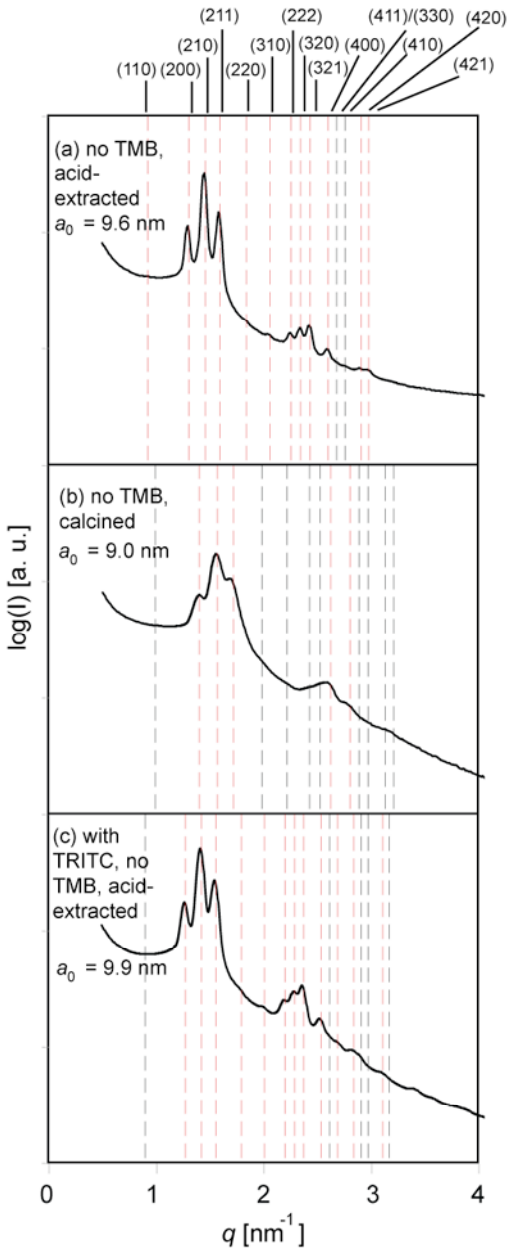

Figure 3.2. SAXS patterns of (a) acid-extracted and (b) calcined NH_2-MSNs and (c) acid-extracted TRITC-labeled NH_2-MSNs.

calcined material has the same symmetry and the strongest peak is the (210) peak, then the unit cell dimension is 9.0 nm.

The use of organosilane at high molar ratio in the co-condensation based sol-gel synthesis usually affects the packing of surfactant-silane complexes and hence causes the formation of disordered mesostructures.[19, 24] In contrast, in the present study, the amino groups are incorporated in the silica matrix without sacrificing pore size and morphology control.[25] High amine content in these particles is reflected by a strongly positive zeta potential of the acid-extracted particles in water, that is, 42 ± 5 mV (see Appendix A). In comparison, the reported zeta potential for non-aminated MCM-41-type MSNs is approximately -35 mV, that is, highly negative as expected from the low isoelectric point (pH 2-3) of pure silica.[26] N_2 sorption isotherms of acid-extracted and calcined mesoporous nanoparticles exhibit a type IV isotherm with small and narrow hysteresis loops at high relative pressure, which are due to incomplete desorption of N_2 from micropores (Figure 3.3a).[10] The BET surface area of the calcined sample is 1264 $m^2 g^{-1}$, and is almost 2 times higher than that of the acid-extracted sample, 674 $m^2 g^{-1}$. Thermogravimetric analysis (see Appendix A) suggests this to be the result of the degradation of the high amounts of organic moieties of APTES. In contrast, the pore sizes calculated using the BJH method of acid-extracted and calcined NH_2-MSNs (Figure 3.3a, inset) are the same, that is, 2.7 nm. The BJH model assumes cylindrical pores and thus underestimates the true pore size. We thus also estimated the pore size as 3.7 (acid) and 3.4 (calcined) nm by a more appropriate geometrical model informed by previous studies, see Appendix A.[27]

To prepare NH_2-MSNs for fluorescence microscopy applications, we synthesized materials with TRITC dye covalently bound to the organically modified silica matrix (see Appendix A for details). Inspection of these materials by TEM again reveals well-faceted nanoparticles and specific projections (Figure 3.1d). SAXS

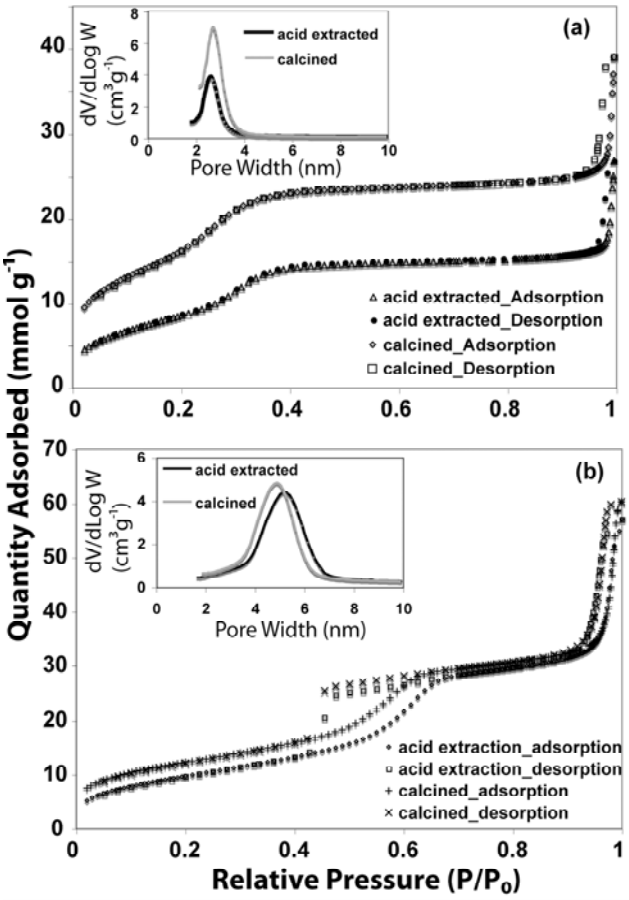

Figure 3.3. N_2 sorption isotherms (inset: BJH pore size distribution from adsorption branches) of (a) template-removed NH_2-MSNs and (b) template-removed large-pore NH_2-MSNs. For each particle case, two data sets are shown corresponding to acid-extracted and calcined samples, respectively.

scattering patterns of acid-extracted samples in dry form (Figure 3.2c) were taken at CHESS. Twelve well-resolved peaks, consistent with the (200), (210), (211), (220), (310), (222), (320), (321), (400), (410), (420), and (421) indices of a cubic $Pm\bar{3}n$ lattice with unit cell dimension (a_0) = 9.9 nm can be observed for this fluorescent material (see below). Comparing Figure 3.1a and 3.1d with Figure 3.2a and 3.2c, the combined TEM and SAXS results suggest that TRITC molecules covalently bound to the silica matrix did not significantly alter the formation of a cubic $Pm\bar{3}n$ particle morphology. Average particle sizes as determined by TEM image analysis and DLS (about 215 ± 45 and 190 nm, respectively) showed slightly smaller particles as compared to non-dye modified NH_2-MSNs, while zeta potentials stayed highly positive (see Appendix A, Table A.1).

It is known that pore sizes in mesoporous silica can be tailored by pore expander molecules.[28] To this end, we prepared large pore NH_2-MSNs with the aid of TMB (see Appendix A). The TEM image in Figure 3.1e suggests that a quasi-periodic structure is preserved under these conditions, but that the resulting particles are smaller than those synthesized in the absence of TMB (compare panel e with panels b and c in Figure 3.1). Average particle sizes as observed from TEM image analysis and DLS are 110 ± 25 and 164 nm, respectively, that is, the TEM image analysis slightly underestimates sizes measured in solution. Repeated efforts to obtain SAXS diffractograms from acid-extracted large pore NH_2-MSNs only resulted in patterns (see Appendix A, Figure A.2a), in which the peaks are far less well resolved than those shown in Figure 3.2a-c, for the particles synthesized in the absence of TMB. Figure A.2a in Appendix A also shows tic marks at the expected peak positions for a $Pm\bar{3}n$ lattice, assuming that the first order maximum is the (210) reflection. The broad second peak in the pattern would then correspond to where the (222), (320), and (321) peaks would appear. If one assumes $Pm\bar{3}n$ symmetry for the TMB acid-

extracted material with strong peak at the (210) position, then the unit cell size for this material is 15.9 nm, that is, significantly larger than for materials synthesized without TMB, *vide supra*.

Zeta potential measurements on large pore NH_2-MSNs gave values comparable to those of materials synthesized in the absence of TMB (43 ± 7 mV). The N_2 sorption isotherms (Figure 3.3b) of acid-extracted and calcined large-pore aminated porous particles exhibit type IV isotherms with hysteresis loops. BET surface areas were determined as 780 m^2 g^{-1} for acid-extracted samples and 990 m^2 g^{-1} for calcined samples. The BJH (geometrical model) pore sizes were 5.3 (7.1) and 5 (6.6) nm for acid-extracted and calcined samples, respectively (Figure 3.3b, inset), that is, significantly larger than without TMB.

Elemental analysis confirmed amine contents as high as 20.45 and 23.38 mol % for aminated and large pore aminated MSNs, respectively (see Appendix A). To the best of our knowledge, this is the highest amine content in ordered and porous silica nanoparticles reported to date.[29, 30] Differences relative to previously reported synthesis protocols that may allow this high amine loading are the use of ethyl acetate and slightly lower pH (pH in our reaction is ~11, see Appendix A).

Intensive research efforts have recently been devoted to the exploration of interactions between silica nanoparticles and cells.[3, 20, 21, 26] To this end, herein, we report the study of endocytosis-mediated internalization of nanoparticles into COS-7 and epithelial cells (SLC-44) using PEGylated and TRITC-labeled NH_2-MSNs and large-pore NH_2-MSNs as imaging probes, respectively. For synthesis details, the interested reader is referred to the Appendix A. TEM images of TRITC-labeled, large-pore NH_2-MSNs (Figure 3.1f) suggest that the combination of covalent incorporation of TRITC molecules into the aminated silica and use of the pore expander TMB did not significantly disturb the formation of a cubic particle structure. Interestingly, the

average particle size as determined by TEM and DLS (see Appendix A, Table A.1) went down to about 100 nm suggesting that the use of dye and pore expander together leads to the smallest sizes observed in this study. This is consistent with a particle size reduction for both of these synthesis variations separately (see Appendix A, Table A.1). A SAXS pattern for this material is depicted in the Appendix A (Figure A.2b) and shows similar features as the diffractogram of large-pore NH_2-MSNs in Figure A.2a.

Additional PEGylation with poly(ethylene glycol) succinimidyl succinate (PEG) prevented particle aggregation, providing good stability in physiological environments.[3, 31] The change in zeta potentials before and after PEGylation from 36.5 ± 6 to -0.5 ± 5 mV for TRITC-labeled NH_2-MSNs and from 32 ± 6 to 6 ± 4mV for TRITC-labeled large-pore NH_2-MSNs confirmed the surface modifications. At the same time through PEGylation, the hydrodynamic particle sizes as determined by DLS slightly increased for both samples (see Appendix A, Table A.1). Confocal microscopy experiments confirm the uptake of normal and large-pore NH_2-MSNs into COS-7 and endothelial cells, respectively. Figure 3.4a,b illustrates the spontaneous cell uptake of PEGylated and TRITC-labeled NH_2-MSNs from the medium and accumulation into discrete cytosolic structures. Cell cross-section images along two orthogonal directions and obtained from z-scans in the microscope shown at the top and on the right confirmed the presence of particles inside cells, most likely in endosomes. The size of particles used in the presented experiments is consistent with fluid phase endocytosis as the main particle uptake pathway. It is interesting to note that no particle aggregation was observed on the cell membrane consistent with successful PEGylation.

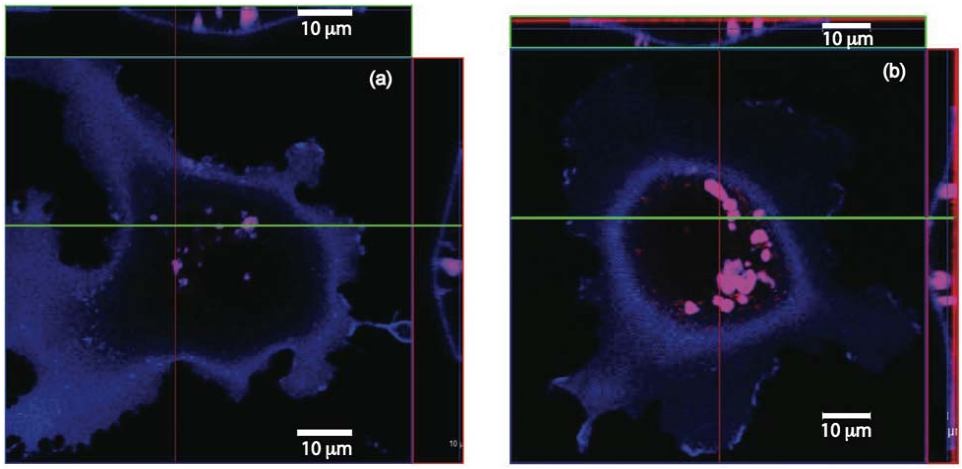

Figure 3.4. Confocal microscopy images of (a) endocytosed PEGylated and TRITC-labeled NH_2-MSNs into COS-7 cells and (b) endocytosed PEGylated and TRITC-labeled, large-pore NH_2-MSNs into epithelial cells. Particles appear in red. Far-red plasma membrane dye (Cell Mask Deep Red, Em/ Ex 660/677 nm) was used to label the cell membrane (blue). Cell cross-section images along two orthogonal directions (red and green lines) are shown at the top and on the right of each image (see text) and corroborate the presence of particles inside the cells. Scale bars are 10 µm.

3.3 Acknowledgment

This work was supported by the Cornell Center for Materials Research (CCMR) with funding from a PREM program at Norfolk State University through the National Science Foundation (NSF) grant (DMR-0611430), by the Department of Energy grant DE-FG02-97ER62443 and by the National Institute of Dental and Craniofacial Research (R21DE018335). We thank the Cornell Universiy KAUST Center for Research and Education for financial support. This work was further supported by the U.S. Department of Homeland Security under Cooperative Agreement Number “2009-ST-108-LR0004”. The authors thank CCMR for facility support. This work is based upon research conducted at the Cornell High Energy Synchrotron Source (CHESS), which is supported by the NSF and the National Institutes of Health/National Institute of General Medical Sciences under NSF award DMR-0225180. T.S. is grateful for a Thai Government Scholarship under the Ministry of Science and Technology.

REFERENCES

1. De, M.; Ghosh, P. S.; Rotello, V. M., *Advanced Materials (Weinheim, Germany)* **2008,** *20* (22), 4225-4241.

2. Park, K.; Lee, S.; Kang, E.; Kim, K.; Choi, K.; Kwon, I. C., *Advanced Functional Materials* **2009,** *19* (10), 1553-1566.

3. Burns, A. A.; Vider, J.; Ow, H.; Herz, E.; Penate-Medina, O.; Baumgart, M.; Larson, S. M.; Wiesner, U.; Bradbury, M., *Nano Letters* **2009,** *9* (1), 442-448.

4. Tan, W. H.; Wang, K. M.; He, X. X.; Zhao, X. J.; Drake, T.; Wang, L.; Bagwe, R. P., *Medicinal Research Reviews* **2004,** *24* (5), 621-638.

5. Zhao, X. J.; Hilliard, L. R.; Mechery, S. J.; Wang, Y. P.; Bagwe, R. P.; Jin, S. G.; Tan, W. H., *Proceedings of the National Academy of Sciences of the United States of America* **2004,** *101* (42), 15027-15032.

6. Burns, A.; Ow, H.; Wiesner, U., *Chemical Society Reviews* **2006,** *35*, 1028-1042.

7. Piao, Y.; Burns, A.; Kim, J.; Wiesner, U.; Hyeon, T., *Advanced Functional Materials* **2008,** *18* (23), 3745-3758.

8. Ow, H.; Larson, D. R.; Srivastava, M.; Baird, B. A.; Webb, W. W.; Wiesner, U., *Nano Letters* **2005,** *5* (1), 113-117.

9. Kim, S.; Ohulchanskyy, T. Y.; Pudavar, H. E.; Pandey, R. K.; Prasad, P. N., *Journal of the American Chemical Society* **2007,** *129* (9), 2669-2675.

10. Wan, Y.; Zhao, D. Y., *Chemical Reviews* **2007,** *107* (7), 2821-2860.

11. Vallet-Regi, M.; Balas, F.; Arcos, D., *Angewandte Chemie, International Edition* **2007,** *46*, 7548-7558.

12. Fan, J.; Yu, C. Z.; Gao, T.; Lei, J.; Tian, B. Z.; Wang, L. M.; Luo, Q.; Tu, B.; Zhou, W. Z.; Zhao, D. Y., *Angewandte Chemie, International Edition* **2003,** *42* (27), 3146-3150.

13. Brohede, U.; Atluri, R.; Garcia-Bennett, A. E.; Stromme, M., *Current Drug Delivery* **2008,** *5* (3), 177-185.

14. Li, J.; Wei, Y.; Deng, Y.; Gu, D.; Yang, X.; Zhang, L.; Tu, B.; Zhao, D. Y., *Journal of Materials Chemistry* **2010,** *20*, 6460-6463.

15. Wang, J.; Zhou, H.; Sun, P.; Ding, D.; Chen, T., *Chemistry of Materials* **2010,** *22* (13), 3829-3831.

16. Che, S.; Sakamoto, Y.; Terasaki, O.; Tatsumi, T., *Chemistry Letters* **2002,** (2), 214-215.

17. Che, S.; Sakamoto, Y.; Terasaki, O.; Tatsumi, T., *Chemistry of Materials* **2001,** *13* (7), 2237-2239.

18. Kim, M. J.; Ryoo, R., *Chemistry of Materials* **1999,** *11* (2), 487-491.

19. Atluri, R.; Sakamoto, Y.; Garcia-Bennettt, A. E., *Langmuir* **2009,** *25* (5), 3189-3195.

20. Vallhov, H.; Gabrielsson, S.; Stromme, M.; Scheynius, A.; Garcia-Bennett, A. E., *Nano Letters* **2007,** *7* (12), 3576-3582.

21. Lu, F.; Wu, S. H.; Hung, Y.; Mou, C. Y., *Small* **2009,** *5* (12), 1408-1413.

22. Jin, H.; Heller, D. A.; Sharma, R.; Strano, M. S., *ACS Nano* **2009,** *3* (1), 149-158.

23. Suteewong, T.; Sai, H.; Lee, J.; Bradbury, M.; Hyeon, T.; Gruner, S. M.; Wiesner, U., *Journal of Materials Chemistry* **2010,** *20* (36), 7807-7814.

24. Huh, S.; Wiench, J. W.; Yoo, J. C.; Pruski, M.; Lin, V. S. Y., *Chemistry of Materials* **2003,** *15* (22), 4247-4256.

25. ^{29}Si NMR data supporting full incorporation will be discussed in detail in a forthcoming publication.

26. Slowing, I.; Trewyn, B. G.; Lin, V. S. Y., *Journal of the American Chemical Society* **2006,** *128* (46), 14792-14793.

27. Ravikovitch, P. I.; Neimark, A. V., *Langmuir* **2002,** *18* (5), 1550-1560.

28. Beck, J. S.; Vartuli, J. C.; Roth, W. J.; Leonowicz, M. E.; Kresge, C. T.; Schmitt, K. D.; Chu, C. T. W.; Olson, D. H.; Sheppard, E. W.; McCullen, S. B.; Higgins, J. B.; Schlenker, J. L., *Journal of the American Chemical Society* **1992,** *114* (27), 10834-10843.

29. Burleigh, M. C.; Markowitz, M. A.; Spector, M. S.; Gaber, B. P., *Chemistry of Materials* **2001,** *13* (12), 4760-4766.

30. Burleigh, M. C.; Markowitz, M. A.; Spector, M. S.; Gaber, B. P., *Journal of Physical Chemistry B* **2001,** *105* (41), 9935-9942.

31. Kim, J.; Kim, H. S.; Lee, N.; Kim, T.; Kim, H.; Yu, T.; Song, I. C.; Moon, W. K.; Hyeon, T., *Angewandte Chemie, International Edition* **2008,** *47* (44), 8438-8441.

CHAPTER 4

STRUCTURE TRANSFORMATION IN THE SYNTHESIS OF AMINATED MESOPOROUS SILICA NANOPARTICLES [*]

4.0 Abstract

We report the formation of aminated mesoporous silica nanoparticles (NH_2-MSNs) by means of co-condensation of different molar ratios of tetraethyl orthosilicate (TEOS) and 3-aminopropyl triethoxysilane (APTES). The resulting materials are characterized by a combination of transmission electron microscopy (TEM), small angle x-ray scattering (SAXS), Fourier transform infrared (FTIR) spectroscopy, thermogravimetric analysis (TGA), and N_2 sorption/desorption measurements. Analysis reveals that an increase in APTES loading (mol%) in the synthesis feed leads to a structural transition in the mesoporous silica nanoparticles from hexagonal (0-49 mol%) to cubic $Pm\bar{3}n$ (54-64 mol%) to disordered at very high APTES loading (69 mol%). Investigation of structural evolution during particle synthesis shows a gradual structural transition from disordered clusters to ordered, but still heterogeneous particles, to fully ordered cubic structures with $Pm\bar{3}n$ lattice. Syntheses at varying pH reveal further details of the structure formation process.

[*] Prepared for Submission as: Teeraporn Suteewong, Hiroaki Sai, Michelle Bradbury, Sol M. Gruner and Ulrich Wiesner. *Structure Transformation in the Synthesis of Aminated Mesoporous Silica Nanoparticles.*

4.1 Introduction

Silica-based ordered mesoporous materials combine advantages of both silica and mesoporous materials. Due to the versatility of silica chemistry, it has been widely used, e.g. to integrate with other materials, such as metal nanoparticles, fluorescent molecules, or rare-earth elements.[1, 2, 3, 4] Mesoporous materials provide large surface area, high pore volume and uniform pore size distributions.[5] Combining aforementioned advantages in both bulk and nano-sized materials, offers characteristics that can be used in a range of applications.[5, 6] Soon after the discovery in the early 1990's[7, 8], scientists have focused on broadening the functionalities of mesoporous silica, such as incorporating or attaching organic molecules.[5, 9]

Mesoporous silica nanoparticles (MSNs) in particular have been drawing attention from researchers in nano-biomedicine as they could potentially be used as cargo delivery vehicles, imaging probes or theranostic materials.[10, 11] Similar to silica nanoparticles, size and stability of particles in physiological media as well as surface properties are crucial in aforementioned applications.[12, 13] Furthermore, pore structure and geometry of MSNs also influence their use.[14] They will influence uptake and release rates of adsorbents as diffusion rates are geometry-dependent.[15, 16] Width of pore entrance and pore/cavity size will limit the size of guest molecules to be carried. Existing groups on particle surface will contribute to adsorption-desorption affinity between adsorbate and adsorbent.[15, 16] Carefully tuning these features is likely a key to success in an application of interest.

There are several reports focusing on the study of surface functionalization and structure control of MSNs.[17, 18, 19, 20, 21] Functionalization of particle surface can be performed either by post-synthetic grafting or by co-condensation with organosilanes.[22] The latter provides uniform surface modification, but can affect shape and morphology of final products at the same time.[17, 18] Use of a high amount of co-

silane precursor often results in loss of hierarchical structure.[17, 23] This is because organosilane molecules can disrupt the packing of surfactants and/or alter the geometry of structure directing micelles, which in return affects the assemblage between silica-micelle complexes.[17, 18] The geometry of surfactant micelles is known to mainly determine the morphology of mesoporous materials.[6] Compatibility between silica precursors is also reported to play a role.[20] Incorporating a desired amount of organosilane into MSNs without rupturing their periodicity is thus a challenge.

Recently, Atluri *et al.* reported the synthesis of micron sized mesoporous silica materials by means of co-condensation between tetraethyl orthosilicate (TEOS) and (3-aminopropyl) triethoxysilane (APTES) yielding a cubic $Pm\bar{3}n$ structure.[23] By varying the molar ratio between cationic surfactant (hexadecyltrimethylammonium bromide; CTAB) and APTES, structures of resulting materials changed from hexagonal to mesocage cubic with $Pm\bar{3}n$ symmetry. Even though low concentrations of APTES were used and only one ratio led to the formation of the $Pm\bar{3}n$ structure, this work opened the possibility of the direct synthesis of cubic MSNs containing organic moieties.

Bulk mesoporous cubic $Pm\bar{3}n$ silica has large pore cages, which are 3-dimensionally inter-connected by small windows.[16] Among ordered mesoporous materials it thus would be a particularly interesting architecture for nano-biomedical applications if it were available in the form of nanoparticles. To this end, we have previously reported the synthesis of highly aminated (from 54 mole % APTES loading in the synthesis feed) truncated-octahedral mesoporous silica nanoparticles with $Pm\bar{3}n$ lattice symmetry.[24] In the present work, we give a full account of these results and study the effect of increasing amounts of APTES in the synthesis feed on the formation of aminated mesoporous silica nanoparticles (NH_2-MSNs). We show that upon an increase of APTES concentration in the feed, a morphological transition from

hexagonal to cubic $Pm\bar{3}n$ is observed. High amounts of APTES can be accommodated in the synthesis without loss of the ordered structure. A combination of transmission electron microscopy (TEM), small-angle x-ray scattering (SAXS), Fourier transform infrared (FTIR) spectroscopy, thermogravimetric analysis (TGA) and N_2 sorption measurements are used for NH_2-MSN characterization. Finally, in order to elucidate the formation mechanism of cube-shaped $Pm\bar{3}n$ NH_2-MSNs, materials obtained at different time points in the synthesis are characterized by TEM and SAXS, while additional syntheses at different pH reveal influences of reaction rates on particle synthesis.

4.2 Experimental Section

4.2.1 Materials

Hexadecyltrimethylammonium bromide (apprx. 99%), ethyl acetate (EtOAc, ACS grade), tetraethyl orthosilicate (TEOS, ≥99%, GC), (3-aminopropyl) triethoxysilane (APTES, > 95%), ammonium hydroxide (NH_4OH, 29%), acetic acid (glacial), hydrochloric acid (36.5-38%), ethanol (absolute, anhydrous) and deionized water (Milli-Q, 18.2 MΩ-cm) were used as obtained without further purification.

4.2.2 Synthesis of Aminated Mesoporous Silica Nanoparticles from Different APTES Concentrations

EtOAc, NH_4OH and a mixture of silane precursors (TEOS and APTES) were sequentially added into an aqueous solution of hexadecyltrimethylammonium bromide (CTAB) (54.8 mM) and stirred for 5 minutes. Additional water was then added into the reaction before leaving the solution overnight under stirring. After 24 hours, the reaction solution was neutralized using hydrochloric acid solution (2 M). The sample was cleaned by centrifugation and re-dispersed in ethanol. CTAB was removed by

acid extraction using an acetic acid/ethanol mixture (95/5 v/v). Samples were stirred for 30 minutes, before centrifugation to remove CTAB and acetic acid. Every step was performed at room temperature. Throughout this paper, we will refer to these materials as X-NH_2-MSNs, where X is the mol% of APTES (with respect to total silane used) loaded in the synthesis. The amount of TEOS and APTES were varied, while all other chemicals were kept constant for all samples. For example, the volumetric ratio in milliliters of chemicals used in the synthesis of 54-NH_2-MSNs was 1 CTAB (aq):0.045 TEOS:0.055 APTES:0.54 NH_4OH:0.176 EtOAc:27.38 H_2O. Concentration of NH_4OH in the synthesis is 207.5 mM.

Control sample was prepared in the same way as described for the synthesis of NH_2-MSNs, but without the addition of APTES.

To investigate the effect of solution pH on the structure of mesoporous silica with 54 mol% APTES loading, concentrations of NH_4OH were varied. In addition to a concentration of 207.5 mM used in the syntheses described above, two further concentrations of NH_4OH, i.e., 103.75 and 409 mM, were chosen in the study.

4.2.3 Particle Characterizations

Transmission electron microscopy (TEM) images were obtained with a FEI Tecnai T12 Spirit microscope operated at an acceleration voltage of 120kV. SAXS patterns were obtained on a home-built beamline as previously described[25] with a sample-to-detector distance of 25 cm and at the G1 beamline at the Cornell High Energy Synchrotron Source (CHESS) with a beam energy of 9.5 keV and a sample to detector distance of 35 cm.[26] All samples were in dry form, with CTAB removed by acid extraction (vide supra). Nitrogen physisorption isotherms of dried samples were obtained with a Micromeritics ASAP2020 physisorption instrument. The particles exhibited nitrogen sorption isotherms of type IV according to BDDT classification.

Surface areas were determined according to the Brunnauer-Emmett-Teller (BET) method.[27] The BET surface area analysis was performed in the range between 0.042 and 0.095. Calculation of the pore size distributions from the adsorption branches of the isotherms was performed according to the Barrett-Joyner-Halenda[28] (BJH) method and a geometrical model.[29] Thermogravimetric analysis (TGA) was conducted on a TA instruments Q500 thermogravimetric analyzer. All measurements were taken from room temperature to 650 ^{o}C under nitrogen flow. Infrared spectra were measured on a Bruker Optics-Vertex 80V equipped with a transmission holder under vacuum. FT-IR spectra were recorded in the frequency range of 4000-400 cm^{-1}, and 128 scans at a resolution of 4 cm^{-1} were collected for one spectrum. Measurements were performed on KBr (blank) pellets and sample pellets containing 1 wt% samples in KBr.

4.3 Results and Discussion

Incorporating organic moieties into mesoporous silica particles via co-condensation of different types of silane precursors is often used as it is a simple one-pot process and provides a uniform distribution of organic functionality. In the present work, NH_2-MSNs obtained from different amounts of APTES (10-69 mol%) as feed were synthesized in this way at room temperature using APTES and TEOS as precursors. Figures 4.1 (a-i) show TEM images of control and X-NH_2-MSNs after removal of CTAB. As the amount of APTES in the starting solutions increased, the structure of the resulting NH_2-MSNs changed from what looks like hexagonal (Figure 4.1(a-f), 0-49 mol%) to cubic (Figure 4.1(g-h), 54-64 mol%) and finally to disordered structures (Figure 4.1i, 69 mol%). At the same time the shapes of particles varied from oval-like in the control samples to one-dimensionally elongated particles in the presence of moderate amounts of APTES (10-49 mol%). A further increase in the amount of APTES led to the formation of octahedrally truncated particles at 54 mol%

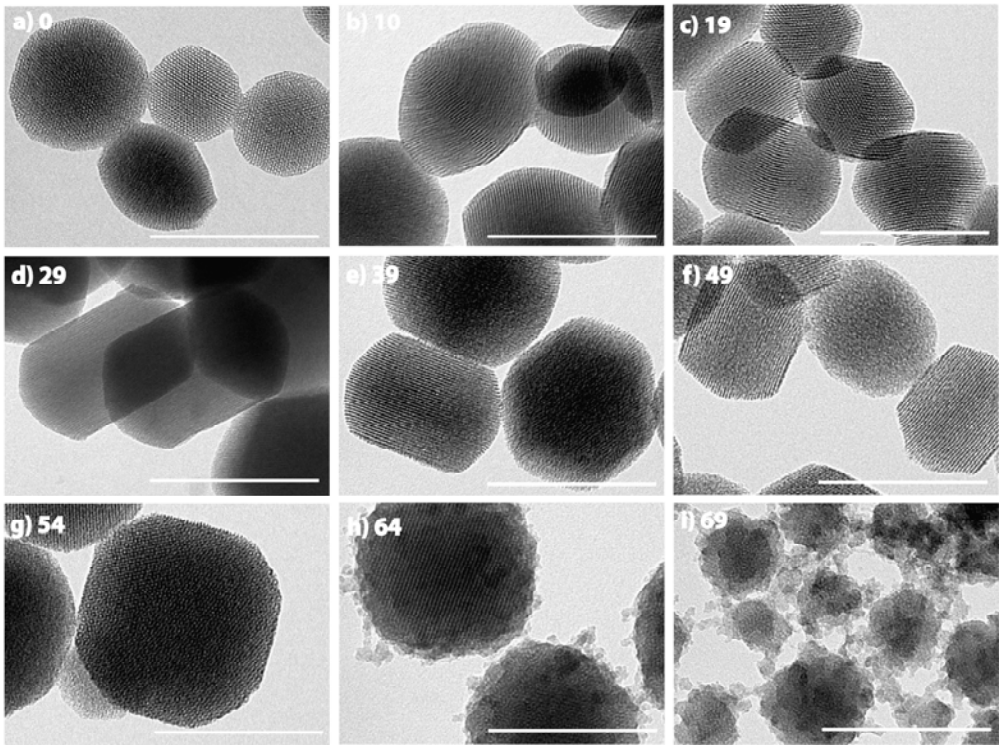

Figure 4.1. TEM images of acid-extracted samples of (a) control and X-NH_2-MSNs made from (b) 10,(c) 19, (d) 29, (e) 39, (f) 49, (g) 54, (h) 64 and (i) 69 mol% APTES in the reaction feed. All scale bars are 200 nm.

and cube-like shapes at 64 mol% APTES. Comparing TEM images of 54- and 64-NH_2-MSNs (Figure 4.1(g-h)), reveal that while both samples are similar in shape and structure, 64-NH_2-MSNs has less facets and a rough surface from additional small silica nanoparticles. At even higher concentrations of APTES (see Figure 4.1i, 69 mol% APTES), the resulting materials are disordered and irregular in shape. Clusters of silica nanoparticles around the larger porous particles are also observed, suggesting that the particle formation under these conditions is retarded. In addition, the yield of this sample was very low. Based on the TEM analysis and consistent with a previous report[30], the two following major effects are induced by the presence of increasing amounts of APTES: i) APTES molecules induce a transformation of particle structure and shape and ii) large amounts of APTES slow down the rate of particle formation.

The transformation of particle structure was corroborated by SAXS measurements. SAXS scattering patterns shown in Figure 4.2 were taken from dried samples after removal of surfactant templates by acid extraction as described in the Experimantal Section. Here, q denotes the scattering vector and is defined as $q = (4\pi\sin\theta)/\lambda$ with a scattering angle 2θ and the x-ray wavelength, $\lambda = 1.54$ Å. SAXS data are consistent with a hexagonal lattice for samples made from 0-49 mol% APTES in the reaction feed as indicated by a set of peaks at q = 0.16, 0.27 (0.28 for control), 0.31 (0.32 for control) and 0.41 (0.43 for control) Å. These reflections can be indexed as 10, 11, 20, 21 and 30 reflections. Samples 49-NH_2-MSN only showed 3 peaks indexed as 10, 11 and 20. In SAXS diffractograms of 54- and 64-NH_2-MSNs, six well-resolved peaks are observed. They can be indexed as 200, 210, 211, 222, 320 and 321 reflections of a cubic lattice with $Pm\bar{3}n$ symmetry. Thus, even thought the TEM image of 64-NH_2-MSNs (Figure 4.1h) does not exhibit well-defined particle shapes as observed for sample 54-NH_2-MSN (Figure 4.1g), the SAXS scattering patterns of both samples point to the same structure. Higher ordered peaks of 64-NH_2-MSNs were

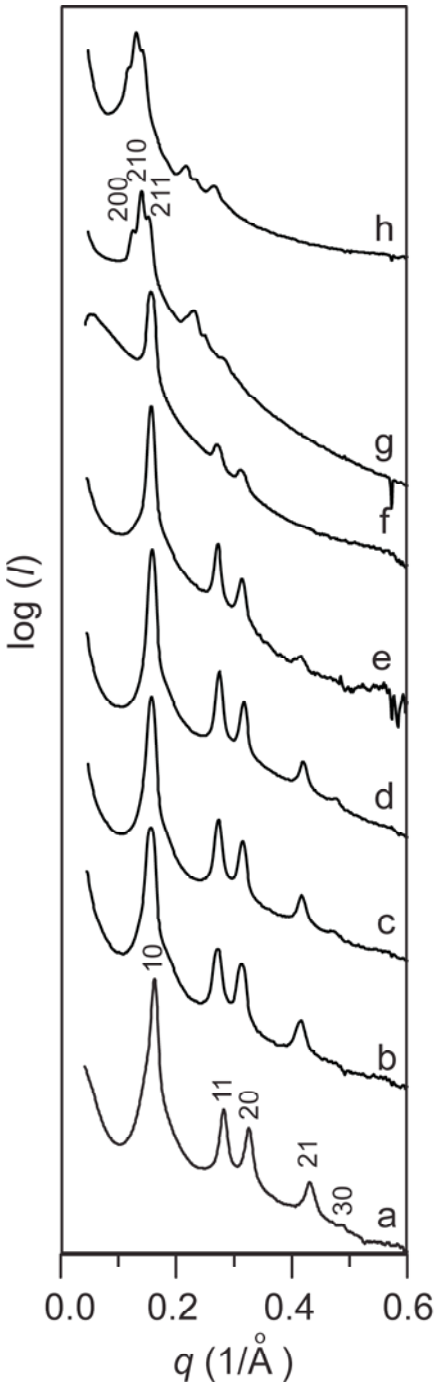

Figure 4.2. SAXS diffractograms of acid-extracted samples of (a) control and NH_2-MSNs made from (b) 10, (c) 19, (d) 29, (e) 39, (f) 49, (g) 54 and (h) 64 mol % APTES in the reaction feed.

slightly shifted to lower *q* values as compared to those of 54-NH_2-MSNs. Both TEM and SAXS analyses consistently suggest a morphology transition upon the addition of more and more APTES in the reaction feed, implying that the organization of surfactant molecules into micelles or silane-surfactant micelle complexes is affected by the presence of organosilane, APTES.[17, 18, 23]

There are several reports on organically functionalized mesoporous silica, both in bulk and particle form, using the co-condensation method in basic condition, especially using APTES as co-silane precursor.[17, 18, 19, 20] In general, the hydrophilicity of the organosilane in a given condition influences morphology, shape, size and degree of functionalization of the resulting mesoporous silica materials. The pKa of APTES is 10.6, so a large number of amine groups are expected to be neutral during the synthesis described here (pH ≈ 11). It is possible that organic moieties, i.e., the aminopropyl groups, intercalate into the hydrophobic micelle core and tailor the packing of the CTAB molecules.[23] The organization of surfactant molecules into a corresponding micelle structure can be rationalized by considering a packing parameter, $g = V/la_0$, where V is the volume of hydrophobic surfactant chains, l is the surfactant chain length, and a_0 is the effective area of the hydrophilic head group of the surfactant molecule at the interface.[31] This parameter could be adopted to rationally predict structures of mesoporous materials.[5, 6] The g value relates to the surface curvature of micelles. The structural transition from hexagonal (Figure 4.1(a-f)) to $Pm\bar{3}n$ (Figure 4.1(g-h)) is correspondent to a decrease in packing parameter or increase in surface curvature of micelles.

To qualitatively determine the amount of APTES incorporated in the organically-modified mesoporous particles, FTIR spectroscopy and TGA were conducted on control and X-NH_2-MSNs, where X = 10-54 mol%, after CTAB removal. Specific peaks in FTIR spectra are evidence for the presence of specific

organic functionalities, and the corresponding intensities are a measure of their concentration. In this way, FTIR spectra can qualitatively indicate the amount of APTES integrated into the silica framework. FTIR spectra of control and X-NH_2-MSNs after normalization to the Si-O-Si peak at 1087 cm^{-1} of the control sample are shown in Figure 4.3. The spectrum of the control sample has high intensity peaks at 948 and 3450 cm^{-1} (Si-OH) and at 1087 cm^{-1} (Si-O-Si). The intensities of these peaks become lower in amine-containing materials. All aminated materials exhibit the appearance of additional peaks at 1560 and very board peaks from 2800-3300 cm^{-1} characteristic for the N-H bending and stretching vibrations of primary amines, respectively. This indicates the presence of APTES in the acid-treated NH_2-MSNs. To semi-quantitatively analyze APTES content between samples, we compared the peak intensities of the N-H bending vibration at 1560 cm^{-1} relative to those of Si-O-Si at 1087 cm^{-1} in the same sample. Figure 4.4 presents the plot of peak ratio of the N-H bending/Si-O-Si stretching for different mol % of APTES in the synthesis. As expected, the peak ratio monotonically increases with the feed concentration of APTES, suggesting that the amount of APTES co-condensed with TEOS is roughly proportional to the initial concentration.

Thermogravimetric measurements of all acid-extracted samples were conducted from room temperature to 650 ^oC under nitrogen flow. TGA curves of control samples (0-NH_2-MSNs) before and after template removal are presented in Appendix B (Figure B.1). As-made MSNs exhibited a weight loss of about 7% at temperatures lower than 120 ^oC, attributed to the loss of small amounts of residual ethanol and moisture adsorbed on the materials surface. This is followed by a 10-12% weight loss from 120-300 ^oC due to surfactant decomposition.[19] At even higher temperatures around 450-600 ^oC, there was another weight loss of 2-4%, which most likely comes from further co-condensation of the silica matrix. After CTAB removal,

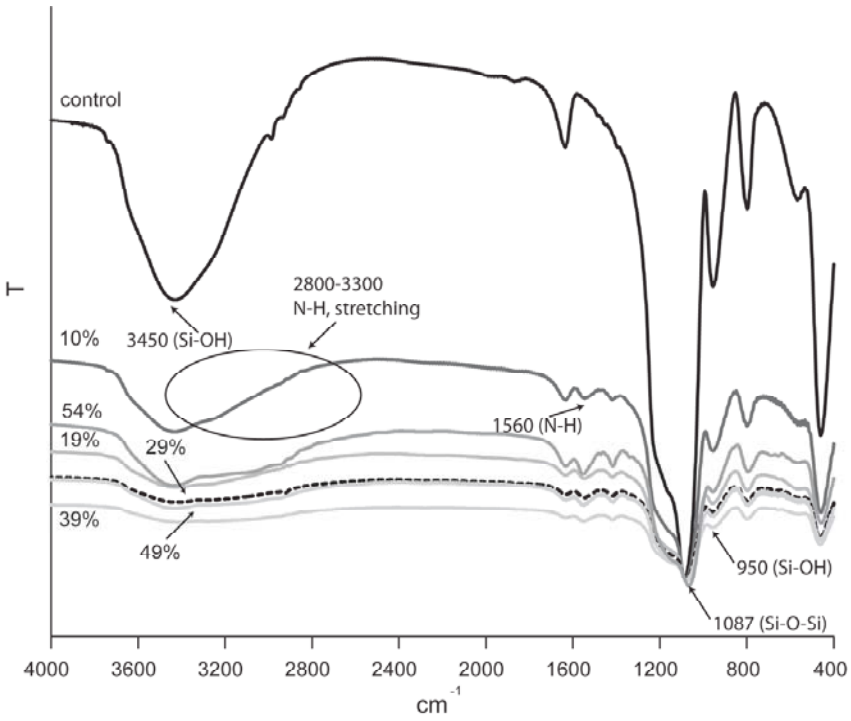

Figure 4.3. FT-IR spectra of acid-extracted control sample and NH_2-MSNs obtained from different mol % APTES in the reaction feed (10-54).

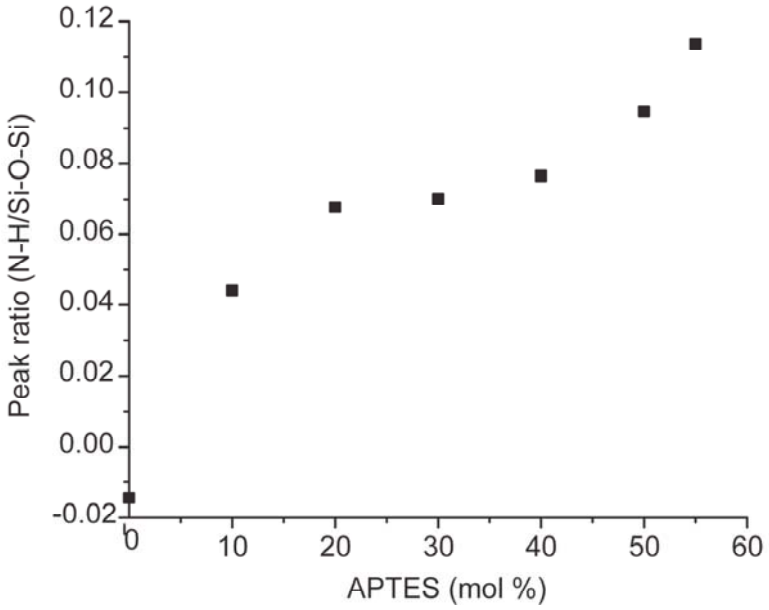

Figure 4.4. Peak intensity ratios of N-H bending to Si-O-Si stretching vibrations of acid-extracted control samples and NH_2-MSNs obtained from different mol % APTES (10-54) in the reaction feed.

the TGA curve of MSNs showed a similar temperature dependence, except that the weight loss around 250 ^{o}C with only 3% was significantly reduced, as expected. The weight loss curves of different acid-extracted NH_2-MSNs shown in Appendix B (Figure B.2) all also exhibited three different decomposition steps albeit with different temperature dependence. Most importantly, the decomposition temperature range associated with APTES is very broad from about 250-600 ^{o}C. In general, the three weight loss regimes observed in the TGA profiles most likely originate from (i) loss of ethanol and moisture (20-80 ^{o}C), (ii) residual CTAB removal/decomposition (80-150 ^{o}C), and (iii) APTES decomposition plus dehydration of surface hydroxyl groups (>250 ^{o}C).[19, 20] The large amount of weight loss at temperatures below about 100 ^{o}C seems to reflect the increasing hydrophilicity of the materials with increasing APTES content.[20] The residual weight (%) at 645 ^{o}C (see Table 4.1) relates qualitatively to the loading concentration of APTES.

Nitrogen sorption measurements were performed on acid-extracted materials (Table 4.1). All samples exhibit type IV isotherms (see Appendix B, Figure B.3). Compared to the control (0-NH_2-MSNs), the addition of APTES results in a decrease in BET surface area for all NH_2-MSNs as previously reported for organically modified mesoporous silica.[20] BJH pore sizes are similar for all samples irrespective of structure, except for sample 29-NH_2-MSNs, which for unknown reasons shows somewhat smaller pores. The BJH model assumes cylindrical pores and thus underestimates the true cavity size of mesoporous materials exhibiting cubic $Pm\bar{3}n$ structure. Table 4.2 shows the estimated spherical cavity size of 54-NH_2-MSNs as 3.87 nm as derived from a geometrical model.[24, 29] The pore size of 64-NH_2-MSNs could not be determined. A significant decrease in BET surface area for 64-NH_2-MSNs might be due to the presence of small silica nanoparticles around larger mesoporous particles as observed in TEM.

Table 4.1. BET surface area, BJH pore size, unit cell size (*a*) and residual inorganic weight percentage determined by thermogravimetric analysis of acid-extracted control samples and NH_2-MSNs obtained from different mol % APTES in the reaction feed.

Samples	APTES (mol%)[a]	a_{100} (nm)	N_2 sorption		[c] wt% residue
			BET surface area (m^2/g)	BJH pore size (nm)	
Control	0	4.46	1122.7	2.7	81.1
10-NH_2-MSN	9.58	4.66	798.1	2.6	80.7
19-NH_2-MSN	19.24	4.62	984.4	2.6	72.5
29-NH_2-MSN	29.00	4.59	893.5	2.3	70.6
39-NH_2-MSN	38.86	4.62	811.8	2.7	71.6
49-NH_2-MSN	48.80	4.65	807.2	2.7	70.5
54-NH_2-MSN	53.81	9.97[b]	673.7	2.7	65.6
64-NH_2-MSN	63.90	10.6[b]	457.6	n/a	n/a
69- NH_2-MSN	68.98	n/a	n/a	n/a	n/a

[a] mol% of APTES loaded in synthesis conditions.
[b] unit cell calculated from the peak indexed as 200 reflection.
[c] weight percentage of residue at 645 ^oC determined by thermogravimetric analysis.

Table 4.2. Estimated spherical cavity size (D_{me}) and average wall thickness (h) for 54-NH_2-MSN sample. The cubic lattice constant, a, was determined from SAXS, and the mesoporosity, ε_{me}, was estimated from the nitrogen adsorption profile.

sample	a_{200} (nm)	ε_{me}	D_{me} (nm)	h (nm)
54-NH_2-MSN	9.97	0.2457	3.87	3.96

Among all samples containing different amounts of APTES, the 54-NH_2-MSNs are particularly interesting as they exhibit as structure with cubic $Pm\bar{3}n$ symmetry and a fairly regular, truncated octahedral shape. The following discussion will thus entirely focus on these materials. The formation mechanism of cubic-type morphologies is more complicated than that of MCM-41 type structures.[32] Acid-catalyzed syntheses of $Pm\bar{3}n$ mesoporous silica from cationic surfactants, referred to as SBA-1, have been more intensively explored than the corresponding base-catalyzed systems, referred to as SBA-6. Furthermore, only few reports on organically modified micron-sized $Pm\bar{3}n$ mesoporous silica have been published.[21, 23] To better understand the highly aminated cubic $Pm\bar{3}n$ mesoporous silica nanoparticles prepared in our approach, we studied the formation mechanism by looking at particle structure at different time points in the synthesis.

To this end, after chemical reagents were mixed for 5 minutes and water was added into the reaction, aliquots were taken out at different time points after water addition. Each aliquot was neutralized to halt ongoing chemical processes. The surfactant template was then removed by acid extraction. TEM images of 54-NH_2-MSNs at different reaction times prepared in this way are shown in Figure 4.5. Similar to what we reported earlier[30], clusters of small silica nanoparticles are first formed and a structural transition from disordered to ordered mesostructures as a function of reaction time is observed.[18, 30] At very early stages (2 minutes), aggregates of small silica nanoparticles are found. At 5 minutes, a few larger, about 100 nm-sized objects can already be found among a large number of small silica nanoparticles (≈ 5-10 nm). Between 8-20 minutes, more and more of such larger particles occur that seem to be assembled from loose packs of smaller silica nanoparticles. Figure 4.6 shows (a) low and (b) high magnification TEM images taken at the 8 minute time point. Some degree of structural periodicity within the particles can clearly be discerned in Figure 4.6b,

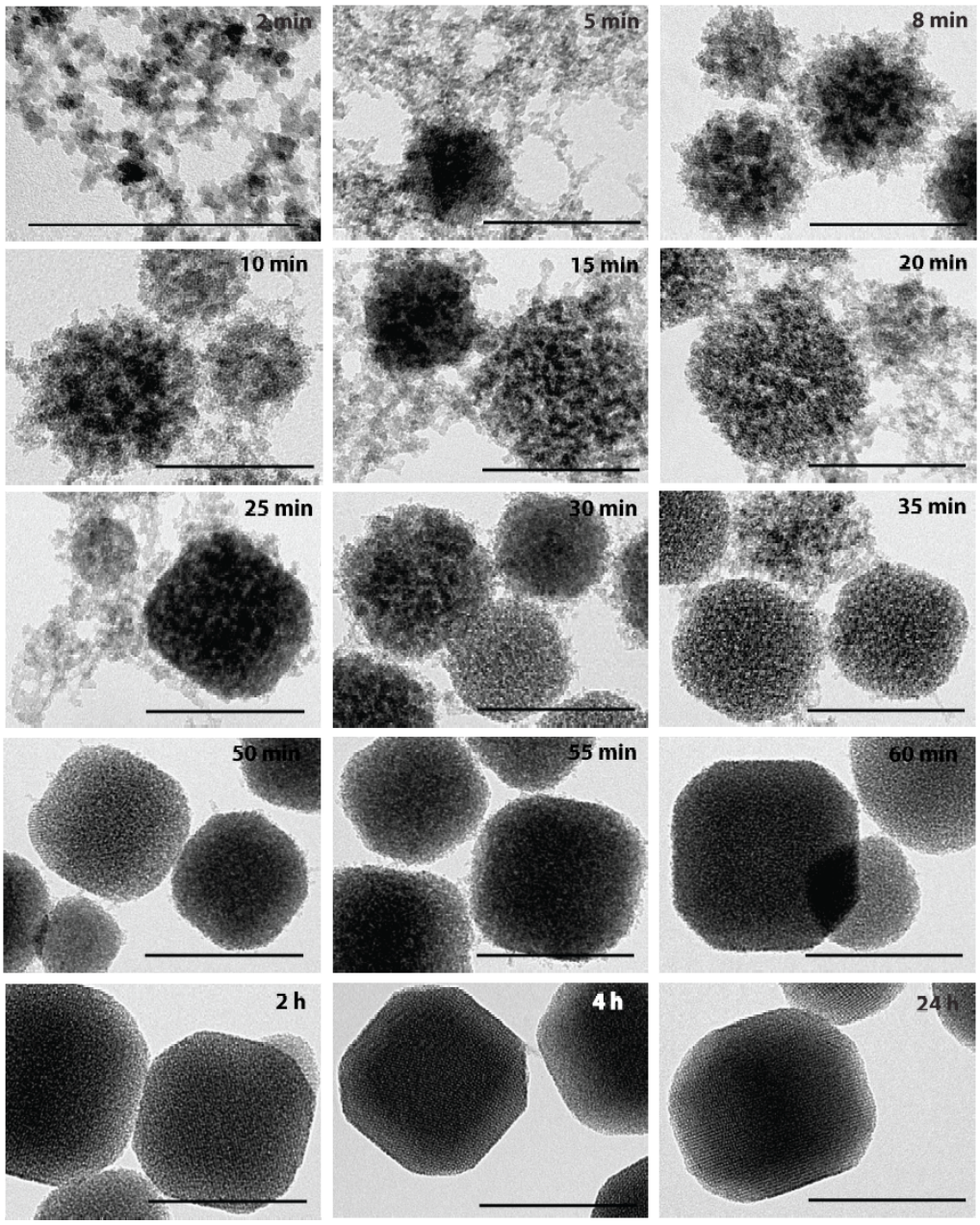

Figure 4.5. TEM images of 54-NH_2-MSNs taken at different time points in the synthesis after removal of CTAB. All scale bars are 200 nm.

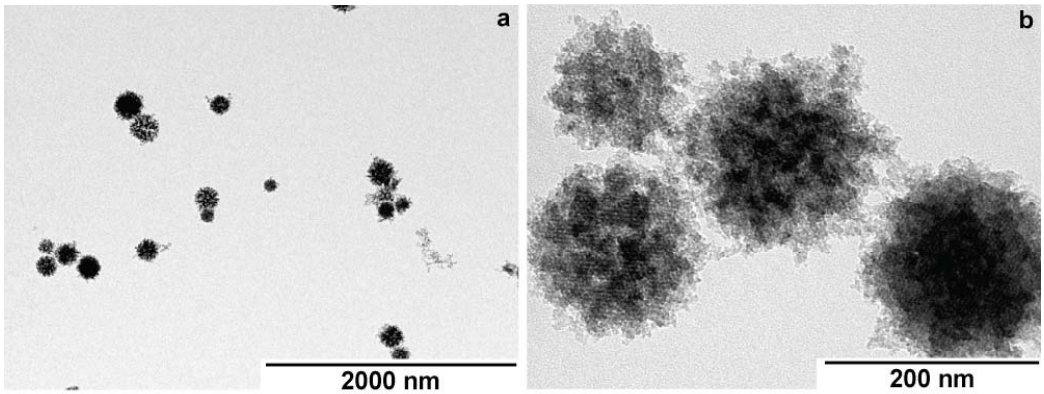

Figure 4.6. TEM images at (a) low and (b) high magnifications of 54-NH_2-MSNs after CTAB removal taken at the 8 minute reaction time point. All scale bars are 200 nm.

even though the overall structure is rather heterogeneous with significant density variations within the particles and a rather ill defined particle surface topology. Cube-shaped particles are clearly observed at around 15-20 minutes. The number of octahedrally shaped MSNs increases as the reaction time proceeds, while at the same time the amount of primary silica nanoparticles goes down (compare images in Figure 4.5 after 5 and 55 minutes). This observation can be rationalized by an Ostwald-ripening type particle growth mechanism, i.e., larger particles grow at the expense of smaller particles. No significant change is observed beyond 2 hours of aging time, at which point the particle structure is fully developed.

SAXS scattering patterns of 54-NH_2-MSNs taken at different synthesis time points are shown in Figure 4.7. Patterns of samples taken at 2-3 minutes show no structural scattering peak. Samples taken from 5-30 minutes show a broad hump around q = 0.14 $Å^{-1}$. At 35 minutes, small peaks appear at q = 0.144 and 0.16 $Å^{-1}$. The intensity of these two peaks becomes more pronounced as time progresses. After a reaction time of 60 minutes, a third peak at q = 0.13 $Å^{-1}$ appears. These three peaks can be assigned as 200, 210 and 211 reflections of a cubic lattice. After 2 hrs, additional higher ordered peaks occur also consistent with $Pm\bar{3}n$ symmetry. In order to further corroborate the cubic pore structure, Figure 4.8 shows a series of TEM images of a specific particle of a 54-NH_2-MSN batch that has gone through the full (i.e. 24 hours) reaction time taken at different rotation angles. Tilting the octahedrally shaped particle by different angles, several projections corresponding to cubic $Pm\bar{3}n$ structure are revealed including [111], [110] and [100], thus corroborating the structural assignment from SAXS.

As previously mentioned, the current challenge in the synthesis of organically modified ordered MSNs via co-condensation is the limited amount of organosilane, in this case APTES, being incorporated. Primary amine groups of APTES can be either

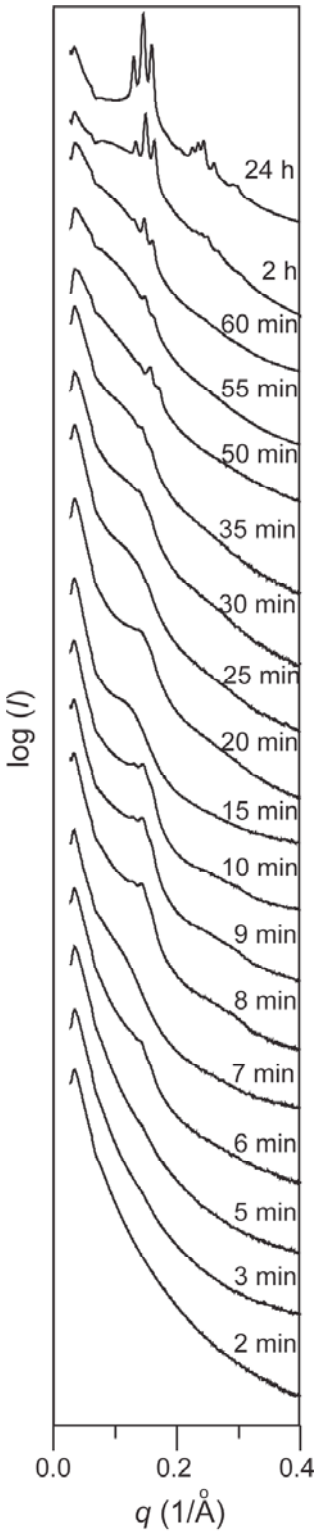

Figure 4.7. SAXS diffractograms of 54-NH_2-MSNs after CTAB removal taken at different time points in the particle synthesis.

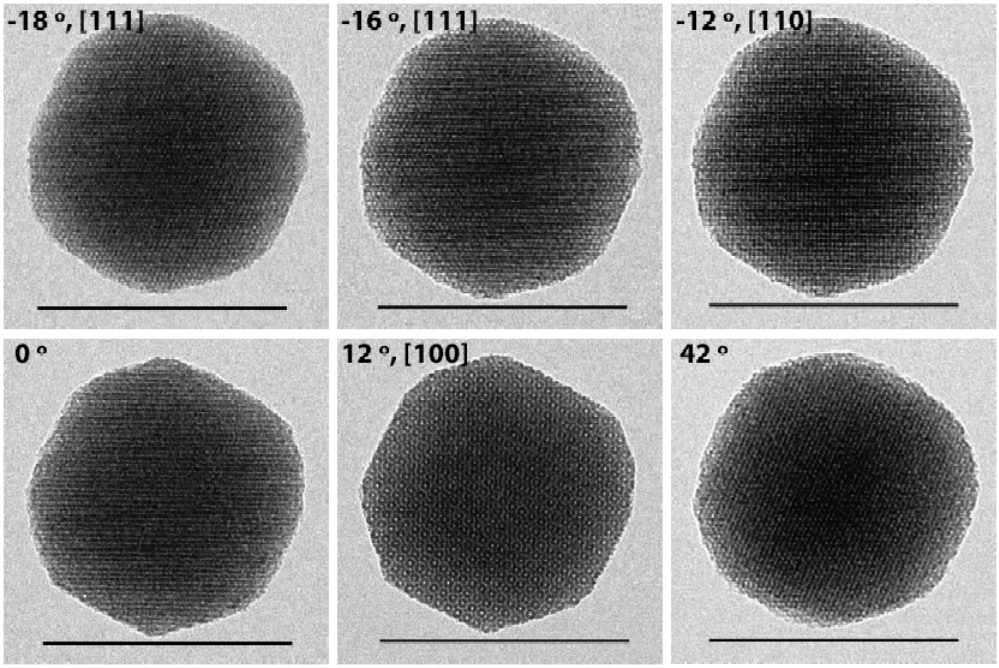

Figure 4.8. A series of TEM images of a particle of 54-NH_2-MSNs after removal of CTAB taken at different tilting angles in the electron microscope. All scale bars are 200 nm.

in protonated or in deprotonated (neutral) form, depending on the pH of the synthesis environment. The majority of amine groups, in the synthesis conditions used here, is expected to be in neutral form as the solution pH is above their pK_a. The aminopropyl moieties of the APTES molecules can then intercalate into the hydrophobic micelle cores, which consequently alters the curvature of the micelles from low (10-49 mol% APTES) to high surface curvature (54-64 mol% APTES), favoring the formation of a cubic morphology.[23, 31, 32, 33, 34] In order to support this suggested mechanism, we varied the pH of the synthesis solutions by changing the concentration of NH_4OH from the original condition (207.5 mM). The pH of solutions containing (a) 103.75 and (b) 409 mM NH_4OH were 10 and 11, respectively. Though there was not significant change in solutions pH, the equilibrium of amino groups in APTES between protonated and deprotonated states was affected. Corresponding TEM images of 54-NH_2-MSNs using different amounts of NH_4OH are shown in Figure 4.9 (a-b). While the structures of both samples are similar, size and shape of the resulting particles are different. At pH 10, a large number of amino groups are expected to be in protonated form. The probability that APTES molecules would intercalate into micelles is then low as a result of the electrostatic repulsion with the cationic head groups of the surfactants. Surprisingly, NH_2-MSNs with cubic shape and structure were obtained under these conditions, though the shape is slightly irregular. These observations suggest that the effects may be more subtle than a simple APTES induced change in micelle geometry.

Aminated materials synthesized at lower catalyst content or lower pH (103.7 mM NH_4OH) have considerably smaller particle size while the shape is cubic-like. In the higher pH system (409 mM NH_4OH), particles are larger in size and exhibit a higher number of well-defined facets. These results suggest that condensation rates of silica are different in these two systems and determine hence the final size and details

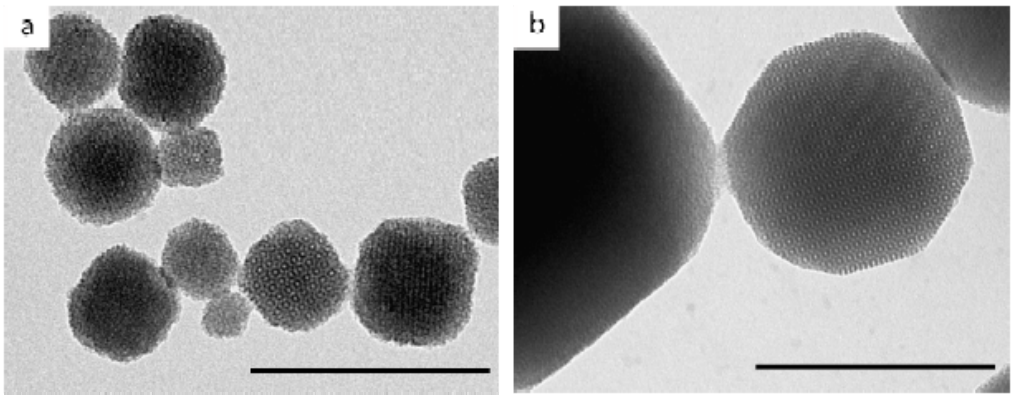

Figure 4.9. TEM images of acid-extracted 54-NH_2-MSNs synthesized using (a) 103.5 mM and (b) 409 mM NH_4OH concentrations. All scale bars are 200 nm.

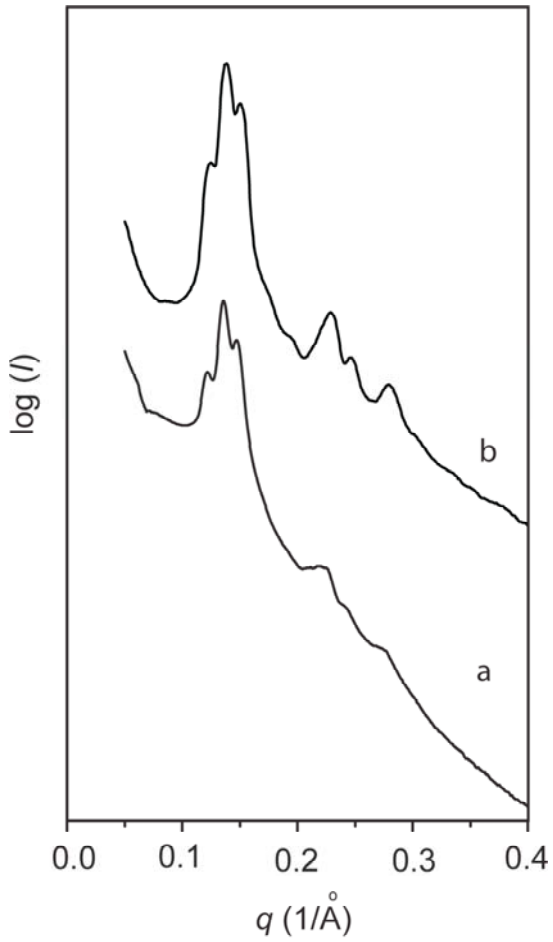

Figure 4.10. SAXS diffractograms of acid-extracted 54-NH_2-MSNs synthesized at (a) 103.5 mM and (b) 409 mM NH_4OH concentrations.

of the shape of NH_2-MSNs. The closer the pH is to pH 7, the faster the condensation rate of silica. Furthermore, the results are similar to what has been reported in acid-catalyzed systems using a single silane precursor.[35] In the preparation of SBA-1, for example, the acidity of the solution with respect to the isoelectric point of silica affects hydrolysis and condensation rates of silica, which consequently changes the shape of the resulting particles without disturbing mesostructure.[32, 34, 35] Effect of pH in the synthesis of cubic $Pm\bar{3}n$ in basic solution has not yet been carefully studied. From our work, at higher pH, the condensation rate of silica is slow. Growth of particles thus should be more thermodynamically controlled, which then yields well-defined NH_2-MSNs with truncated-octahedral shape. On the other hand, at less basicity, growth of particles would be more kinetically controlled as the condensation rate of silica is faster. Consequently, less well-defined NH_2-MSNs exhibiting fewer facets were formed.

SAXS scattering patterns of 54-NH_2-MSNs prepared under different NH_4OH concentrations are shown in Figure 4.10 (a-b). Regardless of catalyst concentration and irrespective of final particle size and shape, SAXS diffractograms of both samples exhibit similar patterns to those of 54-NH_2-MSNs synthesized at the original catalyst content (207.5 mM, Figure 4.2), and can be indexed to a cubic lattice with $Pm\bar{3}n$ symmetry.

4.4 Conclusions

In this study, we reported the synthesis of NH_2-MSNs from different amounts of APTES in the reaction feed. By increasing initial APTES concentrations, mesoporous particle structure altered from hexagonal to cubic $Pm\bar{3}n$ to disordered. Investigation of particle structure at various time points in the synthesis of $Pm\bar{3}n$ cubic 54-NH_2-MSNs revealed a gradual structural transition from disordered

nanoparticle (≈ 5-10 nm) clusters formed during the first couple of minutes to the fully developed cubic lattice occurring after about 50 minutes. Size and shape of highly aminated $Pm\bar{3}n$ MSNs using 54 mol% APTES could be further controlled by means of tuning pH using different NH_4OH concentration. At higher pH, through slow down of silica condensation rates, growth of particle is less kinetically controlled, resulting in the formation of aminated $Pm\bar{3}n$ MSNs with larger size and higher number of well-defined crystal facets as compared to particles prepared at lower pH.

4.5 Acknowledgement

This work was supported by the Cornell Center for Materials Research (CCMR) with funding from a PREM program at Norfolk State University through the National Science Foundation (NSF) grant (DMR-0611430), by the Department of Energy grant DE-FG02-97ER62443 and by the National Institute of Dental and Craniofacial Research (R21DE018335). We thank the Cornell Universiy KAUST Center for Research and Education for financial support. This work was further supported by the U.S. Department of Homeland Security under Cooperative Agreement Number "2009-ST-108-LR0004". The authors thank CCMR for facility support. This work is based upon research conducted at the Cornell High Energy Synchrotron Source (CHESS), which is supported by the NSF and the National Institutes of Health/National Institute of General Medical Sciences under NSF award DMR-0225180. T.S. is grateful for a Thai Government Scholarship under the Ministry of Science and Technology.

4.6 Disclaimer

The views and conclusions contained in this document are those of the authors and should not be interpreted as necessarily representing the official policies, either expressed or implied, of any of the funding agencies.

REFERENCES

1. Tan, W. H.; Wang, K. M.; He, X. X.; Zhao, X. J.; Drake, T.; Wang, L.; Bagwe, R. P., *Medicinal Research Reviews* **2004,** *24* (5), 621-638.

2. Kim, S.; Ohulchanskyy, T. Y.; Pudavar, H. E.; Pandey, R. K.; Prasad, P. N., *Journal of the American Chemical Society* **2007,** *129* (9), 2669-2675.

3. Noginov, M. A.; Zhu, G.; Belgrave, A. M.; Bakker, R.; Shalaev, V. M.; Narimanov, E. E.; Stout, S.; Herz, E.; Suteewong, T.; Wiesner, U., *Nature* **2009,** *460* (7259), 1110-1113.

4. Ow, H.; Larson, D. R.; Srivastava, M.; Baird, B. A.; Webb, W. W.; Wiesner, U., *Nano Letters* **2005,** *5* (1), 113-117.

5. Ying, J. Y.; Mehnert, C. P.; Wong, M. S., *Angewandte Chemie, International Edition* **1999,** *38* (1-2), 56-77.

6. Wan, Y.; Zhao, D. Y., *Chemical Reviews* **2007,** *107* (7), 2821-2860.

7. Yanagisawa, T.; Shimizu, T.; Kuroda, K and Kato, C., *Bulletin of Chemical Society Japan.* **1990,** *63* (4), 988-992.

8. C. T. Kresge, M. E. L., W. J. Roth, J. C. Vartuli and J. S. Beck, *Nature* **1992,** *359*, 710-712.

9. Beck, J. S.; Vartuli, J. C.; Roth, W. J.; Leonowicz, M. E.; Kresge, C. T.; Schmitt, K. D.; Chu, C. T. W.; Olson, D. H.; Sheppard, E. W.; McCullen, S. B.; Higgins, J. B.; Schlenker, J. L., *Journal of the American Chemical Society* **1992,** *114* (27), 10834-10843.

10. Vallet-Regi, M.; Balas, F.; Arcos, D., *Angewandte Chemie, International Edition* **2007,** *46*, 7548-7558.

11. Brohede, U.; Atluri, R.; Garcia-Bennett, A. E.; Stromme, M., *Current Drug Delivery* **2008,** *5* (3), 177-185.

12. Lu, F.; Wu, S. H.; Hung, Y.; Mou, C. Y., *Small* **2009,** *5* (12), 1408-1413.

13. Burns, A. A.; Vider, J.; Ow, H.; Herz, E.; Penate-Medina, O.; Baumgart, M.; Larson, S. M.; Wiesner, U.; Bradbury, M., *Nano Letters* **2009,** *9* (1), 442-448.

14. Vallhov, H.; Gabrielsson, S.; Stromme, M.; Scheynius, A.; Garcia-Bennett, A. E., *Nano Letters* **2007,** *7* (12), 3576-3582.

15. Fan, J.; Lei, J.; Wang, L. M.; Yu, C. Z.; Tu, B.; Zhao, D. Y., *Chemical Communications (Cambridge, United Kingdom)* **2003,** (17), 2140-2141.

16. Fan, J.; Yu, C. Z.; Gao, T.; Lei, J.; Tian, B. Z.; Wang, L. M.; Luo, Q.; Tu, B.; Zhou, W. Z.; Zhao, D. Y., *Angewandte Chemie, International Edition* **2003,** *42* (27), 3146-3150.

17. Huh, S.; Wiench, J. W.; Yoo, J. C.; Pruski, M.; Lin, V. S. Y., *Chemistry of Materials* **2003,** *15* (22), 4247-4256.

18. Sadasivan, S.; Khushalani, D.; Mann, S., *Journal of Materials Chemistry* **2003,** *13* (5), 1023-1029.

19. Burleigh, M. C.; Markowitz, M. A.; Spector, M. S.; Gaber, B. P., *Chemistry of Materials* **2001,** *13* (12), 4760-4766.

20. Burleigh, M. C.; Markowitz, M. A.; Spector, M. S.; Gaber, B. P., *Journal of Physical Chemistry B* **2001,** *105* (41), 9935-9942.

21. Gao, C.; Che, S., *Advanced Functional Materials* **2010,** *20* (17), 1-19.

22. Liu, J.; Shin, Y.; Nie, Z. M.; Chang, J. H.; Wang, L. Q.; Fryxell, G. E.; Samuels, W. D.; Exarhos, G. J., *Journal of Physical Chemistry A* **2000,** *104* (36), 8328-8339.

23. Atluri, R.; Sakamoto, Y.; Garcia-Bennettt, A. E., *Langmuir* **2009,** *25* (5), 3189-3195.

24. Suteewong, T.; Sai, H.; Cohen, R.; Wang, S.; Bradbury, M.; Baird, B.; Gruner, S. M.; Wiesner, U., *Journal of the American Chemical Society.*

25. Toombes, G. E. S.; Mahajan, S.; Weyland, M.; Jain, A.; Du, P.; Kamperman, M.; Gruner, S. M.; Muller, D. A.; Wiesner, U., *Macromolecules* **2008,** *41* (3), 852-859.

26. Tate, M. W.; Eikenberry, E. F.; Barna, S. L.; Wall, M. E.; Lowrance, J. L.; Gruner, S. M., *Journal of Applied Crystallography* **1995,** *28*, 196-205.

27. Brunauer, S.; Deming, L. S.; Deming, W. E.; Teller, E., *Journal of the American Chemical Society* **1940,** *62*, 1723-1732.

28. Barrett, E. P.; Joyner, L. G.; Halenda, P. P., *Journal of the American Chemical Society* **1951,** *73* (1), 373-380.

29. Ravikovitch, P. I.; Neimark, A. V., *Langmuir* **2002,** *18* (5), 1550-1560.

30. Suteewong, T.; Sai, H.; Lee, J.; Bradbury, M.; Hyeon, T.; Gruner, S. M.; Wiesner, U., *Journal of Materials Chemistry 20* (36), 7807-7814.

31. Soler-illia, G. J. D.; Sanchez, C.; Lebeau, B.; Patarin, J., *Chemical Reviews* **2002,** *102* (11), 4093-4138.

32. Che, S. N.; Lim, S. Y.; Kaneda, M.; Yoshitake, H.; Terasaki, O.; Tatsumi, T., *Journal of the American Chemical Society* **2002,** *124* (47), 13962-13963.

33. Che, S.; Sakamoto, Y.; Terasaki, O.; Tatsumi, T., *Chemistry of Materials* **2001,** *13* (7), 2237-2239.

34. Che, S.; Sakamoto, Y.; Terasaki, O.; Tatsumi, T., *Chemistry Letters* **2002,** (2), 214-215.

35. Chao, M. C.; Wang, D. S.; Lin, H. P.; Mou, C. Y., *Journal of Materials Chemistry* **2003,** *13* (12), 2853-2854.

CHAPTER 5

LARGE PORE AMINATED MESOPOROUS SILICA NANOPARTICLES[*]

5.0 Abstract

We report the room-temperature synthesis of large pore mesoporous silica nanoparticles synthesized by means of 1,3,5-trimethylbenzene (TMB) as swelling agent. The effect of TMB concentrations on properties of mesoporous nanoparticles was investigated using the combination of transmission electron microscope (TEM), small-angle x-ray scattering (SAXS) and N_2 sorption measurements. Pore sizes of resulting mesoporous silica increase with increasing TMB concentrations without significantly disturbing packing regularity of pore structure. In contrast to pore size, overall particle sizes decrease. We extend this approach further by combining with co-condensation method to prepare large pore aminated mesoporous silica nanoparticles using tetraethoxysilane (TEOS) and 3-aminopropyl triethoxysilane (APTES). TEM and SAXS analyses show that an increase in APTES in the synthesis feed leads to a structural transformation of aminated mesoporous nanoparticles from hexagonal to cubic-type structures. Organically modified nanoparticles exhibit larger pore sizes than those of non-organically modified materials as confirmed by N_2 sorption measurements and SAXS. ^{29}Si NMR data reveal that large pore aminated mesoporous nanoparticles exhibit low degrees of silica condensation, which likely causes a structural transition in this study.

[*] Prepared for Submission as: Teeraporn Suteewong, Hiroaki Sai, Juho Song, Rachel M. Dorin, Michelle Bradbury, Sol M. Gruner and Ulrich Wiesner. *Large Pore Aminated Mesoporous Silica Nanoparticles.*

5.1 Introduction

Silica-based mesoporous materials prepared from assemblage of structure-directing molecules and silica precursors have attracted the interest of researchers from various fields since their discovery.[1, 2, 3, 4] To date, numerous studies focusing on syntheses, formation mechanisms, structure control, chemical modifications and integration with different matters have been reported either to employ or to improve the functionalities of mesoporous silica.[1, 5, 6, 7]

Mesoporous materials are characterized by their high surface area, large pore volume and tunable pore diameter.[1, 4] One original interest in mesoporous materials was for catalysis and separation.[8] Later, materials have been opted for different purposes, such as anti-reflection, chemical sensing and as drug carriers.[1, 4, 9, 10, 11] Similar to other mesoporous materials, control of pore structure as well as pore diameter of mesoporous silica is important as they strongly affect materials performance. Several structures of ordered mesoporous silica, such as two- (2D) and three-dimensionally (3D) hexagonal and 3D cubic morphologies, have been reported.[1, 4, 8] Each architecture influences the diffusion properties of adsorbed molecules in pore channels differently.[12, 13] Furthermore, the size of possible cargo molecules is determined by the width of the pore entrance. Pore diameter engineering is thus an important issue. It can be tailored by several means, such as tuning the hydrophobic tail length of ionic surfactants, using block copolymers of different molar mass as templates, manipulating synthesis conditions for example pH or reaction time, or using auxiliary organic (co-) solvents.[1, 8, 12, 13] Incorporating organic additives, such as decane, 1,3,5-trimethylbenzene (TMB or mesitylene), 1,3,5-triethylbenzene (TEB) and 1,3,5-triisopropylbenzene (TIPB), is an effective way to enlarge pore size. These organic co-solvents solubilize in the hydrophobic region of surfactant micelles and act as swelling agents, which then yield the expanded pore sizes. Due to their hydrophobic

nature, swelling agents are often used along with hydrothermal treatment or at elevated temperature to enhance the incorporation inside surfactant micelles. However, the resulting materials normally show an inferior order or even disordered structures.[1]

The role of auxiliary organic solvents is not limited to the expansion of pore diameter. They have also been used to study the formation mechanism of several mesoporous material systems. Che *et al.* investigated the epitaxial phase transformation from hexagonal to cubic $Pm\bar{3}n$ symmetry of cationic surfactant-templated mesoporous silica. Three isomers of trimethylbenzene, i.e. 1,2,3-, 1,2,4- and 1,3,5- trimethylbenzene were used to slow down the transition process by stabilizing the hexagonal phase.[14] A similar approach was adopted to study the structural transformations in block copolymer-templated mesoporous material systems. Recently, we reported the base-catalyzed synthesis of aminated mesoporous silica nanoparticles (NH_2-MSNs) with and without TMB.[15] In the absence of TMB, cubic $Pm\bar{3}n$ NH_2-MSNs with truncated octahedral shape were formed. In the presence of TMB, large-pore aminated materials exhibiting quasi-periodic pore structure were obtained. The pore size was about two times larger compared to the TMB-free system. At the same time the addition of TMB caused smaller particle sizes (~100 nm). Hence, TMB plays a more complex role in the synthesis than simply expanding particle pore size. Tunability of particle size of mesoporous silica down to the nano-regime is highly desirable, especially in biology and nanomedicine.[10, 16] Tunable pore sizes will allow a broad size range of therapeutics or molecules of interest to be carried.[13] We are thus interested in developing mesoporous silica with tunable pore and particle sizes as well as various surface functionalities.

Herein, we report the room temperature synthesis of large pore mesoporous silica nanoparticles (MSNs) with MCM-41-type structure in the presence of TMB as a

co-solvent. By simply adding TMB to the surfactant solution before the addition of the silica precursor, the pore size of the resulting materials increases with increasing concentration of TMB as confirmed by small angle x-ray scattering (SAXS) and N_2 sorption measurements. In contrast to the pore diameter, the overall particle size as determined from transmission electron microscopy (TEM) becomes smaller (smaller than 100 nm). This approach is then used to synthesize large pore NH_2-MSNs via co-condensation between TEOS and APTES. While in our previous work on NH_2-MSNs we only reported results for one APTES/TEOS ratio, here large pore NH_2-MSNs are prepared with varying relative amounts of APTES and TMB. Prepared with the same amount of TMB, pore sizes of amine-modified materials are larger than for un-modified, large pore MSNs. A combination of SAXS, TEM, ^{29}Si-NMR and N_2 sorption measurements are used to characterize the resulting large pore NH_2-MSNs.

5.2 Experimental Section

5.2.1 Materials

Hexadecyltrimethylammonium bromide (apprx. 99%), ethyl acetate (EtOAc, ACS grade), tetraethyl orthosilicate (TEOS, ≥99%, GC), 3-aminopropyl triethoxysilane (APTES, > 95%), ammonium hydroxide (NH_4OH, 29%), acetic acid (glacial), hydrochloric acid (36.5-38%), ethanol (absolute, anhydrous) and deionized water (Milli-Q, 18.2 MΩ-cm) were used as obtained without further purification.

5.2.2 Synthesis of Large Pore Mesoporous Silica Nanoparticles (Large Pore MSNs)

Ethyl acetate (EtOAc), ammonium hydroxide (NH_4OH) and 1,3,5-trimethylbenzene (TMB) were sequentially added into an aqueous solution of hexadecyltrimethylammonium bromide (CTAB) (54.8 mM) and stirred for 30 minutes. Tetraethyl orthosilicate (TEOS) was added and stirred for 5 minutes.

Additional water was then added into the reaction before leaving the solution 15 minutes under stirring. The amounts of TMB in the synthesis were varied, corresponding to 0.023, 0.047, 0.070, 0.093, 0.0129, 0.0139 and 0.162 M, respectively. All other chemicals were kept constant for all samples. For example, in the case of reaction containing 0.047 M TMB, the volumetric ratio in milliliters of chemicals used was 5 CTAB (aq):100 H_2O:0.88 EtOAc:0.712 TMB:2.7 NH_4OH:0.5 TEOS and 36.9 mL of additional H_2O. After 20 minutes, the reaction solution was neutralized using hydrochloric acid solution (2 M). The resulting solution was slightly translucent. Every step was performed at room temperature. The sample was cleaned by centrifugation and re-dispersed in ethanol. CTAB was removed by acid extraction using an acetic acid/ethanol mixture (95/5 v/v). Samples were stirred for 30 minutes, before centrifugation to remove CTAB and acetic acid.

5.2.3 Synthesis of Large Pore Aminated Mesoporous Silica Nanoparticles

In general, the preparation and chemical concentrations used were similar to the synthesis protocol of large pore MSNs, except for the addition of APTES. After the addition of EtOAc, NH_4OH and TMB into the CTAB aqueous solution, the solution was stirred for 30 minutes before adding a mixture of silica precursors (TEOS and APTES). For three concentrations of TMB chosen in this study, i.e., 0.047, 0.093 and 0.129 M, APTES loadings were varied from 10-55 mol%. For example, the volumetric ratio in milliliters of chemicals used was 5 CTAB (aq):100 H_2O:0.88 EtOAc:0.712 TMB:2.7 NH_4OH:0.225 TEOS: 0.275 APTES and 36.9 mL of additional H_2O for 0.047 M TMB and 54 mol% APTES loading. The subsequent steps were followed in the same way to what has been described in the previous section, except that the reaction solution was left overnight under stirring after the addition of water.

Throughout this paper, we will refer to these materials as large pore NH_2-MSNs-X, where X is the mol% of APTES in the synthesis feed.

5.2.4 Particle Characterization

Transmission electron microscopy (TEM) images were obtained with a FEI Tecnai T12 Spirit microscope operated at an acceleration voltage of 120kV. Average particle sizes were obtained by averaging over approximately 100 particles. Small-angle x-ray scattering (SAXS) patterns of large pore MSNs and large pore NH_2-MSNs were obtained (i) on a home-built beamline as previously described[17, 18] with a sample-to-detector distance of 25 cm and (ii) at the G1 beamline of the Cornell High Energy Synchrotron Source (CHESS) with a beam energy of 9.5 keV and with a sample to detector distance of 35 cm.[17] All samples were in dry form, with CTAB removed by acid extraction (vide supra). Nitrogen physisorption isotherms of dried samples were obtained with a Micromeritics ASAP2020 physisorption instrument. The particles exhibited nitrogen sorption isotherms of type IV according to BDDT classification.[19, 20] Surface areas were determined according to the Brunnauer-Emmett-Teller (BET) method.[20] The BET surface area analysis was performed in the range between 0.042 and 0.095. Calculation of the pore size distributions from the adsorption branches of the isotherms was performed according to the Barrett-Joyner-Halenda[21] (BJH) method as well as a geometrical model as described in previous papers[15, 22]. Solid-state ^{29}Si NMR experiments were performed on a Bruker Avance DSX NMR spectrometer with a 9.4T magnet (400 MHz proton Larmor frequency, 79.52 MHz ^{29}Si Larmor frequency) using a probe head for rotors of 4 mm diameter. The chemical shift scale was referenced against the ^{29}Si NMR resonance of Kaolin at -91.34 ppm.[23]

5.3 Results and Discussion

5.3.1 Effect of Varying TMB Concentration on Mesoporous Silica

Pore structure and pore size of bulk and nano-sized mesoporous materials are known to govern the materials performance.[1, 8, 9] Significant efforts are devoted to control pore size while minimizing the loss of ordered pore structure, which is a challenging aspect especially for mesoporous nanoparticles.[24] In the present work, we report a room temperature synthesis of pore-expanded MSNs with the assistance of TMB, i.e., a pore expander. This method is facile, can be performed under mild conditions, and proceeds on a short time scale (20 minutes). Figure 5.1 (b-h) shows TEM images of large pore MSNs made from different amounts of TMB in the reaction solution (0.023-0.162 M). For comparison a TEM image of non-modified MSNs is included (Figure 5.1a) as a control sample. All samples in Figure 5.1 (a-h) exhibit an ordered pore arrangement; even though the regularity of mesopores seems to slightly decrease when high concentrations of TMB, i.e. 0.129-0.162 M (Figure 5.1f-h), were used. Besides affecting pore size and structural regularity, from TEM analysis the overall particle size of mesoporous silica significantly decreases from about 140 nm in the absence of TMB to about 60 nm upon the addition of the largest amount, i.e. 0.162 M, of TMB (see Table 5.1).

The structure of pore-expanded mesoporous silica was further characterized by SAXS measurements. SAXS scattering patterns shown in Figure 5.2 were taken from dried samples after removal of surfactant templates by acid extraction as described in the Experimental Section. Here, q denotes the scattering vector and is defined as $q = (4\pi\sin\theta)/\lambda$ with a scattering angle 2θ and the x-ray wavelength, $\lambda = 1.54$ Å. SAXS patterns of samples prepared with 0.093-0.162 M TMB are less well resolved than those prepared with lower TMB concentrations. However, scattering patterns of all resulting materials show 4 peaks at q values between 0.136 to 0.384 $Å^{-1}$, which can be

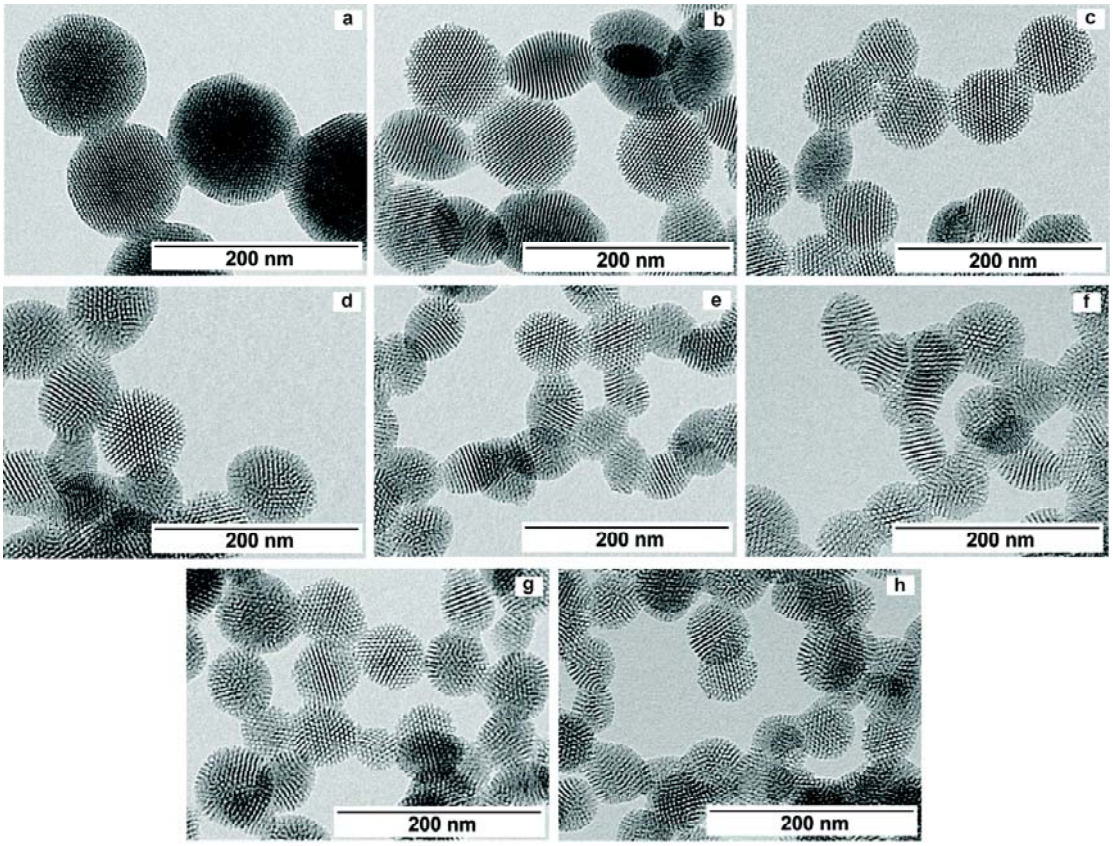

Figure 5.1. TEM images of acid-extracted large pore MSNs made from (a) 0, (b) 0.023, (c) 0.047, (d) 0.070, (e) 0.093, (f) 0.129, (g) 0.139 and (h) 0.162 M TMB in the reaction solution.

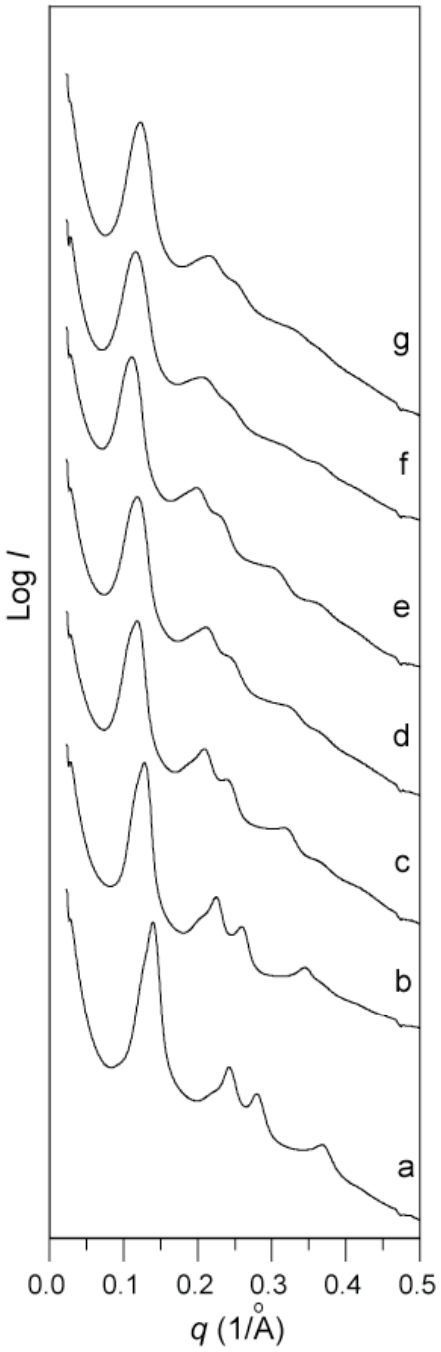

Figure 5.2. SAXS diffractograms of acid-extracted large pore MSNs made from (a) 0.023, (b) 0.047, (c) 0.070, (d) 0.093, (e) 0.129, (f) 0.139 and (g) 0.162 M TMB.

Table 5.1. BET surface area, BJH pore size, unit cell size (a), spacing (d_{100}) and particle size from TEM analysis of acid-extracted control samples and large pore MSNs made from different TMB concentrations.

Samples	[TMB]	BET surface area (m^2/g)	BJH pore size (nm)	a_0 (Å)	d_{100} (Å)	Size from TEM analysis (nm)
1	0	1122.7	2.7	44.6	38.6	140 ± 15
2	0.023	1100.7	3.2	51.9	44.9	93 ± 13
3	0.047	1193.5	3.8	56.4	48.8	75 ± 11
4	0.070	1131.0	4.2	61.3	53.0	94 ± 10
5	0.093	1152.3	4.1	61.0	52.8	74 ± 8
6	0.129	1217.0	4.5	65.2	56.4	69 ± 7
7	0.139	1168.2	4.1	62.3	54.0	64 ± 7
8	0.162	1507.9	3.7	59.2	51.3	62 ± 5

indexed as 10, 11, 20 and 21 reflections of a hexagonal lattice. These SAXS data are consistent with a hexagonal, MCM-41 type material. Figure 5.3 graphically shows that d_{100} spacings significantly increase with TMB concentrations, a trend that is reversed for the two highest concentrations of TMB.

BET surface area and BJH pore sizes of the resulting materials after CTAB removal are presented in Table 5.1 and the Appendix C. All samples possess high surface areas above 1000 m^2/g. The highest BET surface area was obtained from the sample prepared with 0.162 M TMB. BJH pore sizes increase with increasing concentrations of TMB (from 0.023 to 0.129 mM), and slightly decrease when the TMB concentration is larger than 0.129 mM, as plotted in Figure 5.3.[25, 26] These results suggest that, within a certain range, the amount of TMB residing in the surfactant micelle cores is proportional to the loading concentration, resulting in the expansion of the mesopores. Excess TMB can form either droplets or locate near surfactant head groups, which can hinder diffusion/dissolution of other molecules.[27] It is important to emphasize that all syntheses were performed at ambient temperature, for which the dissolution of non-polar TMB in aqueous phase should be low. After the addition of TMB, the reaction solution indeed became translucent/less transparent, which is consistent with phase separation. This was observed for every preparation protocol, suggesting that only a partial amount of TMB went into the surfactant micelles.

5.3.2 Effect of Varying APTES Concentration on Large Pore Aminated Mesoporous Silica

From the previous section, prepared in the presence of 0.047 M TMB mesoporous silica shows a significant pore size increase (~1.1 nm, see Table 5.1) compared to the synthesis without TMB, as well as good pore structure regularity.

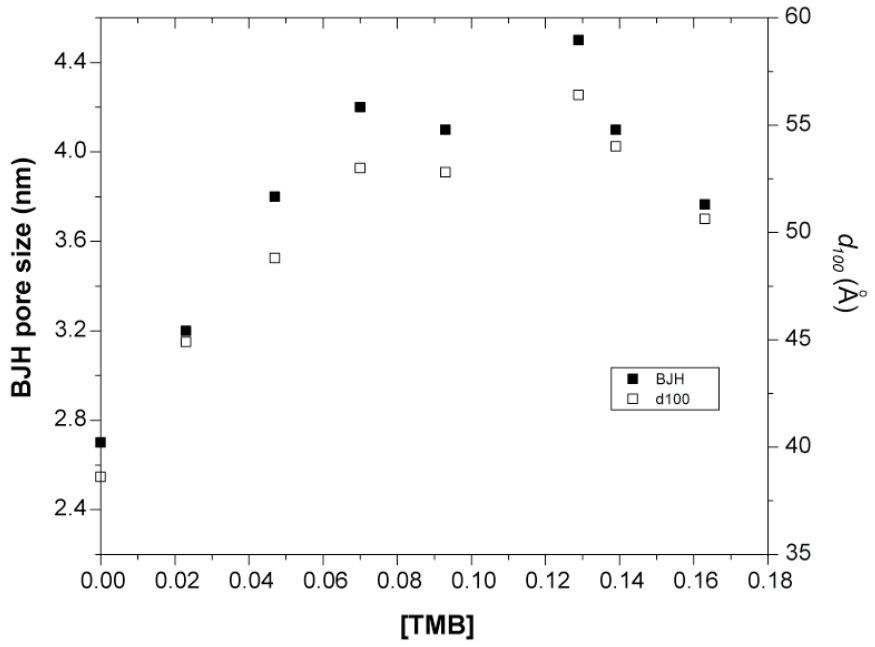

Figure 5.3. BJH pore sizes and d_{100} spacing of acid-extracted large pore MSNs made from different concentrations of TMB.

This concentration was chosen in subsequent experiments to also enlarge the pore size of aminated MSNs (NH_2-MSNs). As we demonstrated recently, a high APTES concentration added to TEOS as silica precursor (54 mol%) in the synthesis feed of a co-condensation route can cause a structural transition from hexagonal to cubic $Pm\bar{3}n$ symmetry in the resulting nanoparticles.[15, 28] The combination of TMB (0.047 M) and a high APTES concentration in the synthesis feed (54 mol%) yielded large-pore aminated materials exhibiting a quasi-periodic pore structure. TEM images showed similar structural features as images of larger particles with $Pm\bar{3}n$ symmetry.[15] In the present study, we now explore the combination effect of the two additives, i.e., TMB and APTES, on the formation of large pore NH_2-MSNs by controlling the amounts of both, TMB and APTES, in the particle synthesis feed.

TEM images of large pore NH_2-MSNs prepared in the presence of 0.047 M TMB and varying amounts of APTES (10-54 mol%) in addition to TEOS are presented in Figure 5.4 (a-d). As the amount of APTES in the reaction feed increases, the structure of the resulting nanoparticles changes from what looks like hexagonal (Figure 5.4a, 10 mol%) to a different structure at higher APTES amounts (Figure 5.4b-d, 24-54 mol%). In Figure 5.4a, two different orientations of cylindrical pores, i.e., perpendicular and parallel to the imaging plane, are observed in the same particle. For most particles, cylinders parallel to the imaging plane are located at particle edges, while the center exhibits what looks like hexagonal arrays of pores. TEM images of samples containing moderate amounts of APTES in the synthesis feed (24 and 39 mol%; Figure 5.4b-c) clearly show particles with 4-fold symmetry projections. Once 54 mol% APTES is fed in the synthesis, the resulting nanoparticles exhibit a quasi-periodic pore arrangement. For example, in Figure 5.4c a mesoporous particle with distorted 4-fold symmetry is observed. We speculate that the distortion is due to the small particle size obtained under these synthesis conditions.

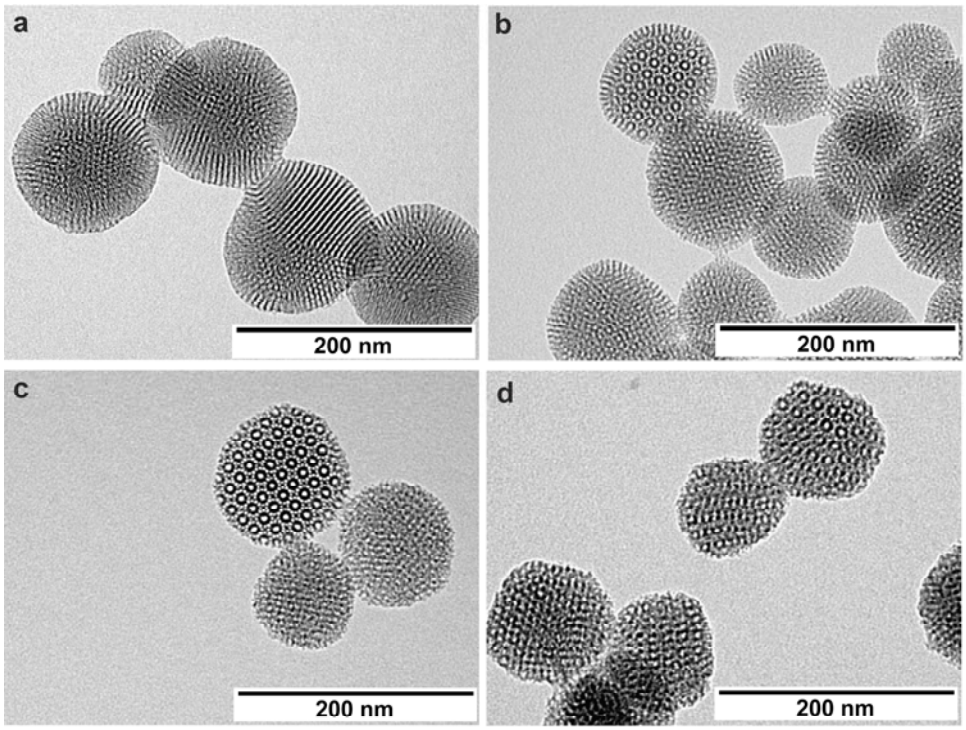

Figure 5.4. TEM images of acid-extracted large pore NH_2-MSNs made from 0.047 M TMB with (a) 10, (b) 24, (c) 39 and (d) 54 mol% APTES in the reaction feed.

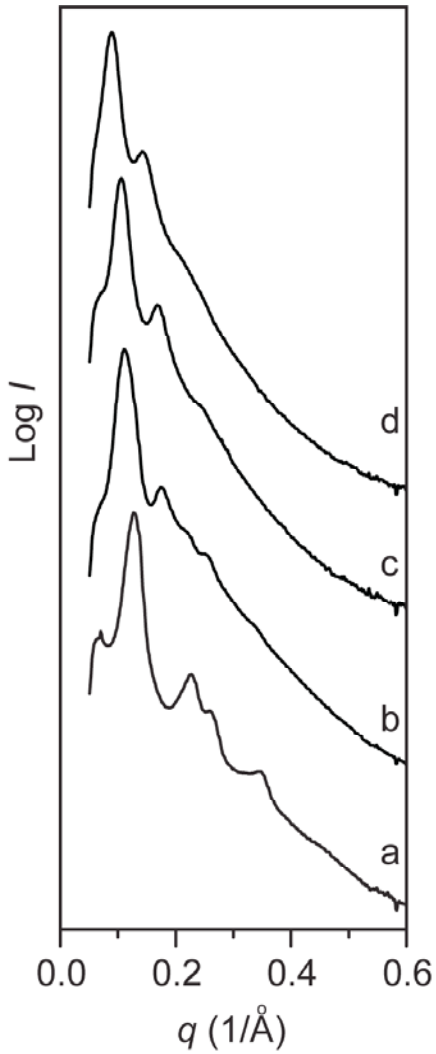

Figure 5.5. SAXS diffractograms of acid-extracted large pore NH_2-MSNs made from 0.047 M TMB with (a) 10, (b) 24, (c) 39 and (d) 54 mol% APTES in the reaction feed.

To further investigate the structure of large pore aminated materials, SAXS measurements were performed on the acid-extracted aminated samples in dried form, see Experimental Section. Results of those experiments are shown in Figure 5.5. TheSAXS diffractogram of large pore NH_2-MSNs-10% possesses 4 peaks, which can be indexed as 100, 110, 200 and 220 reflections of a hexagonal lattice. SAXS spectra of large pore NH_2-MSNs synthesized from 24, 39% and 54% APTES in the reaction feed show less and less well-resolved peaks. None of them is consistent with a hexagonal lattice. TEM and SAXS analyses thus suggest a structural transition upon variation of APTES amount. Except for NH_2-MSNs-10%, however, from SAXS alone it is difficult to assign a lattice to the structure of large pore aminated materials prepared with higher amine in the synthesis feed. Several TEM projections of a cubic $Pm\bar{3}n$ lattice, such as [110], [111] and [210], are observed for sample NH_2-MSNs-24%, as presented in Figure 5.6 (a-d). Some particles show hexagonal structure. This case may be the intermediate in the structural transformation from hexagonal to cubic-type structures with increasing amounts of APTES. TEM images of sample NH_2-MSNs-39% (Figure 5.7) indicate the presence of particles possessing characteristics of a cubic phase such as pore structure projections along (a) [210], (b) [111] and (c) [210] and [100] directions. Figure 5.7d shows a high magnification image along the [100] direction, in which small windows connecting larger pore cavities are clearly seen. Similar to NH_2-MSNs-54% this data suggests the formation of a cubic phase for NH_2-MSNs-39%, As we will discuss below, the relatively small particle size < 100 nm compared to the pore size, as well as the irregular shape are likely the reasons for the diffuse and less well-resolved scattering patterns.

Solid-state ^{29}Si MAS NMR was used to qualitatively determine the degree of silica condensation and the amount of APTES incorporated in large pore NH_2-MSN matrices in the presence of 0.047 M TMB. ^{29}Si MAS NMR spectra of as-synthesized

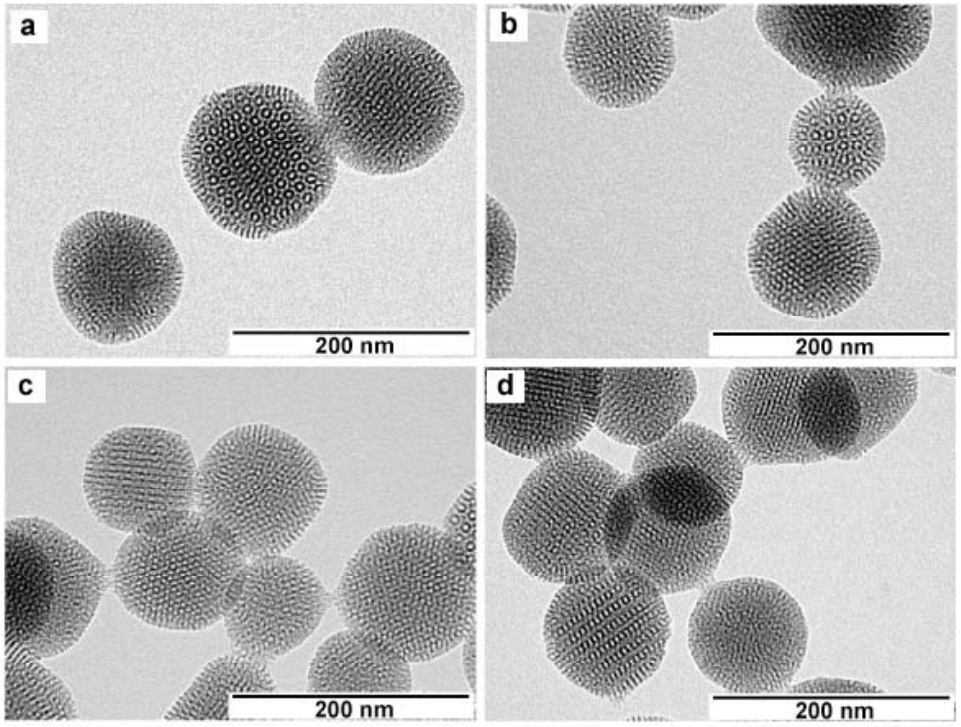

Figure 5.6. TEM images of acid-extracted large pore NH_2-MSNs made from 0.047 M TMB with 24 mol% APTES in the reaction feed.

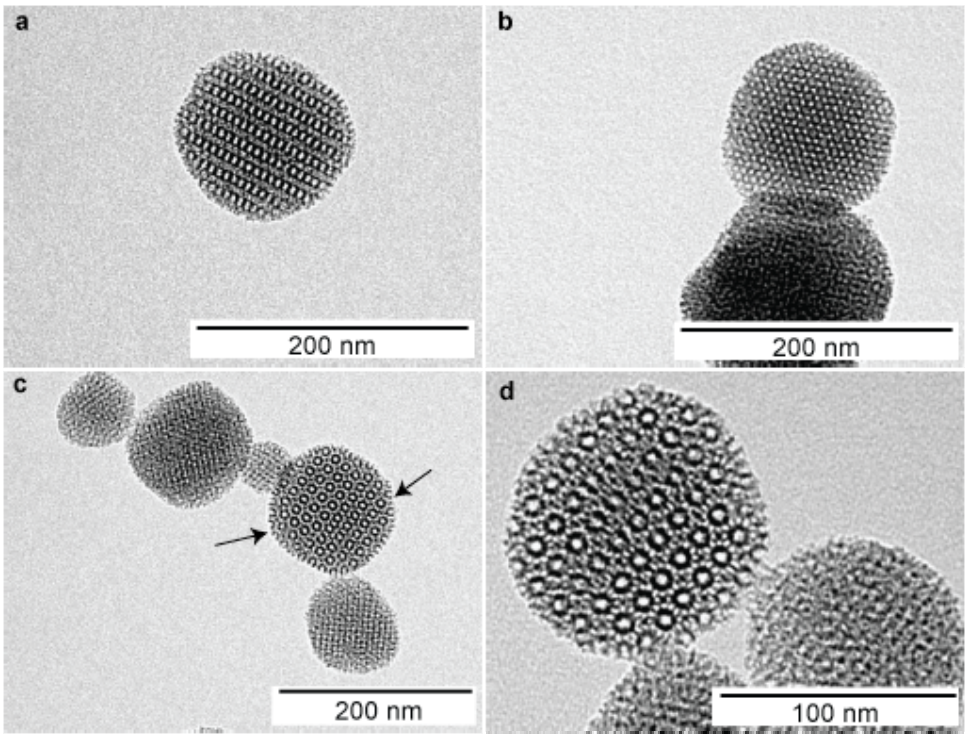

Figure 5.7. TEM images of acid-extracted large pore NH_2-MSNs made from 0.047 M TMB with 39 mol% APTES in the reaction feed.

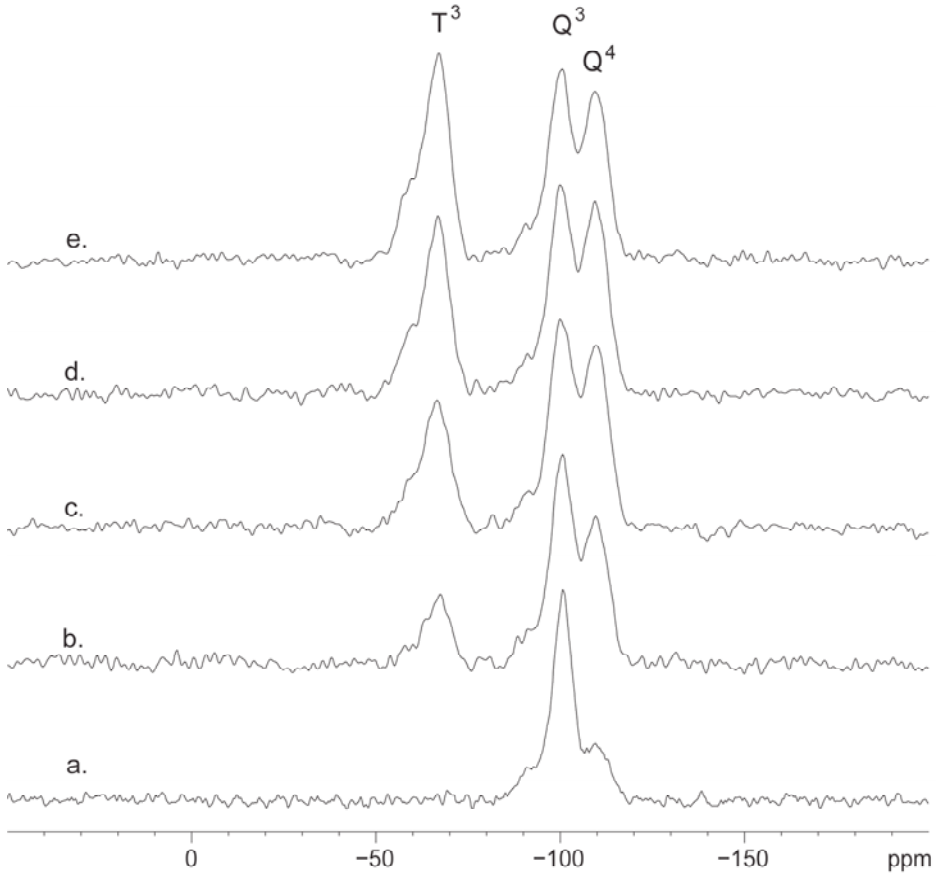

Figure 5.8. ^{29}Si-NMR spectra of as-synthesized large pore NH_2-MSNs made from (b) 10, (c) 25, (d) 40 and (e) 55 mol % APTES in the reaction feed. ^{29}Si-NMR spectrum of (a) as-synthesized large-pored MSNs is shown for comparison. All sample were prepared in the presence of 0.047 M TMB.

large pore NH_2-MSNs are compared to large pore MSNs, i.e. mesoporous silica nanoparticles obtained in the absence of APTES, in Figure 5.8. All spectra of as-synthesized materials show 2 main peaks corresponding to Q^3 (-100 to -101 ppm) and Q^4 (-109 to -111 ppm) groups, respectively. The ^{29}Si NMR spectrum of material synthesized in the absence of APTES shows a significantly higher Q^3 than Q^4 peak, suggesting that condensation of the silica matrix is incomplete. While the Q^3 peak remains the dominant one of the two also in the spectra of all amine-modified materials, the intensity of the Q^4 peak substantially increases. Moreover, an additional peak appears, which can be indexed as T^3 (-66 to -67 ppm). Its presence confirms co-condensation of APTES into the particle matrix. The intensity of the T^3 peak steadily increases upon increase in APTES in the synthesis feed. This observation confirms that the amount of APTES incorporated into the particles is proportional to its concentration in the synthesis feed. The high intensity of Q^3 peaks found in all samples may be the result of the presence of TMB. On the other hand, the amino moieties in APTES clearly act as catalyst promoting silica condensation of TEOS as evidenced by the increased Q^4 intensity in all APTES-modified materials (compare Figure 5.8b-d with 5.8a).

BET surface area and BJH pore size of acid-extracted large pore NH_2-MSNs are reported in Table 5.2. The surface area of these aminated mesoporous nanomaterials is generally lower than that of the non-aminated sample (compare with Table 5.1; 0.047 M TMB). It is still high, however (>700 m^2/g), and decreases with increasing organosilane loading. Plots of N_2 sorption isotherms in Figure C.3 exhibit H2-type hysteresis, suggesting the formation of cage-type mesopores with narrow windows connecting the adjacent pores.[13, 29] In contrast to surface area, BJH pore size increases upon the addition of increasing amounts of APTES and all values are larger than that of the non-aminated reference sample prepared with the same concentration

Table 5.2. BET surface area, BJH pore size, unit cell size (a), spacing (d_{100}), spherical cavity diameter (D_{me}) and particle size from TEM analysis of acid-extracted large pore NH_2-MSNs made from different TMB concentrations.

APTES loading (mol%)	[TMB]	BET surface area (m^2/g)	BJH pore size (nm)	d [a] (Å)	a [b] (Å)	D_{me} [c] (nm)	Particle size [d] (nm)
10	0.047	1000.7	4.0	49.4	57.1	n/a	106 ± 14
24	0.047	882.2	4.4	56.6	126.5 [e]	6.8	105 ± 14
39	0.047	840.7	4.7	59.2	132.5 [e]	7.3	112 ± 18
54	0.047	780.6	5.3	70.0	156.5 [e]	9.6	95 ± 14
10	0.093	934.2	3.6	59.6	68.8	n/a	73 ± 7
29	0.093	868.2	4.4	67.8	151.6 [e]	8.1	79 ± 10
54	0.093	754.1	4.8	75.4	168.5 [e]	9.1	99 ± 12
10	0.129	950.9	4.0	60.8	70.2	n/a	72 ± 7
29	0.129	891.5	4.8	70.0	156.6 [e]	8.5	87 ± 11
54	0.129	747.5	5.2	77.3	172.9 [e]	9.4	100 ± 13

[a] Spacing calculated from the first strongest intensity peak.
[b] Unit cell calculated from the first strongest intensity peak of hexagonal symmetry and [e] cubic (assumed 210 reflection).
[c] Estimated spherical cavity diameter calculated from the geometrical model.
[d] Particle size distribution from TEM analysis.

of TMB (3.8 nm, see Table 5.1; 0.047 M TMB). In order to more appropriately determine pore or cavity size (D_{me}) of large pore NH_2-MSNs (24-54 mol%) samples for which TEM data suggest cubic-like structure, values were calculated using a geometrical model published by Ravikovitch and Neimark.[22] Results of these calculations are presented in Table 5.2. The largest spherical cavity diameter from this model of almost 10 nm is obtained when 55 mol% APTES was added in the synthesis feed.

In previous work, we demonstrated the synthesis of NH_2-MSNs prepared in the absence of TMB with different mol% APTES in the synthesis feed.[15, 30] A silica mesostructure with cubic $Pm\bar{3}n$ symmetry was observed at 54 and 64 mol% of APTES in the synthesis feed. In the present work, the transformation from hexagonal to cubic symmetry occurs at much lower APTES in the feed, i.e., at 24 mol%. Surface curvature of surfactant micelles plays a role in determination of pore architecture.[1, 7, 13] From our study, TMB alone swells and enlarges the surfactant micelles without changing particle pore symmetry. However, if it is present together with APTES molecules, the structural transition is facilitated. It is likely that TMB enables the formation of larger spherical micelles, and leads to the formation of cubic-type symmetry at low APTES loading. The formation of the cubic morphology is thus more favorable than in the system containing APTES alone. As a result the addition of TMB broadens the synthesis window for APTES that yields aminated mesoporous silica nanoparticles with cubic-like symmetry.

In order to broaden our study to other concentration ranges, two higher concentrations of TMB, i.e. 0.093 and 0.129 M, were chosen to prepare large pore aminated MSNs with APTES loadings of 10, 29 and 54 mol% in the reaction feed, respectively. TEM images of the resulting large pore aminated MSNs are shown in Figure 5.9 ((a-c) for 0.093 and (d-f) for 0.129 M TMB). For 0.093 M TMB and 10

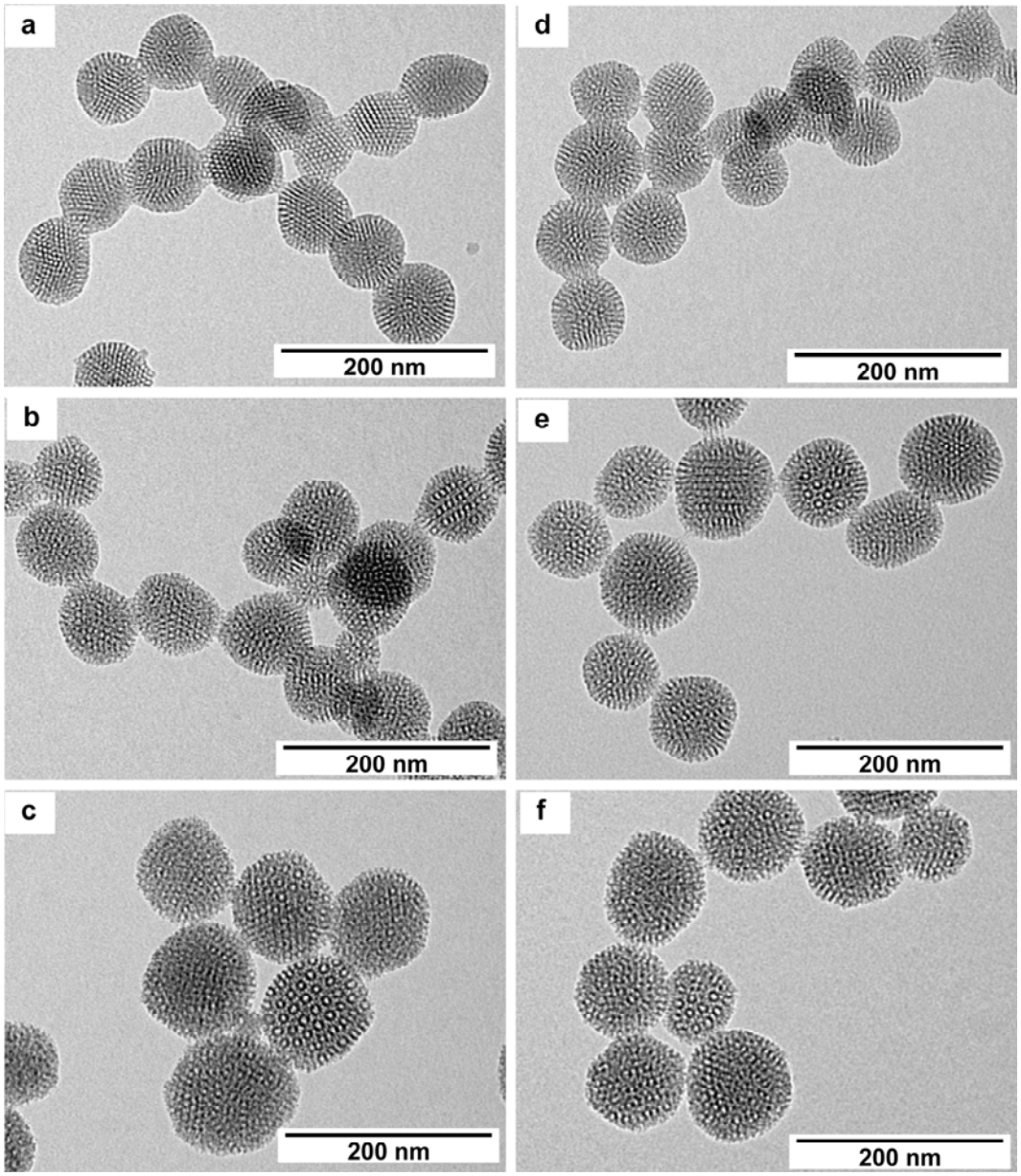

Figure 5.9. TEM images of acid-extracted large pore NH_2-MSNs made from (a-c) 0.093 and (d-f) 0.129 M TMB with different APTES amount (mol%) in the reaction feed; Left column: TMB concentration was 0.093 and mol% APTES were (a) 10, (b) 29 and (c) 54 mol%, respectively. Right column: TMB concentration was 0.129 and mol% APTES were (d) 10, (e) 29 and (f) 54 mol%, respectively.

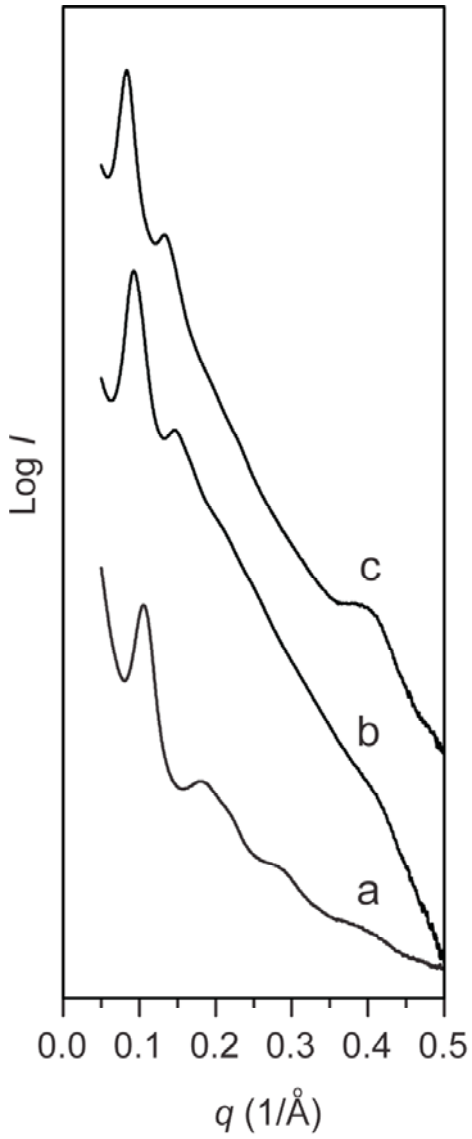

Figure 5.10. SAXS diffractograms of acid-extracted large pore NH_2-MSNs made from 0.093 M TMB with (a) 10, (b) 29 and (c) 54 mol% APTES in the reaction feed

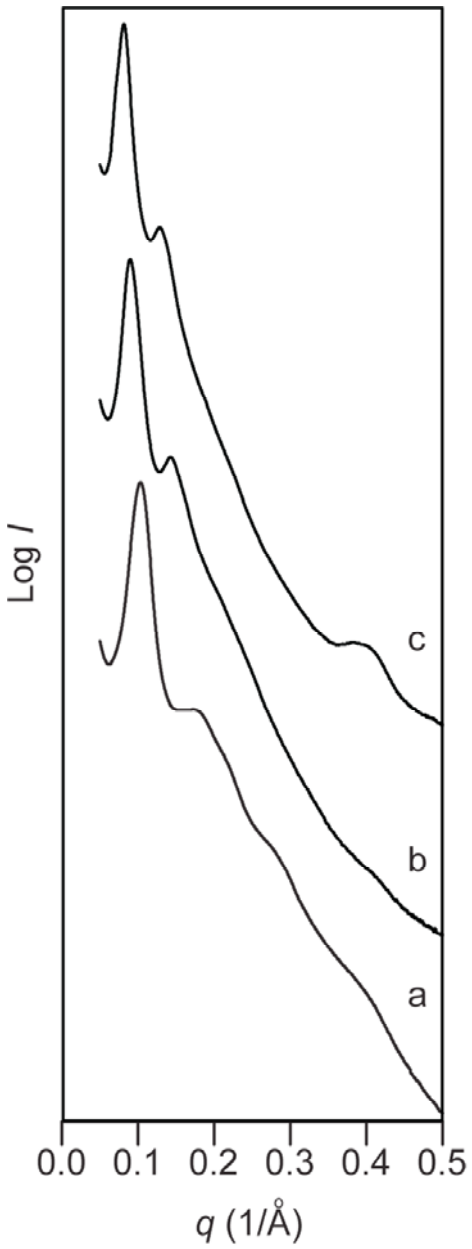

Figure 5.11. SAXS diffractograms of acid-extracted large pore NH_2-MSNs made from 0.129 M TMB with (a) 10, (b) 29 and (c) 54 mol% APTES in the reaction feed.

mol% APTES in the feed, Figure 5.9a reveals sub-100 nm silica nanoparticles with hexagonal pore structure. Upon increase of aminosilane to 29 and 54 mol% in the synthesis feed, some mesoporous particles clearly show 4-fold symmetry projections (Figure 5.9b,c). Similar to NH_2-MSNs made from 0.047 M TMB, BET surface area of samples monotonically decreases with increasing APTES loading, while pore size as determined from BJH (and the geometrical model for 29 and 54 mol% APTES) increases (see Table 5.2). N_2 sorption isotherms of this series are presented in Figure C.5. Sorption data of mesoporous materials prepared with 29 and 54 mol% APTES loading (Figure C.5b and c) exhibit Type IV isotherms with H2 type-loops, as observed for lower TMB concentration (compare to Figure C.3). SAXS measurements were performed on these materials to corroborate the structural information obtained from TEM analysis (Figure 5.10 a-c). At the lowest APTES loading (10 mol%), the SAXS pattern shows four peaks, which can be indexed as 100, 110, 200 and 210 reflections of a hexagonal lattice. Similar to what was described earlier, SAXS diffractograms of materials at higher APTES loading display less well-resolved peaks.

The series of large pore aminated MSNs prepared with 0.129 M TMB exhibits similar morphological trends as the series from 0.093 M TMB, as revealed by TEM and SAXS diffractograms shown in Figure 5.9 d-f and Figure 5.11, respectively. The SAXS pattern of the sample from 10 mol% APTES shows less well-pronounced peaks as the corresponding one from the lower TMB concentration, however, suggesting that higher concentrations of TMB disturb ordered pore formation. BET surface area and BJH pore size for this series are also reported in Table 5.2. Pore sizes of these materials (0.129 M TMB) as estimated from BJH and the geometrical model are slightly larger than those prepared at the same APTS loading but lower TMB concentration.

5.4 Conclusions

In this study, we reported the preparation of large pore mesoporous silica nanoparticles at ambient temperature by means of TMB as a co-solvent. This swelling agent not only expands particle pore size, but also decreases overall particle size, while retaining an ordered pore structure. The combination of TMB and APTES in the synthesis feed led to the formation of large pore NH_2-MSNs. Pore sizes of resulting NH_2-MSNs are larger than those of non-organically modified materials made from the same TMB content. Moreover, at given concentration of TMB, increasing APTES in the synthesis feed resulted in structural transformation from hexagonal to cubic-like symmetries. From this study, TMB is a powerful additive as it can simultaneously be used to fine tune, particle size, mesopore size, as well as the pore structure.

5.5 Acknowledgement

This work was supported by the Cornell Center for Materials Research (CCMR) with funding from a PREM program at Norfolk State University through the National Science Foundation (NSF) grant (DMR-0611430), by the Department of Energy grant DE-FG02-97ER62443 and by the National Institute of Dental and Craniofacial Research (R21DE018335). We thank the Cornell University KAUST Center for Research and Education for financial support. This work was further supported by the U.S. Department of Homeland Security under Cooperative Agreement Number “2009-ST-108-LR0004”. The authors thank CCMR for facility support. This work is based upon research conducted at the Cornell High Energy Synchrotron Source (CHESS), which is supported by the NSF and the National Institutes of Health/National Institute of General Medical Sciences under NSF award DMR-0225180. T.S. is grateful for a Thai Government Scholarship under the Ministry of Science and Technology.

5.6 Disclaimer

The views and conclusions contained in this document are those of the authors and should not be interpreted as necessarily representing the official policies, either expressed or implied, of any of the funding agencies.

REFERENCES

1. Wan, Y.; Zhao, D. Y., *Chemical Reviews* **2007,** *107* (7), 2821-2860.

2. Kresge, C. T.; Leonowicz, M. E.; Roth, W. J.; Vartuli, J. C.; Beck, J. S., *Nature* **1992,** *359* (6397), 710-712.

3. Yanagisawa, T.; Shimizu, T.; Kuroda, K.; Kato, C., *Bulletin of the Chemical Society of Japan* **1990,** *63* (4), 988-992.

4. Ying, J. Y.; Mehnert, C. P.; Wong, M. S., *Angewandte Chemie, International Edition* **1999,** *38* (1-2), 56-77.

5. Sadasivan, S.; Khushalani, D.; Mann, S., *Journal of Materials Chemistry* **2003,** *13* (5), 1023-1029.

6. Kim, J.; Lee, J. E.; Lee, J.; Yu, J. H.; Kim, B. C.; An, K.; Hwang, Y.; Shin, C. H.; Park, J. G.; Hyeon, T., *Journal of the American Chemical Society* **2006,** *128* (3), 688-689.

7. Huh, S.; Wiench, J. W.; Yoo, J. C.; Pruski, M.; Lin, V. S. Y., *Chemistry of Materials* **2003,** *15* (22), 4247-4256.

8. Beck, J. S.; Vartuli, J. C.; Roth, W. J.; Leonowicz, M. E.; Kresge, C. T.; Schmitt, K. D.; Chu, C. T. W.; Olson, D. H.; Sheppard, E. W.; McCullen, S. B.; Higgins, J. B.; Schlenker, J. L., *Journal of the American Chemical Society* **1992,** *114* (27), 10834-10843.

9. Vallet-Regi, M.; Balas, F.; Arcos, D., *Angewandte Chemie, International Edition* **2007,** *46*, 7548-7558.

10. Vallhov, H.; Gabrielsson, S.; Stromme, M.; Scheynius, A.; Garcia-Bennett, A. E., *Nano Letters* **2007,** *7* (12), 3576-3582.

11. Hoshikawa, Y.; Yabe, H.; Nomura, A.; Yamaki, T.; Shimojima, A.; Okubo, T., *Chemistry of Materials* **2010,** *22* (1), 12-14.

12. Brohede, U.; Atluri, R.; Garcia-Bennett, A. E.; Stromme, M., *Current Drug Delivery* **2008,** *5* (3), 177-185.

13. Fan, J.; Yu, C. Z.; Gao, T.; Lei, J.; Tian, B. Z.; Wang, L. M.; Luo, Q.; Tu, B.; Zhou, W. Z.; Zhao, D. Y., *Angewandte Chemie, International Edition* **2003,** *42* (27), 3146-3150.

14. Che, S. N.; Kamiya, S.; Terasaki, O.; Tatsumi, T., *Journal of the American Chemical Society* **2001,** *123* (48), 12089-12090.

15. Suteewong, T.; Sai, H.; Cohen, R.; Wang, S.; Bradbury, M.; Baird, B.; Gruner, S. M.; Wiesner, U., *Journal of the American Chemical Society* **2010**.

16. Burns, A. A.; Vider, J.; Ow, H.; Herz, E.; Penate-Medina, O.; Baumgart, M.; Larson, S. M.; Wiesner, U.; Bradbury, M., *Nano Letters* **2009,** *9* (1), 442-448.

17. Tate, M. W.; Eikenberry, E. F.; Barna, S. L.; Wall, M. E.; Lowrance, J. L.; Gruner, S. M., *Journal of Applied Crystallography* **1995,** *28*, 196-205.

18. Toombes, G. E. S.; Mahajan, S.; Weyland, M.; Jain, A.; Du, P.; Kamperman, M.; Gruner, S. M.; Muller, D. A.; Wiesner, U., *Macromolecules* **2008,** *41* (3), 852-859.

19. Brunauer, S.; Emmett, P. H.; Teller, E., *Journal of the American Chemical Society* **1938,** *60*, 309-319.

20. Brunauer, S.; Deming, L. S.; Deming, W. E.; Teller, E., *Journal of the American Chemical Society* **1940,** *62*, 1723-1732.

21. Barrett, E. P.; Joyner, L. G.; Halenda, P. P., *Journal of the American Chemical Society* **1951,** *73* (1), 373-380.

22. Ravikovitch, P. I.; Neimark, A. V., *Langmuir* **2002,** *18* (5), 1550-1560.

23. Massiot, D.; Fayon, F.; Capron, M.; King, I.; Le Calve, S.; Alonso, B.; Durand, J. O.; Bujoli, B.; Gan, Z. H.; Hoatson, G., *Magnetic Resonance in Chemistry* **2002,** *40* (1), 70-76.

24. Mizutani, M.; Yamada, Y.; Nakamura, T.; Yano, K., *Chemistry of Materials* **2008,** *20* (14), 4777-4782.

25. Jana, S. K.; Nishida, R.; Shindo, K.; Kugita, T.; Namba, S., *Microporous and Mesoporous Materials* **2004,** *68* (1-3), 133-142.

26. Huo, Q. S.; Margolese, D. I.; Ciesla, U.; Demuth, D. G.; Feng, P. Y.; Gier, T. E.; Sieger, P.; Firouzi, A.; Chmelka, B. F.; Schuth, F.; Stucky, G. D., *Chemistry of Materials* **1994,** *6* (8), 1176-1191.

27. Blin, J. L.; Su, B. L., *Langmuir* **2002,** *18* (13), 5303-5308.

28. Atluri, R.; Sakamoto, Y.; Garcia-Bennettt, A. E., *Langmuir* **2009,** *25* (5), 3189-3195.

29. Fukuoka, A.; Kikkawa, I.; Sasaki, Y.; Shimojima, A.; Okubo, T., *Langmuir* **2009,** *25* (18), 10992-10997.

30. Suteewong, T.; Sai, H.; Bradbury, M.; Gruner, S. M.; Wiesner, U., *in preparation.*

CHAPTER 6

CONCLUSIONS

In mesoporous silica nanomaterials the nature of the pore system as well as the size and shape of the pores are important characteristics for materials performance. Pore systems with short and unhindered paths are beneficial for applications that are limited by intra-particle diffusion processes, such as catalysis, separation, guest-molecule encapsulation, and internal-surface modification. To this end extensive work has been devoted to control the morphology of mesoporous silica and organosilicates and to develop tailored nano-sized mesoporous materials. Most research approaches are empirical and based on changes in the synthesis conditions relative to previous work, including changes in the silica sources, the nature of the structure directing surfactants, co-surfactants, solvents and co-solvents, additives, as well as the pH and overall composition of the synthesis mixture. Only few investigations have focused on developing a fundamental understanding how the ordered structure of mesoporous nanoparticles is formed during the synthesis. This is a severe shortcoming, however, as a better understanding of the molecular processes occurring during synthesis will likely provide keys for improved structure control of mesoporous silica nanoparticles.

In order to address this shortcoming this dissertation described the synthesis, characterization and structural evolution during synthesis of a class of non-modified and modified ordered mesoporous silica nanoparticles. Using global as well as local structural characterization techniques at different time points during synthesis, i.e. small angle x-ray scattering (SAXS) and transmission electron microscopy (TEM), significant attention was paid to revealing the formation mechanisms of ordered mesoporous silica nanoparticles. The insights gained from these studies helped in

better understanding and ultimately better controlling the architecture of the final products.

There were also many attempts in the research community in the past to integrate inorganic nanoparticles with additional functionalities into the ordered mesoporous silica matrix. However, in most of these cases the work failed in retaining the regularity of the silica pore structure. Only few studies resulted in ordered mesoporous silica composites. In these studies the location of the inorganic particles in the silica matrix was different than in the case of irregular pore structures. No studies had looked at what happens during particle synthesis and what causes the pore irregularity of nanocomposites. Capturing the formation of magnetic-nanoparticle embedding ordered mesoporous silica nanoparticles at each time point in the synthesis revealed the relation between location of the magnetic nanoparticles and the corresponding mesostructure. As it turned out the formation mechanism of the silica nanocomposites can be understood in the context of crystallization in the presence of impurities. Depending on the rate of silica condensation and restructuring, the final location of the magnetic nanoparticles (the impurity) will influence the pore structure of the resulting materials. The magnetic nanoparticles could thus be employed as a probe to study the structural evolution of the liquid crystal-like silica pore structure.

Many past efforts have aimed at the design of different functionalities, pore structures, and sizes of silica particles. Here again the thesis followed the premise that by understanding particle formation mechanisms and thus the parameters that govern mesostructure, one can better tailor porosity and surface chemistry. To this end the thesis demonstrated the synthesis of two different morphologies of mesoporous silica nanoparticles with two dimensional, straight pore channels and three-dimensional, large cavities connected with small windows, respectively, with different pore sizes and particle sizes. It has been claimed that a clear difference resulting from such

structural differences is the diffusion kinetics of adsorbed substances. Indeed, during the past years, there have been an increasing number of research groups involved in the synthesis of mesoporous materials for bio-related applications, especially for drug-delivery. This area is a very nice example for the potential of translating developments in materials science to biomedical applications. Further developments may offer promising possibilities for ultimately better medical treatments. It thus would be very nice to next conduct experiments on adsorption and release rates of the two mesoporous silica nanoparticles developed in this thesis.

Integrating two different pore architectures into a single silica nanomaterial may be another next step. Such materials could be the inorganic equivalent of multi-compartment micelles that have been developed from ABC triblock terpolymers over the last couple of years.[1] Even though ordered mesoporous silica particles are microscopically amorphous, they can be thought of as crystalline at the mesoscopic length scale. Similar to what has been shown for crystalline inorganic nanoparticles, i.e. the preferred growth along specific crystallographic directions, it should be possible to grow complex structures using the faceted cubic nanoparticles described in this thesis. Except that the current nanoparticles are liquid-crystalline-like materials for which the specific length scale for, e.g. epitaxial growth conditions, are shifted to larger length scales by orders of magnitude. Understanding key parameters governing the pore structure/geometry formation will undoubtedly help control such crystallographically dominated structure evolution in mesoporous materials. If successful this could lead to growth of, e.g. one ordered phase out of a different ordered phase or growing two different ordered phases simultaneously out from the same mesoporous silica base structure. Such studies could open a new avenue of research on structure control of ordered mesoporous silica.

REFERENCE

1. Pochan, D. J.; Chen, Z. Y.; Cui, H. G.; Hales, K.; Qi, K.; Wooley, K. L., *Science* **2004,** *306* (5693), 94-97.

APPENDIX A

Supporting Information for Chapter 3

Experimental Section

Synthesis of Aminated Mesoporous Silica Nanoparticles (NH_2-MSNs)

Ethyl acetate (EtOAc), ammonium hydroxide (NH_4OH), and a mixture of silane precursors (tetraethyl orthosilicate (TEOS) and 3-aminopropyl triethoxysilane (APTES)) were added into an aqueous solution of hexadecyltrimethylammonium bromide (CTAB) (54.8 mM) and stirred for 5 minutes. Additional water was then added into the reaction before leaving the solution overnight under stirring. The pH of the solution at this point was around pH=11. The molar composition of chemicals used was 1 CTAB:3.68 TEOS:4.29 APTES:150.73 NH_3:32.81 EtOAc:28759.12 H_2O. The volume ratio of all compounds in milliliters was 1 CTAB (aq):0.045 TEOS:0.055 APTES:0.54 NH_4OH:0.176 EtOAc:27.38 H_2O. The resulting solution was slightly translucent. After 24 hours, the reaction solution was neutralized using hydrochloric acid solution (2 M). Every step was performed at room temperature. The sample was cleaned by centrifugation and redispersed in ethanol. Two methods were used to remove CTAB: (a) acid extraction using an acetic acid/ethanol mixture (95/5 v/v) by stirring cleaned as-made materials in acid solution for 30 minutes, before centrifugation to remove CTAB and acetic acid, and (b) calcination in air at 540^{o}C for 6 hours. The samples with these different treatments are referred to, in this paper, as acid-extracted and calcined materials, respectively.

Synthesis of Large-pore NH_2-MSNs

In general, the preparation and chemical concentrations used were similar to the synthesis protocol of NH_2-MSNs, except the presence of 1,3,5-trimethylbenzene

(TMB). After the addition of EtOAc and NH_4OH, TMB was added into the CTAB aqueous solution. The solution was stirred for 30 minutes before adding a mixture of silane precursors. The molar composition of chemicals used was 1 CTAB:3.68 TEOS:4.29 APTES:150.73 NH_3:32.81 EtOAc:18.68 TMB:28759.12 H_2O. The volume ratio of all compounds in milliliters was 1 CTAB (aq):0.045 TEOS:0.055 APTES:0.54 NH_4OH:0.176 EtOAc:0.142 TMB:27.38 H_2O. The subsequent steps were identical to what has been described in the previous section.

Synthesis of TRITC-labeled NH_2-MSNs

Tetramethyl rhodamine isothiocyanate (TRITC) (5.6 mM in dimethyl sulfoxide) was conjugated to APTES with 1:25 (TRITC:APTES) molar ratio while stirring in a nitrogen atmosphere glove box overnight before use. Fluorescent mesoporous silica nanoparticles were prepared in a manner identical to the synthesis of NH_2-MSNs, with the exception that conjugated TRITC (90 μL) was added 1 minute before the addition of silane precursors.

Synthesis of TRITC-labeled Large-pore NH_2-MSNs

The preparation and chemical concentrations used were identical to the synthesis protocol of large-pore NH_2-MSNs, except that 1 minute before the addition of silane precursors the conjugated TRITC was added (see previous paragraph).

Surface Modifications of TRITC-labeled NH_2-MSNs and TRITC-labeled Large-pored NH_2-MSNs with Poly(ethylene glycol)

A coating protocol was modified from Kim *et al.*[1] Poly(ethylene glycol)-succinimidyl succinate (5 mg; MW 5000) was dissolved in ethanol (48 mL) at 40 ^oC for 3-5 minutes until a clear solution was formed. Suspension of acid-extracted

TRITC-labeled silica particles (5 mg) in ethanol (2 mL) was added into the PEG solution preheated to 40 ^{o}C. The reaction solution was kept at 40 ^{o}C for 3 hours to allow the reaction between amine groups on the particle surface and succinimidyl ester groups to complete. The resulting product was cleaned by centrifugation and redispersion in ethanol and water to remove excess or unreacted PEG molecules.

Characterization

Transmission electron microscopy (TEM) images were obtained with a FEI Tecnai T12 Spirit microscope operated at an acceleration voltage of 120kV. Average particle sizes were obtained by averaging over approximately 100 particles. Hydrodynamic particle sizes, particle size distributions, and zeta potentials in water were measured on a Malvern Zetasizer Nano-SZ. Hydrodynamic particle sizes and particle size distributions based on the mean number percents were used in this study. Small-angle x-ray scattering (SAXS) patterns of calcined NH_2-MSNs and acid-extracted large-pore NH_2-MSNs were obtained on a home-built beamline as previously described[2] with a sample-to-detector distance of 25 cm, whereas SAXS patterns of acid-extracted NH_2-MSNs, acid-extracted TRITC-incorporated NH_2-MSNs, and acid-extracted TRITC-labeled large-pore NH_2-MSNs were obtained at the G1 beamline in the Cornell High Energy Synchrotron Source (CHESS) with a beam energy of 9.5 keV and a sample to detector distance of 35 cm.[3] All samples were in dry forms. Nitrogen physisorption isotherms of dried samples were obtained with a Micromeritics ASAP2020 physisorption instrument. The particles exhibited nitrogen sorption isotherms of type IV according to BDDT classification. Surface areas were determined according to the Brunauer-Emmett-Teller (BET) method.[4] The BET surface area analysis was performed in the range between 0.042 and 0.095. Calculation of the pore size distributions from the adsorption branches of the

isotherms was performed according to the Barrett-Joyner-Halenda[5] (BJH) method. We note that this method is known to underestimate the pore size distribution for materials with spherical pores below 10 nm in diameter.[6] Thus we applied the geometrical model of a $Pm\bar{3}n$ cage-like mesoporous material and estimated the pore size from the mesopore volume and the lattice constants obtained by SAXS (see Table A4). Fourier Transform Infrared (FTIR) spectra were measured with Bruker Optics-Vertex 80V equipped with a transmission holder under vacuum. FTIR spectra were collected in the frequency range of 4000-400 cm^{-1} for 128 scan, 4 cm^{-1}. Analyses were performed on KBr (blank) pellet and sample pellets containing 1wt% samples in KBr. All elemental analyses were conducted by Galbraith Laboratories, Inc., Knoxville, TN. Thermogravimetric analysis (TGA) was conducted on a TA instruments Q500 thermogravimetric analyzer. All measurements were taken from room temperature to 650 ^{o}C under a nitrogen flow.

For cell uptake experiments, each PEGylated and TRITC-labeled mesoporous silica sample was studied on different cell types, i.e. PEGylated and TRITC-labeled NH_2-MSNs were incubated with COS-7 cells (simian kidney cells) and PEGylated and TRITC-labeled large-pore NH_2-MSNs were incubated with epithelial cells (SLC-44, fetal rat intestinal epithelial cells). COS-7 cells (or epithelial cells) were plated on MatTek coverslip dishes in complete medium overnight in the presence of suspended MSN samples. Prior to imaging, cells were washed 3 times with buffered salt solution (BSS: 135 mM NaCl, 5 mM KCl, 1.8 mM $CaCl_2$, 1 mM $MgCl_2$, 1 mg/ml glucose, 20 mM Hepes, pH=7.2-7.4, 1 mg/ml BSA) to remove free-floating and loosely absorbed particles, and incubated for 5 min with a far-red plasma membrane dye (Cell Mask Deep Red, Molecular Probes, Em/Ex 660/677nm). The uptake and distribution of the particles was then investigated using confocal microscopy (Zeiss 510 Meta LSM). Cells in dishes were mounted on a 40x oil immersion objective for detection of TRITC

labeled particles. Images were processed using Zeiss LSM software.

Structure Analysis

The symmetry assignment for NH_2-MSN materials based on the analysis of 1-dimensional (1-D) SAXS scaterring patterns shown in Figure 3.2 in the main text is described below. From the TEM images which show four-fold as well as three-fold symmetry projections (Figure 3.1b and c, respectively), we started the analysis with the assumption that NH_2-MSNs possess a cubic lattice. To extract peak positions, integrated 1-D SAXS patterns, shown in Figure 3.2 in the main text, were first treated with background subtraction by fitting a power-law curve.

The peak positions were then determined by finding the local minima of the second-order difference of the intensity, $I(q)$. In this way, it was revealed that there is also a small (110) peak in the scattering data. Figure A3 shows the correlation between $s = (h^2+k^2+l^2)^{1/2}$, where h, k and l are the three cubic indices assignments, and the observed peak positions for the acid-extracted NH_2-MSN sample. The observed peak positions correlate linearly with the lattice indices assignments if we assign the first peak to be from (110) reflection. Note that the existence of the 9th peak (q = 0.2445 Å^{-1}) does not allow the first peak to be (200) since this will assign the above peak at $h^2+k^2+l^2 = 28$, for which no such combination of lattice indices h, k and l exists. Similarly, the possibility that the first peak is (211) is excluded because of the existence of the 3rd peak (q = 0.1462 Å^{-1}).

Based on these reflection plane assignments, we proceeded with determining the cubic symmetry aspects. Table A2 shows the list of observed reflections and the comparison with cubic symmetry aspects that show allowed reflections at $h^2+k^2+l^2$ = 4, 5, and 6. The observed reflections match that of symmetry aspect 5 up to (400) reflection planes, and thus we can conclude that the material possesses a cubic

symmetry aspect 5. Structure factor analysis for determining the exact nature of structure such as porosity and pore interconnectivity were not performed due to large background scattering signal.

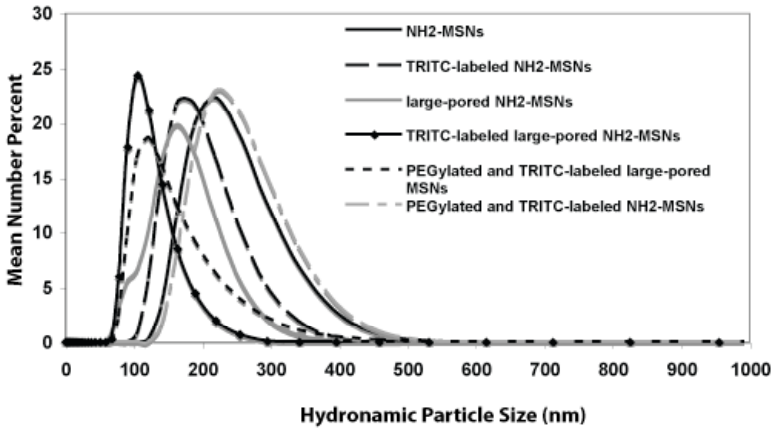

Figure A.1. Hydrodynamic particle sizes of acid-extracted MSNs in Water.

Table A.1. Table of particle sizes and size distributions measured by DLS and TEM as well as zeta potentials of acid-extracted MSNs.

Samples	Particle Size (nm)		Zeta Potential (mV)
	DLS*	TEM	
NH_2-MSNs	220.2	223.1 ± 49.3	42.1 ± 4.96
TRITC-labeled NH_2-MSNs	190.1	214 ± 43.7	36.5 ± 5.97
PEGylated TRITC-labeled NH_2-MSNs	220.2	n/a	-0.55 ± 5.17
Large-pored NH_2-MSNs	164.2	108.2 ± 24.1	43 ± 6.38
TRITC-labeled large-pored NH_2-MSNs	105.7	94.8 ± 15.7	32 ± 5.97
PEGylated TRITC-labeled large-pored NH_2-MSNs	122.4	n/a	6.48 ± 3.93

* DLS: Hydrodynamic particle sizes measured by dynamic light scattering (DLS) technique using Malvern Zetasizer Nano-SZ.

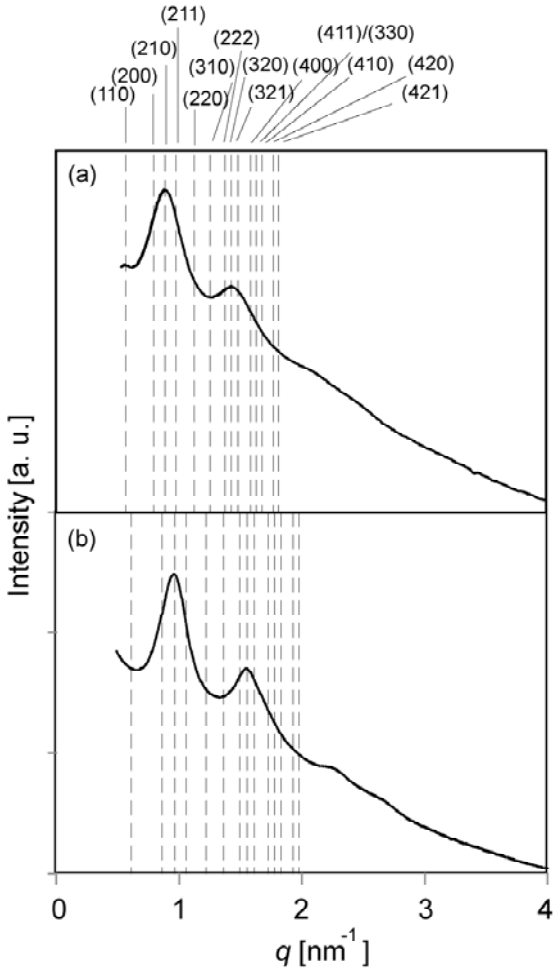

Figure A.2. SAXS patterns of (a) acid-extracted large-pored NH_2-MSNs and (b) acid-extracted TRITC-labeled large-pored NH_2-MSNs.

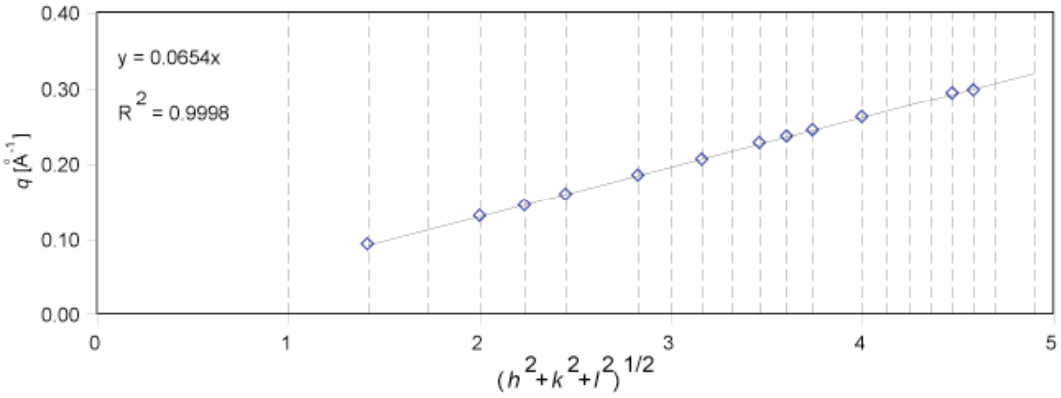

Figure A.3. Correlation between the cubic indices assignments and the observed peak positions of NH_2-MSNs. Dotted lines indicate possible (*hkl*) combinations for cubic lattices. The linear fitting (equation shown above left) is obtained through least squares method.

Table A.2. Table of comparison between the observed reflections of NH_2-MSNs and the allowed reflections for cubic symmetry aspects that include $h^2+k^2+l^2 = 4$, 5, and 6. Peaks in parentheses are weak peaks that are only extracted after subtracting the background and taking the 2nd order difference of the integrated 1D SAXS patterns. The list of allowed reflections for different cubic symmetry aspects are taken from the literature.[7]

$h^2+k^2+l^2$	**1**	**2**	**3**	**4**	**5**	**6**	**8**	**9**	**10**	**11**	**12**	**13**	**14**	**16**	**17**	**18**	**19**	**20**	**21**	**22**	**24**	**25**
Obs.		(+)		+	+	+	(+)		+		+	+	+	+				+	+			
aspects																						
1	+	+	+	+	+	+	+	+	+	+	+	+	+	+	+	+	+	+	+	+	+	+
2	-	+	+	+	+	+	+	+	+	+	+	+	+	+	+	+	+	+	+	+	+	+
5 ($P\bar{4}3n$, $Pm\bar{3}n$)	-	+	-	+	+	+	+	-	+	-	+	+	+	+	+	+	-	+	+	+	+	+
7	-	-	+	+	x	+	+	+	-	+	+	x	+	+	+	+	-	+	+	+	+	x

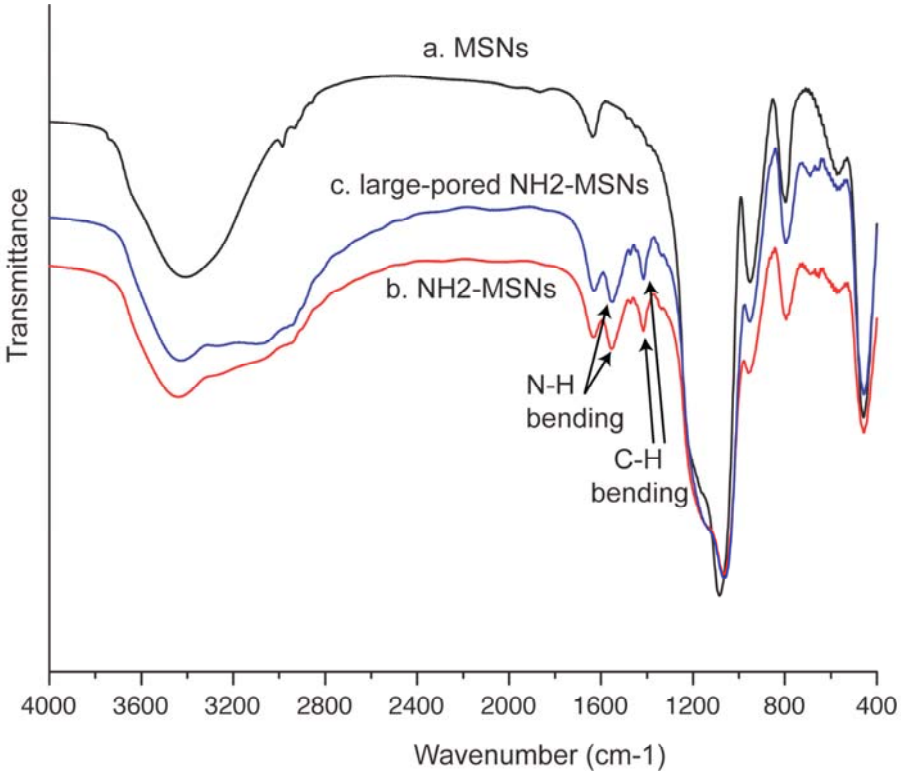

Figure A.4. FTIR spectra of (a) acid-extracted MSNs (no APTES), (b) acid-extracted NH_2-MSNs and (c) acid-extracted large-pored NH_2-MSNs.

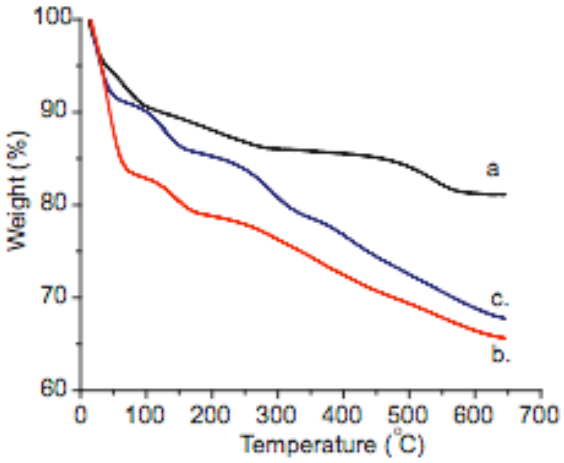

Figure A.5. TGA of (a) acid-extracted MSNs (no APTES), (b) acid-extracted NH_2-MSNs and (c) acid-extracted large-pored NH_2-MSNs.

Table A.3. Table of C, H, N and Si contents of acid-extracted NH_2-MSNs and acid-extracted large-pored NH_2-MSNs from elemental analysis.

Samples	Weight %[a]				Mol %[b]
	C	H	N	Si	
NH_2-MSNs	13.36	4.275	3.108	30.4	19.27
large-pored NH_2-MSNs	12.79	3.599	3.598	30.7	22.43

[a] mass of analyzed NH_2-MSNs for elemental analysis of CHN and Si were 2.094 mg and 31.32 mg, respectively. Mass of analyzed large-pored NH_2-MSNs for elemental analysis of CHN and Si were 2.313 mg and 40.51 mg, respectively. [b] mol% of N in analyzed samples compared with the initial loading concentrations of total silane.

Calculation method

Assume all TEOS completely underwent reactions, N_{APTES} and N_{TEOS} are the number of moles of APTES and TEOS fed into the synthesis, respectively. M_{APTES} is the number of moles of APTES that were in the final product.

For NH_2-MSNs,

starting: $$N_{APTES}/\left(N_{TEOS}+N_{APTES}\right)=27/50 \qquad (1)$$

final: $$M_{APTES}/\left(N_{TEOS}+M_{APTES}\right)=6.232/30.4 \qquad (2)$$

(1); $$(50/27)N_{APTES}=N_{TEOS}+N_{APTES} \qquad (3)$$

(2); $$(30.4/6.232)M_{APTES}=N_{TEOS}+M_{APTES} \qquad (4)$$

(3)-(4); $$0.85N_{APTES}=3.88M_{APTES}$$

$$M_{APTES}=0.219N_{APTES}=11.83$$

mol% of APTES w.r.t. total silane in final product = $(11.83/46+11.83)\,x\,100=20.45$ mol%

Table A.4. Estimated spherical cavity size (D_{me}) and average wall thickness (h) for each NH_2-MSN sample. The cubic lattice constant, a, is determined from SAXS, and the mesoporosity, ε_{me}, is estimated from the nitrogen sorption profile as described below.

	NH_2-MSN (acid-extracted)	NH_2-MSN (calcined)	Large-pored NH_2-MSN (acid-extracted)	Large-pored NH_2-MSN (calcined)
a [nm]	9.61	8.96	15.90	13.90
ε_{me}	0.2457	0.2259	0.4854	0.4394
D_{me} [nm]	3.73	3.39	7.76	6.56
h [nm]	3.82	3.87	2.74	2.79
BJH model [nm]	2.7	2.7	5.3	5.0

Calculation method

Here we only show the calculations on the cavity size and wall thickness for the acid-extracted NH_2-MSNs (without TMB). The geometrical model is described in Ravikovitch and Neimark[6], and we follow their calculations in Section 5.

The lattice constant for the acid-extractred NH_2-MSNs is measured to be a = 9.6nm from SAXS. For nitrogen sorption profiles, since the lower plateau of the nitrogen sorption is not well-defined, we took the volume of condensed nitrogen adsorbed at p/p_0 = 0.2 as the micropore volume V_{micro} (8.586 mmol/g). The upper plateau of the nitrogen sorption was defined at the volume of condensed nitrogen adsorbed at p/p_0 = 0.9 to give the total pore volume, V_{total} (15.649 mmol/g).

The mesoporosity of the material, ε_{me}, can then be calculated from:

$$\varepsilon_{me} = \rho_v(V_{total} - V_{micro})/1 + \rho_v V_{total} = 0.2457$$

where ρ_V is the bulk density of the solid, which was assumed to be 2.2 g/cm^3 for the silica walls. Assuming $Pm\bar{3}n$ symmetry and a cage-like spherical pore structure with the number of cavities per unit cell = 8, the sphere diameter D_{me} can be calculated as:

$$D_{me} = a(6\varepsilon_{me}/\pi v)^{1/3} = 3.73 \text{ nm}.$$

The average wall thickness for this material, h, can be calculated as:

$$h = D_{me}(1 - \varepsilon_{me})/3\varepsilon_{me} = 3.82\ nm$$

Table A4 lists estimates for spherical cavity size, D_{me}, and average wall thickness, h, of the NH_2-MSN samples (as well as large pored NH_2-MSN samples) derived from these calculations. Mean pore size estimates from the BJH model are also listed. Comparison of the results suggests that the BJH model may underestimate the pore size of the normal and large-pore NH_2-MSN samples by about 1 and 1-2 nm, respectively.

REFERENCES

1. Kim, J.; Kim, H. S.; Lee, N.; Kim, T.; Kim, H.; Yu, T.; Song, I. C.; Moon, W. K.; Hyeon, T., *Angewandte Chemie, International Edition* **2008,** *47* (44), 8438-8441.

2. Toombes, G. E. S.; Mahajan, S.; Weyland, M.; Jain, A.; Du, P.; Kamperman, M.; Gruner, S. M.; Muller, D. A.; Wiesner, U., *Macromolecules* **2008,** *41* (3), 852-859.

3. Tate, M. W.; Eikenberry, E. F.; Barna, S. L.; Wall, M. E.; Lowrance, J. L.; Gruner, S. M., *Journal of Applied Crystallography* **1995,** *28*, 196-205.

4. Brunauer, S.; Deming, L. S.; Deming, W. E.; Teller, E., *Journal of the American Chemical Society* **1940,** *62*, 1723-1732.

5. Barrett, E. P.; Joyner, L. G.; Halenda, P. P., *Journal of the American Chemical Society* **1951,** *73* (1), 373-380.

6. Ravikovitch, P. I.; Neimark, A. V., *Langmuir* **2002,** *18* (5), 1550-1560.

7. Kasper, J. S.; Lonsdale, K. in: *International Tables for X-Ray Crystallography*, Kynoch Press: Birmingham, Eng., **1967,** vol. 2, 147.

APPENDIX B

Supporting Information for Chapter 4

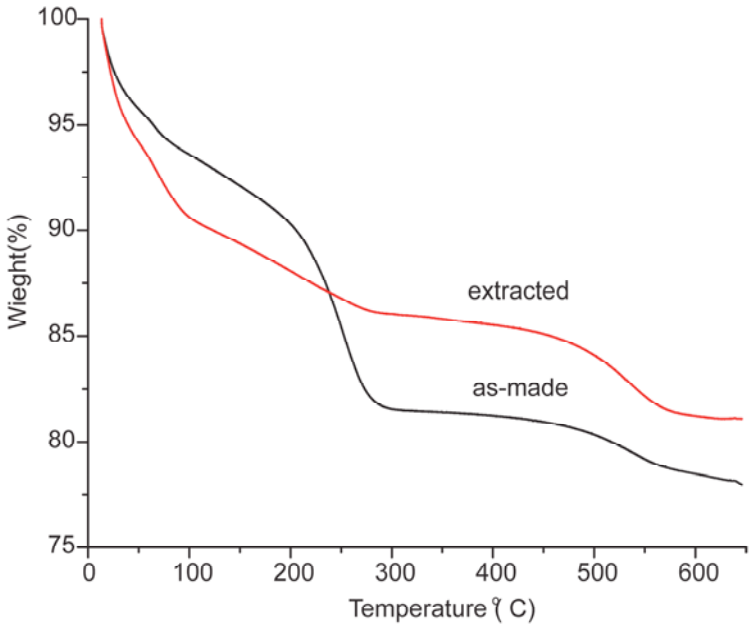

Figure B.1. Thermogravimetric weight loss curves of control MSNs before (red) and after (black) removal of surfactants.

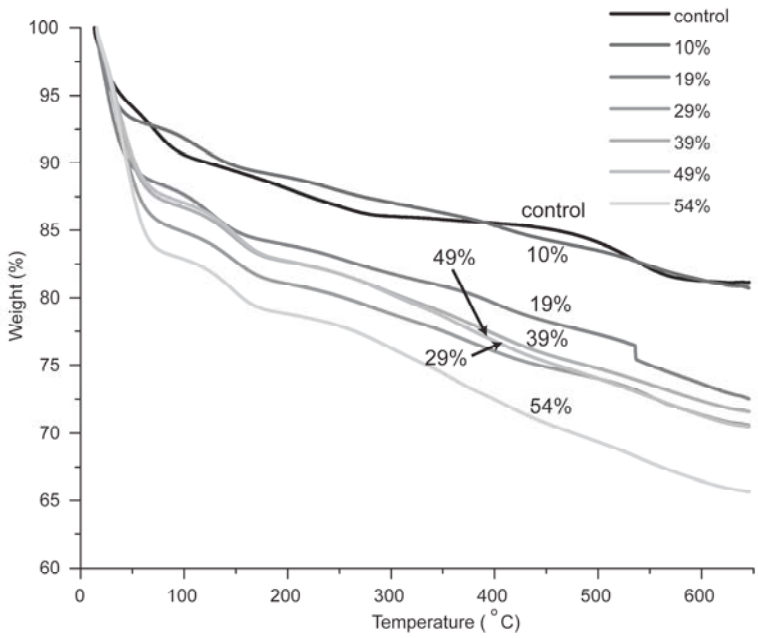

Figure B.2. Thermogravimetric weight loss curves of control sample and X-NH_2-MSNs after surfactant removal, where X=10, 19, 29, 39, 49 and 54 mol% APTES in the reaction feed.

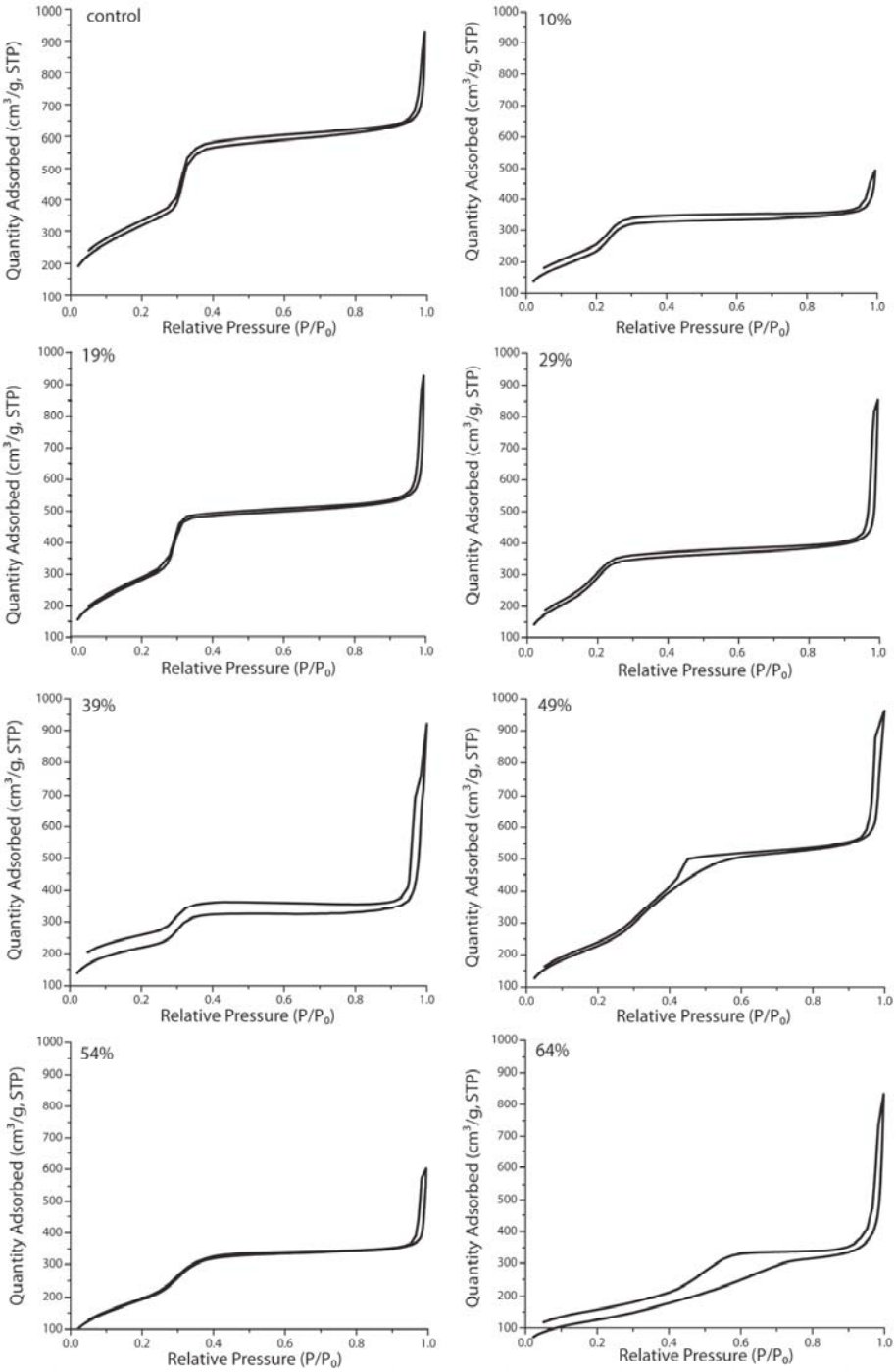

Figure B.3. N_2 adsorption and desorption isotherms of control sample and X-NH_2-MSNs after surfactant removal, where X=10, 19, 29, 39, 49, 54 and 64 mol% APTES in the reaction feed.

APPENDIX C

Supporting Information for Chapter 5

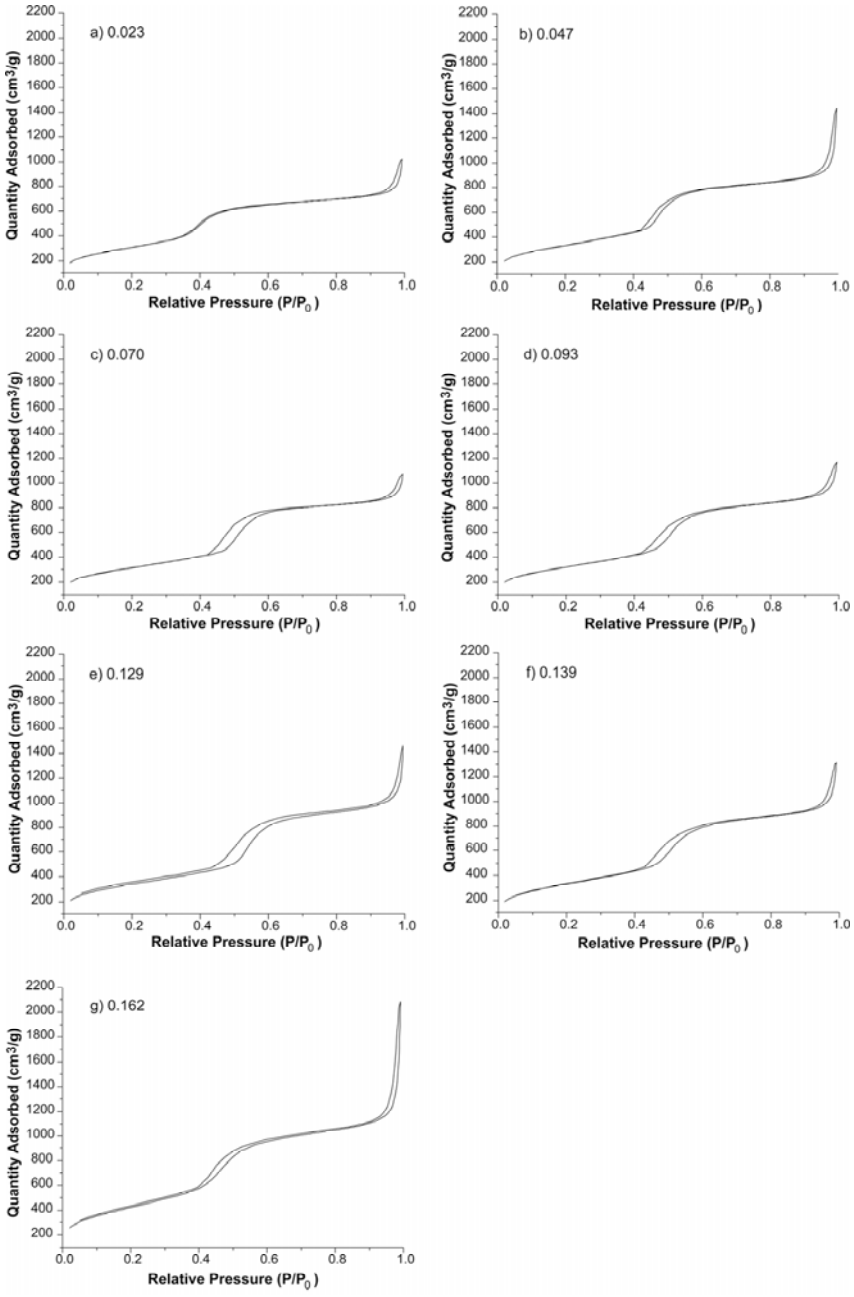

Figure C.1. N_2 adsorption and desorption isotherms of acid-extracted large pore MSNs made from different TMB concentrations (a-g).

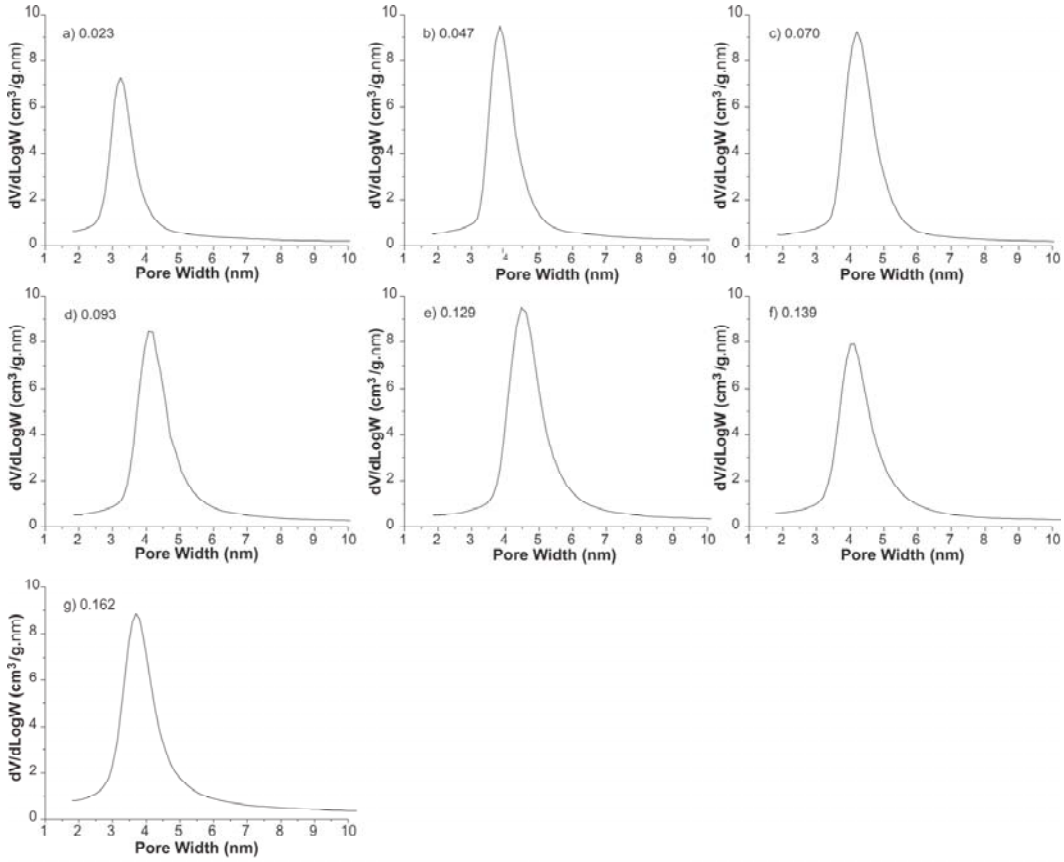

Figure C.2. BJH pore size of acid-extracted large pore MSNs made from different TMB concentrations (a-g).

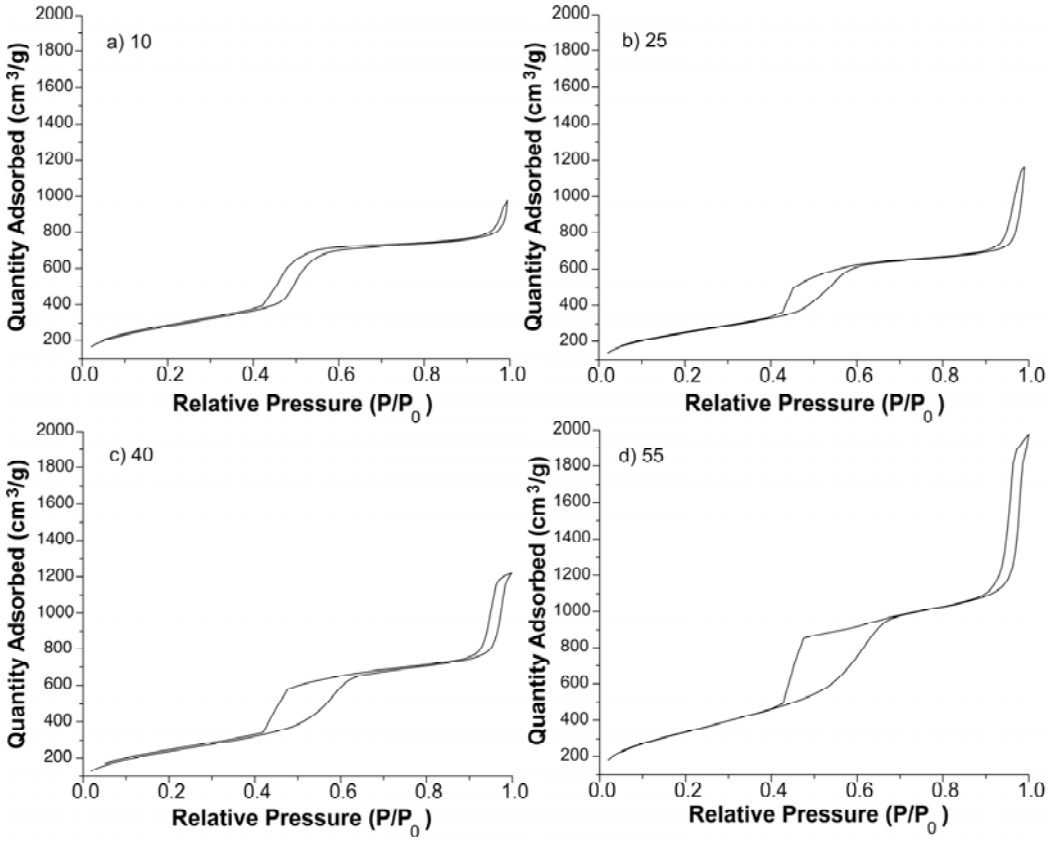

Figure C.3. N_2 adsorption and desorption isotherms of acid-extracted large pore NH_2-MSNs made from 0.047 M TMB with different mol% APTES in the reaction feed.

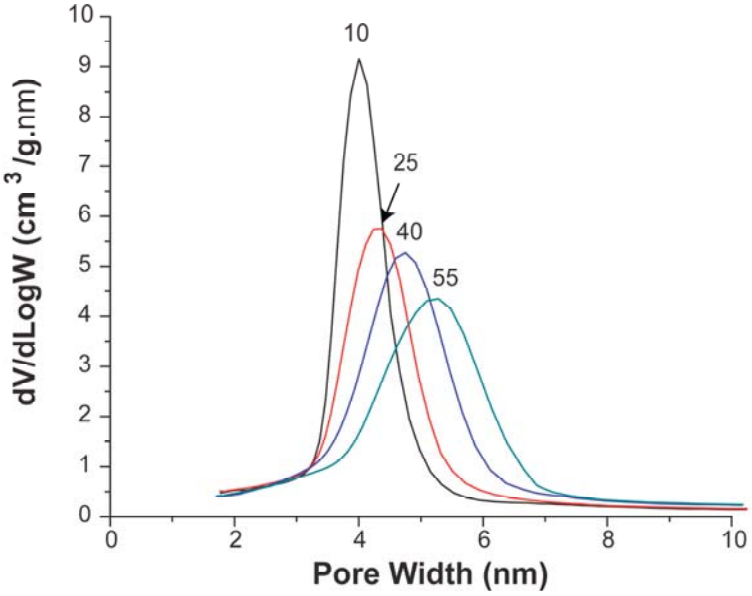

Figure C.4. BJH pore sizes of acid-extracted large pore NH_2-MSNs made from 0.047 M TMB with different mol% APTES in the reaction feed.

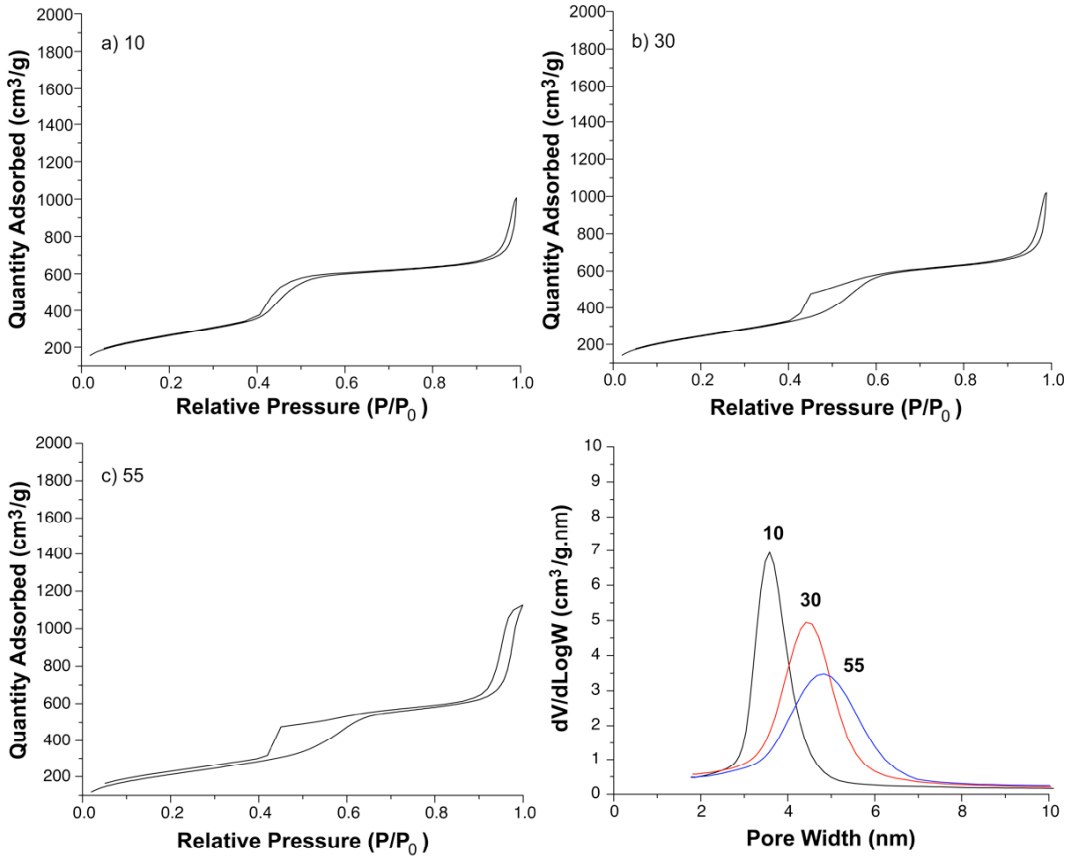

Figure C.5. N_2 sorption isotherms and BJH pore size of acid-extracted large pore NH_2-MSNs made from 0.093 M TMB with different mol% APTES in the reaction feed.

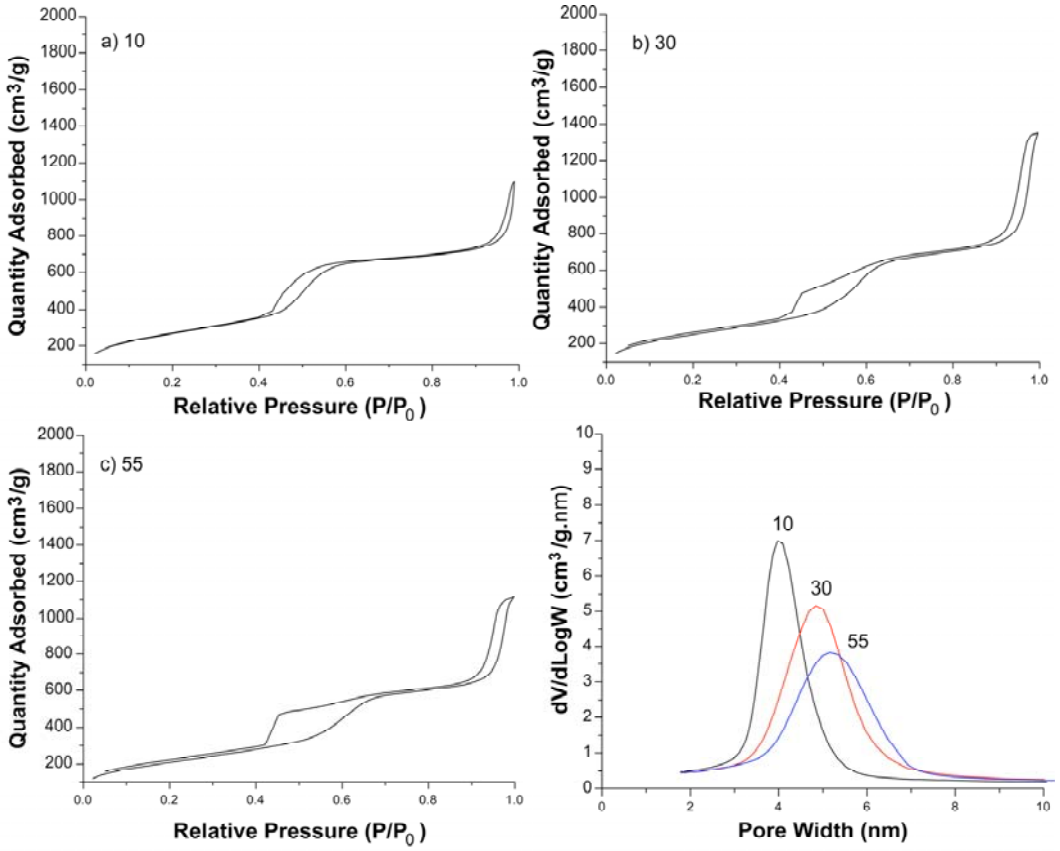

Figure C.6. N_2 sorption isotherms and BJH pore size of acid-extracted large pore NH_2-MSNs made from 0.129 M TMB with different mol% APTES in the reaction feed.